Report Title:

CATHODES FOR LOW TEMPERATURE SOFC: ISSUES CONCERNING INTERFERENCE FROM INERT GAS ADSORPTION AND CHARGE TRANSFER

Type of Report: Final Technical Report

Reporting Period Start Date: October 1, 2002
Reporting Period End Date: December 31, 2003
Principal Author: Professor Anil V. Virkar
Date Report Was Issued: May 5, 2004
DOE Award Number: DE-FC26-02NT41565

Name and Address of Submitting Organization:

Department of Materials Science & Engineering
122 S. Central Campus Drive
University of Utah
Salt Lake City, UT 84112

DISCLAIMER:

This report was prepared as an account of work sponsored by an agency of the United States Government. Neither the United States Government nor any agency thereof, nor any of their employees, makes any warranty, express or implied, or assumes any legal liability or responsibility for the accuracy, completeness, or usefulness of any information, apparatus, product or process disclosed, or represents that its use would not infringe privately owned rights. Reference herein to any specific commercial product, process, or service by trade name, trademark, manufacturer, or otherwise does not necessarily constitute or imply its endorsement, recommendation, or favoring by the United States Government or any agency thereof. The views and opinions of authors expressed herein do not necessarily state or reflect those of the United States Government or any agency thereof.

ABSTRACT

This report summarizes the work done on the project over the duration of the project, from October 1, 2002 through December 31, 2003, which includes a three month no-cost extension. Effort was directed in the following areas:

(1) Fabrication of Sr-doped $LaCoO_3$ (LSC) dense and porous samples.
(2) Design and construction of a conductivity relaxation apparatus for the estimation of surface exchange coefficient, k_{chem}, which depends on adsorption, and oxygen chemical diffusion coefficient, $\widetilde{D}_O$, the parameters which are thought to describe the cathodic activation polarization (overall charge transfer) in mixed ionic electronic conducting (MIEC) cathodes.
(3) The measurement of k_{chem} and $\widetilde{D}_O$ on LSC by conductivity relaxation, as a function of temperature and oxygen partial pressure, p_{O_2}.
(4) Fabrication of YSZ electrolyte discs with patterned LSM and LSC electrodes with three-phase boundary (TPB) length, l_{TPB}, varying between 50 and 1200 cm^{-1}.
(5) The measurement of charge transfer resistance, R_{ct}, and estimation of the charge transfer resistivity, ρ_{ct}, as a function of temperature and p_{O_2}, and the incorporation of the adsorption step in the analysis.
(6) Preliminary cell tests with oxidants having different inert gas diluents; N_2, Ar, and CO_2.

Dense samples of LSC of thickness as small as 150 microns were fabricated by sintering followed by grinding. Porous samples of LSC were also fabricated wherein the porosity was ~30%. Both samples were used in conductivity relaxation experiments. Analysis of data from the dense samples gives both k_{chem} and $\widetilde{D}_O$, while that of porous samples gives k_{chem}. It was observed that at a given temperature, k_{chem} increases with increasing p_{O_2}, while the $\widetilde{D}_O$ is essentially a constant. The dependence of k_{chem} on p_{O_2} is attributed to the adsorption step. It was also observed that the porous samples gave a more accurate measurement of k_{chem}, as the data were not influenced by $\widetilde{D}_O$. By contrast, the results on dense samples were influenced by $\widetilde{D}_O$, especially at lower temperatures. It is thus concluded that the use of porous samples is preferred for the measurement of k_{chem}.

In the case of composite electrodes, such as LSM + YSZ, the relevant parameters are the ρ_{ct} (or R_{ct}) and the ionic resistivity of YSZ ρ_i, where $1/\rho_{ct}$ is analogous to k_{chem} and $1/\rho_i$ is analogous to $\widetilde{D}_O$. LSM patterned electrodes were deposited on YSZ discs using photomicrolithography. The R_{ct} was measured as a function of temperature and p_{O_2} using complex impedance techniques, on samples with l_{TPB} varying between 50 and 1200 cm^{-1}. The plot of $1/R_{ct}$ vs. l_{TPB} was linear, consistent with the occurrence of charge transfer at TPB. Also, the data plotted on the assumption of dissociative adsorption was consistent with the model. The significance of the role of adsorption is discussed. Similar results were

observed with LSC, indicating a similar role of adsorption. In the case of LSC, however, a significant transport of oxygen also occurs through the dense part of the electrode.

Preliminary work was conducted on the testing of button cells with mixtures of $O_2 + N_2$, O_2 + Ar, and $O_2 + CO_2$ as oxidants, wherein the p_{O_2} was varied between ~0.05 and ~1.0 atm. As expected, the results showed that the higher the p_{O_2}, the better was the performance. In pure oxygen, the maximum power density at 800°C was ~2.9 W/cm^2. However, in 5% O_2, it was ~0.6 W/cm^2. This difference is attributed to adsorption, indicating that both charge transfer and adsorption needs to be addressed in order to improve cathode performance at lower temperatures and under high oxidant utilization (in low p_{O_2} atmospheres). Data at low current densities was analyzed to deduce the polarization resistance, R_p, and its dependence on p_{O_2}. Although preliminary, the results show differences in R_p, which are attributed to possible differences in adsorption characteristics. Specifically, it was observed that the polarization resistance was lower in $O_2 + CO_2$ atmospheres compared to $O_2 + N_2$ and O_2 + Ar atmospheres. This suggests that CO_2 has a lower tendency for adsorption compared to the other two diluents.

TABLE OF CONTENTS

	Page
LIST OF GRAPHICAL MATERIALS	6
INTRODUCTION	7
EXECUTIVE SUMMARY	9
EXPERIMENTAL	11
a) LSC Sample Fabrication and the Measurement of k_{chem} and $\widetilde{D}_O$ by Conductivity Relaxation	11
b) Measurement of R_{ct} using Patterned Electrodes	13
c) Fabrication and Electrochemical Testing of Button Cells in Various O_2 + Diluent Gas Mixtures	14
RESULTS AND DISCUSSION	15
a) LSC Sample Fabrication and the Measurement of k_{chem} and $\widetilde{D}_O$ by Conductivity Relaxation	15
b) Measurement of R_{ct} using Patterned Electrodes	17
d) Electrochemical Testing of Button Cells in Various O_2 + Diluent Gas Mixtures	18
CONCLUSIONS	20
REFERENCES	35
LIST OF ACRONYMS AND ABBREVIATIONS	36
APPENDIX-I: Estimation of Charge Transfer Resistivity of $La_{0.8}Sr_{0.2}MnO_3$ (LSM) Cathode on $Y_{0.16}Zr_{0.84}O_2$ (YSZ) Electrolyte using Patterned Electrodes; Manuscript submitted to *J. Electrochem. Soc*., (2004).	37
APPENDIX-II: Measurement of Surface Exchange Coefficient on Porous $La_{0.6}Sr_{0.4}CoO_{3-\delta}$ Samples by Conductivity Relaxation; Manuscript submitted to *J. Electrochem. Soc*. (2004).	81

LIST OF GRAPHICAL MATERIALS

Figure		Page
Figure 1:	A photograph of LSC sample of 218 μm used for conductivity relaxation	22
Figure 2:	A photograph of the new (smaller) sample chamber	23
Figure 3:	A photograph of the 218 μm sample in the smaller chamber	24
Figure 4:	An SEM micrograph of a porous LSC sample	25
Figure 5:	Plots of $g(t)/\sqrt{t}$ vs. $\sqrt{t}$ for dense LSC samples of two thicknesses	26
Figure 6:	A plot of $g(t)$ vs. t for a porous LSC sample	27
Figure 7:	Plots of $g(t)/\sqrt{t}$ vs. $\sqrt{t}$ for a dense sample for various p_{O_2} changes	28
Figure 8:	k_{chem} vs. p_{O_2} using a dense LSC sample	29
Figure 9:	k_{chem} vs. p_{O_2} using a porous LSC sample	30
Figure 10:	An SEM micrograph of an LSM patterned electrode: l_{TPB} = 500 cm^{-1}	31
Figure 11:	A profilometric trace of the LSM patterned electrode	32
Figure 12:	Impedance spectra for patterned electrodes of different l_{TPB}	33
Figure 13:	Plots of $1/R_{ct}$ vs. l_{TPB} in air at different temperatures	34
Figure 14:	Impedance spectra in air at several temperatures (l_{TPB} = 1200 cm^{-1})	35
Figure 15:	Arrhenius plots of R_{ct} in atmospheres with different p_{O_2}	36
Figure 16:	Impedance spectra on patterned electrodes of different l_{TPB} in atmospheres with different p_{O_2}	37
Figure 17:	Plots of $R_{ct}p_{O_2}$ vs. p_{O_2} for LSM patterned electrode at various temperatures	38
Figure 18:	Plots of $R_{ct}p_{O_2}$ vs. p_{O_2} for LSC patterned electrode at various temperatures	39
Figure 19:	An SEM micrograph of a typical anode-supported cell made and tested	40
Figure 20:	Voltage and power density vs. current density for a cell tested at 800^{o}C in O_2 + N_2 gas mixtures as oxidant with various p_{O_2}	41
Figure 21:	Voltage and power density vs. current density for a cell tested at 800^{o}C in O_2 + Ar gas mixtures as oxidant with various p_{O_2}	42
Figure 22:	Voltage and power density vs. current density for a cell tested at 800^{o}C in O_2 + CO_2 gas mixtures as oxidant with various p_{O_2}	43
Figure 23:	Plots of total resistance, R_t (as $i \to 0$) vs. $1/\sqrt{p_{O_2}}$	44
Figure 24:	Schematic of the dependence of θ_{O_2} on p_{O_2}	45
Figure 25:	Experimentally measured $1/\rho_{ct}$ vs. p_{O_2}	46

INTRODUCTION

In the majority of SOFC-based systems, the oxidant is expected to be air, and not pure oxygen due to cost considerations. Thus, the maximum p_{O_2} in the incoming, fresh oxidant is ~0.21 atm, assuming the total oxidant pressure to be 1 atm. During the operation of SOFC, the actual p_{O_2} very close to the cathode interlayer/electrolyte interface is lower than 0.21 atm, and the higher the current density, the lower is the interface p_{O_2}. The overall cathodic electrochemical reaction of charge transfer involves an adsorption step (either associative or dissociative). The fractional surface coverage, θ_{O_2} (θ_O in the case of dissociative adsorption), depends upon local p_{O_2} - usually through some adsorption isotherm, the simplest being Langmuir. It is expected that the reaction of charge transfer in general will be facilitated by higher θ_{O_2} (or θ_O). Thus, the lower the p_{O_2} in the cathode interlayer, the higher is the activation polarization, and the lower is the performance. The situation can become even worse downstream in a SOFC stack, since the oxidant (just outside the cathode) itself is depleted, which means even lower p_{O_2} at the cathode interlayer/electrolyte interface. It is imperative that the effect of local p_{O_2} (and the effect it has on adsorption, θ_{O_2} or θ_O) on cathodic reaction needs to be better understood in order to design cathodes, which can exhibit good performance in oxygen-depleted oxidants. Since the diluent in the oxidant is N_2, its possible adsorption may also play an important role. The development of cathode materials exhibiting good performance in oxygen-depleted oxidants is important because this would allow the attainment of high oxidant utilization – which is important to minimize the amount of oxidant circulated through the stack, and thus minimize thermal losses.

Since oxygen gas must adsorb (either associative or dissociative) for the reaction of cathodic charge transfer to occur, it is imperative that θ_{O_2} (or θ_O) be as large as possible for a given p_{O_2}. Assuming Langmuir associative adsorption, θ_{O_2} is given by [1,2]

$$\theta_{O_2} = \frac{b' p_{O_2}}{1 + b' p_{O_2} + \sum_{i \neq O_2} b_i p_i} \tag{1}$$

where b' is the adsorption coefficient of O_2, and b_i and p_i are, respectively, adsorption coefficient and partial pressure of gaseous species i. Equation (1) shows that the θ_{O_2} not only depends on adsorption coefficient and partial pressure of O_2, but also on other species present. With air as the oxidant, the above may be given as

$$\theta_{O_2} = \frac{b' p_{O_2}}{1 + b' p_{O_2} + b'' p_{N_2}} = \frac{b' p_{O_2}}{1 + b'' + \left(b' - b''\right) p_{O_2}} \tag{2}$$

assuming the total pressure is one atm. The above implies that regardless of the actual magnitude of b'', which is the adsorption coefficient of N_2, as long as it is not identically zero, the presence of N_2 should interfere with the occurrence of the cathodic reaction. In this

context, the desired cathode material is that which has $b' >> b''$, or more specifically, we need to have $b' p_{O_2} >> b'' p_{N_2}$ over the range of partial pressures of interest. Of direct relevance, however, is not only the dependence of θ_{O_2} (or θ_O) on p_{O_2}, but also the effect of p_{O_2} on cathodic charge transfer resistance. The above equations are written for associative adsorption. If the adsorption is dissociative, then with the only gases present being O_2 and N_2, the adsorption isotherm may be given by

$$\theta_O = \frac{b^* \sqrt{p_{O_2}}}{1 + b^* \sqrt{p_{O_2}} + b^{**} \sqrt{p_{N_2}}} \tag{3}$$

where it is assumed that both O_2 and N_2 adsorb dissociatively, and b^* and b^{**} are the corresponding adsorption coefficients. Experimental work was conducted to determine the dependence of cathodic charge transfer resistance on p_{O_2} using patterned electrodes deposited by photomicrolithographic techniques. Details of this work are given in Appendix I, which is a copy of manuscript recently submitted for publication to the *Journal of the Electrochemical Society*.

It is known that cathodic polarization is lower if the cathode exhibits MIEC characteristics [3-7]. A prospective MIEC cathode can be a composite of two materials, such LSM and YSZ, wherein MIEC characteristics exist at the microstructural level, or single-phase materials such as LSC, LSF, or LSCF, where the MIEC characteristics exist at the unit cell level [8,9]. In single-phase MIEC cathodes, the relevant parameters, which describe cathodic reaction, are the oxygen surface exchange coefficient, k_{chem} [10-13], and the chemical diffusion coefficient of oxygen, $\widetilde{D}_O$. In order to categorize the efficiency of a cathode material, it is necessary that k_{chem} and $\widetilde{D}_O$ be measured as a function of temperature and atmosphere (p_{O_2}). Towards this end, a conductivity relaxation technique was used and a new method for data analysis was developed, which leads to a more accurate determination of k_{chem} and $\widetilde{D}_O$. In addition, the technique of using porous samples to accurately determine k_{chem} was developed. Details of the latter technique are given in Appendix II, which is a copy of a manuscript recently submitted for publication to the *Journal of the Electrochemical Society*.

Out of cell measurements are useful, but only to a point, especially in a complex electrochemical system such as the SOFC. Thus, mere characterization of cathode materials in out of cell tests, such as the measurement of cathodic polarization resistance using impedance spectroscopy on thick electrolyte discs, is insufficient – and sometimes actually simply inaccurate. That is, there is no substitute to making and testing cells, and correlate the in-cell behavior with out of cell characterization. For this reason, fabrication and testing of anode-supported button cells has been initiated. Results of cell tests in different oxidants, comprising mixtures of O_2 and a diluent are described.

EXECUTIVE SUMMARY

During the performance period of this project, experiments have been conducted on the investigation of the effect of atmosphere and temperature on the cathodic charge transfer reaction with LSC and LSM as electrode materials. This included an investigation of the effect of atmosphere and temperature on surface exchange coefficient, k_{chem}, and chemical diffusion coefficient of oxygen, $\widetilde{D}_O$, in LSC, an investigation of the effect of atmosphere and temperature on charge transfer resistance by impedance spectroscopy using patterned electrodes of LSM and LSC[1] on YSZ deposited by photomicrolithography, and fabrication and electrochemical testing of anode-supported cells with cathode gas containing O_2 diluted with different diluents, such as N_2, Ar, and CO_2.

An apparatus for the measurement of surface exchange coefficient, k_{chem}, and chemical diffusion coefficient of oxygen, $\widetilde{D}_O$, by conductivity relaxation was designed, constructed and used. Conductivity relaxation experiments were conducted on dense and porous samples of LSC, as a function of temperature and p_{O_2}. A method of analysis was developed, which gives an accurate measurement of k_{chem} and $\widetilde{D}_O$. The $\widetilde{D}_O$ was observed to be a function of temperature but not a function of p_{O_2}, over the range of p_{O_2} investigated. This is consistent with the expectation since oxygen vacancy concentration is virtually fixed by composition. The k_{chem}, however, depends on both temperature and p_{O_2}. The k_{chem} increases with increasing p_{O_2}, consistent with the occurrence of adsorption. At 800°C, the k_{chem} is on the order of 10^{-5} cm/s and the $\widetilde{D}_O$ is on the order of 10^{-7} cm^2/s. The threshold thickness, above which diffusion control occurs, is on the order of 100 microns. Experiments on LSM ($La_{0.8}Sr_{0.2}MnO_{3-\delta}$) showed that $\widetilde{D}_O$ is very low, and confirms the need to use LSM in combination with an oxygen ion conductor such as YSZ to ensure high cathodic activity (composite cathode). The observed better performance of LSC + SDC cathodes, as compared to LSM + YSZ, in part is attributable to high k_{chem} and $\widetilde{D}_O$.

A procedure was developed for the deposition of patterned electrodes with l_{TPB} varying between 50 and 1200 cm^{-1} on YSZ discs. This included the design of masks with various patterns. Techniques in photomicrolithography were used to deposit LSM grid patterns on YSZ discs. Using complex impedance spectroscopy, cathodic charge transfer resistance was measured as a function of temperature and p_{O_2}. It was observed that a plot of $1/R_{ct}$ vs. l_{TPB} was linear, consistent with the occurrence of charge transfer at TPB. The observed p_{O_2} dependence was consistent with adsorption as an important step in charge transfer.

[1] The deposition of LSC on YSZ was achieved at low temperatures. Also, the maximum test temperature was 800°C. It is anticipated that at 800°C, there is negligible reaction between LSC and YSZ. For use of LSC in cells, however, a barrier layer of SDC is deposited on YSZ. This is because the cathode firing temperature for cells is generally high – typically 1150°C.

Specifically, a plot of $R_{ct} p_{O_2}$ vs. p_{O_2} was linear, the slope of which gives a relative measure of the adsorption of O_2 and N_2. Preliminary work was also done with LSC patterned electrodes. In this case also, the plot of $R_{ct} p_{O_2}$ vs. p_{O_2} was linear.

Preliminary work has been done on the fabrication and testing of anode-supported button cells with hydrogen as fuel and oxidants containing O_2 and, N_2, or Ar or CO_2 as diluents. The initial slopes of the voltage vs. current density traces were analyzed to approximately estimate the effective cathodic charge transfer resistance or polarization resistance. With CO_2 as the diluent, the polarization resistance was lower, which suggests a lower tendency for the adsorption of CO_2 as compared to N_2 and Ar, on a relative basis. The results indicated that adsorption-related issues are important.

EXPERIMENTAL

(a): LSC Sample Fabrication and the Measurement of k_{chem} and $\widetilde{D}_O$ by Conductivity Relaxation:

Synthesis of Powders: Sr-doped Lanthanum Cobaltite (LSC) in the ratio $La_{0.6}$ to $Sr_{0.4}$ was chosen as a suitable stoichiometry for the test samples. Oxygen vacancy concentration, and hence p-type conductivity, is known to increase with lower-valent A-site doping. However, the stability of single phase LSC, with temperature and ambient Po_2, is sacrificed with increased doping. Doping beyond $Sr_{0.5}$ is known to cause phase instability and thus $La_{0.6}Sr_{0.4}CoO_3$ was chosen as the best compromise.

Starting powders of La_2O_3, $SrCO_3$ and Co_3O_4 in the correct stoichiometric ratio for $La_{0.6}Sr_{0.4}CoO_3$ were ball-milled in ethanol for 24 hours. The slurry was dried and calcined at 1100°C for 12 hours to synthesize the precursor LSC powder. The calcined powder was ball-milled again in ethanol for 24 hours. The slurry was dried and sieved before fabrication into bars.

Fabrication of Dense, MIEC Samples: The bars were pressed and sintered from the powder as required. Typical fabrication of dense bars involves uniaxial pressing of ~3.5 g of sieved powder at 12,000 lbs for 1 minute. The green bars were then sintered at 1250°C for 6 hours to form dense MIEC of over 99% theoretical density. It was found that bars produced with only uniaxial pressing were sometimes prone to the formation of internal voids, which became exposed during polishing. This problem was solved by isostatically pressing the uniaxially pressed bars at 32,000 psi before sintering.

Dense $La_{0.6}Sr_{0.4}CoO_3$ bars were ground and polished for conductivity relaxation. Dense samples of 150 and 218 μm thicknesses and width 10 mm were fabricated, followed by polishing and finishing operations. Silver electrodes using mesh and paste were attached in a 4-probe configuration.

Fabrication of Porous MIEC Samples: The standard procedure to produce porous samples is to mix carbon particles in the green powder before pressing and sintering. The approach is to slow burn the carbon out of the pressed samples before reaching the sintering temperature, leaving a porous microstructure in the finished bar.

Starting powders of La_2O_3, $SrCO_3$ and Co_3O_4 (as used for the dense samples) in the correct stoichiometric ratios were ball-milled in ethanol for 24 hours. The slurry was dried and calcined at 1100°C for 12 hours to synthesize LSC powder. The powder was mixed with 13 wt.% of carbon (10-20 μm spherical particles) and ball-milled again in ethanol for 24 hours. The dried slurry was mixed with 2 to 3 wt.% ethylene glycol (as binder) and pressed into bars (uniaxially at 7,000 lbs for one minute and then isostatically at 32,000 psi). The bars were initially heated at 1°C/min in air to 500°C (for carbon burn-out) and then sintered at 1150°C for 4 hours.

Characterization: $La_{0.6}Sr_{0.4}CoO_3$ powder used for bar samples was analyzed by XRD to check for phase purity. Limited BET, EDS and SEM characterization was done on selected samples.

Electrochemical Measurements on the Kinetics of Oxygen Incorporation using Conductivity Relaxation: The bar samples (dense as well as porous) were used for conductivity relaxation measurements. The distance between the inner voltage probes was approximately 20 mm and between the outer current probes was approximately 30 mm. Two different chambers have been used in this work. The initial one was somewhat larger, which required longer time for gas exchange. The one recently designed is small, in which the gas can be completely exchanged in less than 2 seconds. In any given test, a sample was mounted in the oxygen exchange reactor. Conductivity relaxation tests were carried out on LSC samples over a range of temperatures between 700 and 800°C. The applied DC voltage across the outer probes was such that a current of 0.2 A flows through the sample. In some experiments, the applied voltage was large enough so that the current was 0.4 A. All experiments were conducted under constant current conditions.

Initially, air was circulated past the sample. After achieving an equilibrated state, the atmosphere in the chamber was abruptly switched to a different p_{O_2}, and the time dependence of the voltage across the inner probes was recorded. Experiments were conducted over a wide range of p_{O_2}, typically ranging between ~0.01 atm and ~0.21 atm. In some cases, the tests were conducted at p_{O_2} as low as 0.001 atm. The step change in p_{O_2}, that is Δp_{O_2}, was as small as 0.02 atm, although in many cases, the Δp_{O_2} was large, typically 0.05 to 0.1. In some cases, the Δp_{O_2} was as large as 0.2 atm. Tests were performed in increasing steps of Δp_{O_2} ($\Delta p_{O_2} > 0$), as well as in decreasing steps of Δp_{O_2} ($\Delta p_{O_2} < 0$). The data were analyzed to obtain both k_{chem} and $\tilde{D}_O$. The following procedure was used.

A normalized conductivity function, $g(t)$, was defined as

$$g(t) = \left| \frac{\sigma(t) - \sigma(0)}{\sigma(t) - \sigma(\infty)} \right| \tag{4}$$

where $\sigma(t)$ is the conductivity at time 't'. Analysis of combined surface exchange and bulk diffusion has been given by Crank [14]. The $g(t)$ is given by

$$g(t) = 1 - \sum_{n=1}^{\infty} \frac{2L^2 \exp\left[-\frac{\beta_n^2 \tilde{D}_O t}{l^2} \right]}{\beta_n^2 \left(\beta_n^2 + L^2 + L \right)} \tag{5}$$

where l is the half sample thickness,

$$L = \frac{l k_{chem}}{\tilde{D}_O} \tag{6}$$

and β_n are the roots of the transcendental equation $\beta_n \tan \beta_n = L$. It can be shown (by expanding the above in a Taylor's series) that the plot of $\frac{g(t)}{\sqrt{t}}$ vs. $\sqrt{t}$ as $t \to 0$ should be a straight line with slope equal to lk_{chem}. Thus, from the slope, k_{chem} can be obtained, and then by fitting the $g(t)$ function, the $\widetilde{D}_O$ can be obtained.

Conductivity relaxation experiments were also conducted on porous samples. In this case, the diffusion distance is only a few microns, and the kinetics are controlled by k_{chem} only. The kinetics then can be described by a simple first order kinetic equation. This aspect will be described later. Details are given in Appendix-II.

(b) The Measurement of R_{ct} using Patterned Electrodes:

The work on patterned electrodes was supported in part on funding by DOE through PNNL to the University of Utah in the form of a graduate student fellowship. Part of the experimental work was done on site at PNNL in the EMSL laboratory.

Fabrication of YSZ Discs for Patterned Electrodes: Discs of YSZ were fabricated using conventional ceramic processing methods involving die pressing of powder compacts followed by sintering in air. The YSZ powder was obtained from Tosoh Corporation, Japan. Nearly 10 gm of the powder was used to prepare each disc. The powder was pressed in a circular die using a uniaxial press at nearly 10,000 lb. The discs obtained were then sintered at 1500^{o}C for 5 hours in air. The discs after sintering had dimensions of approximately 24 mm diameter and 3.5 mm thickness. One surface of each disc was polished such that the surface roughness was nearly 1 micron. After polishing, a groove was made along the cylindrical surface of the discs at a distance of nearly 1.5 mm from the polished surface. The discs were then cleaned in soap solution followed by rinsing in acetone and then in de-ionized water and dried at 500^{o}C for 2 hours.

Deposition of LSM Patterned Electrodes by Photomicrolithography: LSM patterned electrodes corresponding to wide range of l_{TPB} were fabricated on the polished surfaces, in a circular area of 1 cm diameter at the center of the discs, using photolithographic and sputtering techniques. The LSM electrodes of nearly 0.5 micron thickness were sputter deposited from a $La_{0.8}Sr_{0.2}MnO_3$ target by RF sputtering using argon plasma. The YSZ discs were held at a distance of 15 cm from the target and were at room temperature during sputtering. The chamber pressure was kept at a minimum (2 mTorr) to obtain a dense LSM thin film. The deposition rate was nearly 5 nm per minute. The discs with patterned electrodes were later annealed at 1000^{o}C for 2 hours. X-ray Diffraction (XRD) patterns of the as sputtered and annealed LSM film were obtained. The electrode morphology was analyzed before and after annealing and after electrochemical testing using an optical profilometer and a scanning electron microscope (SEM).

A counter electrode of platinum was applied using platinum resinate, in a circular area of 1 cm diameter at the center of the opposite face of the discs so that it is symmetric with respect

to the LSM working electrode. The discs were again annealed at 900^{o}C for 2 hours to remove the organic components of the platinum resinate and to obtain a well bonded porous platinum counter electrode. A platinum reference electrode in the form of a ring was attached along the groove in the cylindrical surface of the disc.

Electrochemical Testing of Patterned Electrodes: Platinum mesh was used as a current collector on both working and counter side. The cell was assembled between two alumina rings with the help of two threaded rods, springs and wing nuts. Care was taken to make sure that both the electrodes are completely exposed to the external atmosphere. Electrical connections were taken out, by connecting platinum wires to the platinum mesh. The assembled cell was then placed inside an alumina tube such that the cell was near the closed end of the tube, with the working electrode always facing the closed end of the tube. The tube was tightly sealed with a rubber cork. Holes were drilled in the cork through which the platinum leads for electrical connection and the rods to hold the cell were inserted. A gas inlet and an outlet were also inserted into the rubber cork. The inlet tube was long enough to release the gas very close to the working electrode of the cell. The alumina tube containing the cell assembly was then placed in a horizontal tube furnace such that the cell was positioned at the center of the furnace. A thermocouple tip was placed very close to the cell to measure the temperature at the cell and correlate with that indicated by the furnace controller. The inlet tube was connected to compressed gas cylinders with premixed gas compositions. A flow rate of nearly 200 ml/minute was used to continuously circulate the respective premixed gas of desired oxygen partial pressure. While changing the temperature or pressure, the system was allowed to equilibrate for two hours before doing any measurements.

Impedance spectra were obtained using Solatron Impedance/gain-phase analyzer (SI-1260) in combination with Solatron Electrochemical Interface (SI-1287), over a range of temperatures between 500 and 800^{o}C in gas mixtures of oxygen partial pressure ranging from 0.01 to 1 atm. Polarization measurements were also carried out using the Solatron Electrochemical Interface (SI-1287).

(c): Fabrication and Electrochemical Testing of Button Cells in Various O_2 + Diluent Gas Mixtures:

Fabrication of Anode-Supported Cells: The following describes the generic cell fabrication procedure used. Anode-supported cells with Ni + YSZ as the anode, YSZ electrolyte, a thin, dense layer of Sm_2O_3-doped CeO_2 (SDC) barrier layer which serves as a part of the electrolyte, Sr-doped $LaCoO_3$ (LSC) + SDC porous cathode, and a porous LSC layer as a current collector, were fabricated using the following procedure. Discs of NiO + YSZ powder mixture were die-pressed. A thin layer of NiO + YSZ was applied by slurry coating. A thin layer of YSZ was the applied on the surface, and also along the edges, by drop coating a YSZ slurry. After drying, a thin layer of SDC was also applied by drop coating. The disc was subsequently sintered in air at a temperature between 1400 and 1500^{o}C. Similar cells were also made with LSM + YSZ as the composite cathode. In this case, no SDC barrier layer was required.

Cell Testing: The following procedure was used for testing fuel cells. A cell was mounted in a fixture using alumina tubes and flexible, glass-free, compression seals. Silver wire meshes, in the same geometry as the electrode areas, were placed on the cathode. Silver wire leads were connected to the wire meshes. The cell was heated in a furnace to 800°C. Hydrogen gas, bubbled through water, was circulated past the anode. The cell was tested in three types of oxidants; $O_2 + N_2$, $O_2 + Ar$, and $O_2 + CO_2$. The objective was to determine the possible effect of inert gas on cell polarization. The O_2 content was varied between ~5% and ~100%.

RESULTS AND DISCUSSION

(a): The Measurement of k_{chem} and $\tilde{D}_O$ by Conductivity Relaxation:

Sample Fabrication and Sample Housing Chamber: Figure 1 is a photograph of a sample of LSC of ~218 microns used in conductivity relaxation studies. The sample is introduced into a one end closed quartz tube. An alumina tube for feeding gas is inserted from the open end of the tube such that the end of the feeding tube is very close to the sample. Most of the initial studies were conducted using this set up. The time required for complete gas exchange is rather long – several seconds. Subsequently, a smaller chamber has been designed and constructed, shown in Figure 2. The set up is equipped with a four-way switch for rapid switching of atmosphere. The switching time is estimated to be less than 2 seconds. Figure 3 shows the 218 micron sample in the new chamber. Sample shown in Figures 1 and 3 is a fully dense sample (less than 2% porosity). Several experiments were also conducted on porous samples. Figure 4 shows an SEM micrograph of a porous sample. Conductivity relaxation experiment for the porous samples gives an effective surface exchange coefficient, k_{eff}, defined by

$$g(t) = 1 - \exp\left[-k_{eff}\, t\right] \tag{7}$$

where the units of k_{eff} are sec^{-1}, and is related to k_{chem} by the following relation, namely,

$$k_{eff} = S_v k_{chem} \tag{8}$$

where S_v is the pore surface area per unit volume. The above equation is applicable if the grain or particle size in the porous sample, d, is much smaller than the threshold thickness, $\lambda = \frac{\tilde{D}_O}{k_{chem}}$; that is as long as $d << \lambda$. The S_v was determined using quantitative stereology to be ~7,900 cm^{-1}.

The Effect of (Dense) Sample Thickness on the Estimation of k_{chem}: The Validity of the Approach: As stated earlier, the approach for the measurement of k_{chem} and $\tilde{D}_O$ using dense samples consists of plotting $g(t)/\sqrt{t}$ vs. $\sqrt{t}$, the slope of which as $t \to 0$ is given by k_{chem}/l where l is the half sample thickness. Figure 5 shows plots of $g(t)/\sqrt{t}$ vs. $\sqrt{t}$ at 800°C, for samples of two thicknesses, 150 and 218 microns, for p_{O_2} change from 0.05 to 0.1 atm (old chamber). Note the linear portions of the plots as $t \to 0$. Note also that the slope

is higher for the thinner sample. The k_{chem} estimated is the same. In order to obtain $\widetilde{D}_O$, however, it is necessary to fit the entire curve.

Estimation of the k_{chem} by Conductivity Relaxation on Porous Samples: As stated above, in such a case, it is possible that $d << \lambda$. This implies that the oxygen exchange process is interface-controlled, for which the kinetics are described by equation (7). Figure 6 shows a plot of $g(t)$ vs. t for a porous LSC sample at 800°C for a p_{O_2} change from 0.21 to 0.18 atm. The governing kinetic equation is given in the inset. The k_{eff} is estimated to be ~0.268 sec^{-1}. From the specific pore surface area, S_V of ~7900 cm^{-1}, determined by quantitative stereology, the k_{chem} is determined to ~3.4 x 10^{-5} cm/sec, which is in good agreement with that measured using the dense sample. Considerable work has been conducted in our lab on the measurement of k_{chem} using porous samples. This is described in detail in Appendix-II, which is a copy of a manuscript recently submitted for publication in the *Journal of the Electrochemical Society*.

The Effect of p_{O_2} on k_{chem}: Experiments with Dense Samples: Determination of k_{chem} as a function of p_{O_2} is difficult because the experiment consists of measuring the change in $g(t)$ when the p_{O_2} is changed abruptly from one value to another. In principle, an approximate value can be obtained at an average value of p_{O_2}, given by

$$p_{O_2}(mean) = \frac{p_{O_2}(initial) + p_{O_2}(final)}{2} \tag{9}$$

where $\Delta p_{O_2} = \left| p_{O_2}(initial) - p_{O_2}(final) \right|$ is as small as possible. If the Δp_{O_2} is too small, however, the sensitivity is poor. Reasonable accuracy can be obtained provided Δp_{O_2} is not too small. Also, it has been observed that the k_{chem} obtained using dense samples during increasing p_{O_2} is generally different (larger) than during decreasing p_{O_2}. Figure 7 shows plots of $g(t)/\sqrt{t}$ vs. $\sqrt{t}$ for a dense sample of LSC of thickness 218 microns tested at 800°C. The p_{O_2} was changed from high to low.

Figure 8 shows a plot of k_{chem} as a function of p_{O_2} (measured during decreasing p_{O_2}) at 800°C, measured on the 218 micron dense sample (new chamber). The Δp_{O_2} was ~0.02 atm. Measurements were conducted at two different values of current; 0.2 and 0.4 A. Note that there is not a significant effect – although the k_{chem} values are somewhat smaller for measurements conducted at higher current. It is not clear if this is a real effect. More experiments are underway to make a definitive determination.

Measurement of k_{chem} using Porous Samples: Figure 9 shows Plots of k_{chem} vs. p_{O_2} at 800°C, during both increasing and decreasing p_{O_2}, measured using the porous sample. For the reasons stated in the text, the measurement of k_{chem} using porous samples is expected to be more accurate. Note that at low values of p_{O_2}, the k_{chem} is virtually the same either during increasing p_{O_2} or decreasing p_{O_2}. The variance at high p_{O_2} may be experimental scatter. Note that k_{chem} increases with p_{O_2}, and seems to plateau at high p_{O_2}, which would be consistent with an adsorption isotherm, such as Langmuir. Considerable work has been conducted on the measurement of k_{chem} using porous samples. These are described in detail in Appendix-II, which is a copy of a manuscript recently submitted for publication in the *Journal of the Electrochemical Society*.

(b): The Measurement of R_{ct} using Patterned Electrodes:

The work on patterned electrodes was also supported in part on funding by DOE through PNNL to the University of Utah in the form of a graduate student fellowship. Part of the experimental work was done on site at PNNL in the EMSL laboratory.

LSM Patterned Electrodes and Preliminary Results: Figure 10 shows an SEM image of a LSM patterned electrode deposited on a YSZ disc. The square regions are of YSZ, in which the YSZ grains can be seen. The rest of the region is the sputtered LSM coating. The l_{TPB} of this sample is 500 cm^{-1}. Figure 11 shows the corresponding profilometric trace. Figure 12 shows impedance spectra on LSM patterned electrodes with different l_{TPB}, taken at 800°C in air. Note that the higher the l_{TPB}, the smaller is the impedance arc, which is a measure of the overall charge transfer resistance. Figure 13 shows plots of $1/R_{ct}$ vs. l_{TPB} at various temperatures, also in air. Note that plots are straight lines. The slope of each line is $1/\rho_{ct}$, where ρ_{ct} is the charge transfer resistivity. As seen in the figure, note that the ρ_{ct} decreases, as the temperature increases. Figure 14 shows the temperature dependence of the impedance spectra. These results show strong temperature dependence. Figure 15 is an Arrhenius plot of the measured R_{ct} for LSM patterned electrodes of two different l_{TPB}. The estimated activation energy is ~121 kJ/mol, indicating a strong temperature dependence.

The Effect of Oxygen Partial Pressure: Figure 16 shows impedance spectra on LSM patterned electrodes as a function of partial pressure of oxygen, p_{O_2}, in O_2-N_2 gas mixtures as oxidant. Note the profound effect of p_{O_2} on the impedance spectra. The R_{ct} is the intercept of the approximate semicircle, minus the high frequency intercept – which is the ohmic part.

Dependence of R_{ct} on p_{O_2}: Issues Related to Adsorption: As stated earlier, an important objective of the proposed work is to determine the possible role of adsorption on the cathodic

reaction, with particular emphasis on the role of inert gases. Our theoretical model shows that the expected relation between R_{ct} and p_{O_2}, with the inert gas being N_2, is given by

$$R_{ct}\,p_{O_2} = \frac{\rho'_{ct}\,(1+b'')}{l_{TPB}\,b'} + \frac{\rho'_{ct}\,(b'-b'')\,p_{O_2}}{l_{TPB}\,b'} \qquad (10)$$

where the total pressure is 1 atm. In the above equation, the ρ'_{ct} is the intrinsic charge transfer resistivity, which is independent of p_{O_2} (or θ_{O_2}), and is related to θ_{O_2} and ρ_{ct} by $\rho_{ct} = \frac{\rho'_{ct}}{\theta_{O_2}}$. Equation (10) suggests that a plot of $R_{ct}\,p_{O_2}$ vs. p_{O_2} should be a straight line with slope proportional to $\frac{\left(b' - b''\right)}{b'} = 1 - \frac{b''}{b'}$. Figure 17 shows plots of $R_{ct}\,p_{O_2}$ vs. p_{O_2} for LSM patterned electrodes on YSZ at various temperatures. Note that the plots are linear, in accord with equation (10). Also note that: (a) The slope is greater than zero, indicating that $b' > b''$, and (b) The slope decreases as the temperature increases. This implies at lower temperatures, the relative tendency of adsorption of O_2 in relation to N_2 increases. Alternatively, as the temperature is increased, the relative (not absolute) tendency for adsorption of N_2 increases. Part of the decrease in slope with increase in temperature is also due to decrease in ρ'_{ct} as the temperature increases. Detailed results, analysis and discussion of results is given in Appendix-I, which is a copy of a manuscript recently submitted for publication to the *J. of the Electrochemical Society*.

Preliminary work has also been conducted on LSC patterned electrodes deposited on YSZ, results of which are shown in Figure 18. The figure shows the plots of $R_{ct}\,p_{O_2}$ vs. p_{O_2} for LSC patterned electrodes on YSZ at various temperatures. Note that in this case also the plots are linear, in accord with the model. It is to be noted that in this case also the slope > 0, indicating that $b' > b''$.

Preliminary results on patterned electrodes have been described in the preceding paragraphs. Work is underway, and more results are expected in the next few months. Also, work will be initiated on LSF and other cathode materials.

(c): Electrochemical Testing of Button Cells in Various O_2 + Diluent Gas Mixtures:

Figure 19 shows an SEM image of a typical anode-supported cell used in the present work. Both the cathode and the anode are graded. Regions near the electrolyte/electrode are of fine porosity, for enhanced electrochemical activity. Regions away from the interfaces are of greater porosity, and of a coarse microstructure to minimize concentration polarization.

Single Cell Testing in Oxidants containing O_2 and Various Inert Gas Diluents: N_2, Ar, and CO_2: Figure 20 shows performance curves for a single cell tested with hydrogen as fuel and O_2 + N_2 gas mixtures (1 atm total pressure) as oxidant. Note that the maximum power density is ~2.9 W/cm^2 in 100% O_2, ~1.7 W/cm^2 in air (~21% O_2), but only ~0.6 W/cm^2 in ~5% O_2.

An important point to note is that the initial slope, that is, $\left|\frac{dV}{di}\right|_{i\to 0}$ is greater in oxidants containing low p_{O_2}. This indicates that at low p_{O_2}, the activation polarization is large – that is R_p increases as p_{O_2} decreases.

Figure 21 shows voltage and power density vs. current density plots for the cell in O_2 + Ar gas mixtures of various compositions as oxidant, ranging between ~5% O_2 + 95% Ar to ~100% O_2. Fuel: Hydrogen. Temperature: 800°C. These exhibit similar trends as with O_2 + N_2 gas mixtures as the oxidant. An important point to emphasize, however, is that it is not possible to assess the possible differences without actually determining $\left|\frac{dV}{di}\right|_{i\to 0}$, which contains the R_p.

Finally, Figure 22 shows voltage and power density vs. current density plots for the cell in O_2 + CO_2 gas mixtures of various compositions as oxidant, ranging between ~5% O_2 + 95% CO_2 to ~100% O_2. Fuel: Hydrogen. Temperature: 800°C. In this case also, the trend is similar. Thus, with all three diulents, the effects of adsorption appear to be important.

Figure 23 shows plots of the total resistance, R_t, as ($i \to 0$) vs. $\left(p_{O_2}\right)^{-1/2}$. The term that depends on p_{O_2} as $i \to 0$ is the cathodic polarization resistance, R_p. Thus, the dependence of R_t on p_{O_2} is a measure of the dependence of R_p on p_{O_2}. These results are obtained from cell measurements, in which the cathodes were composite (here LSC + SDC). The relevant equation, based on our model, is the polarization resistance for a porous composite cathode, given by

$$R_p \approx \sqrt{\frac{d\rho_i R_{ct}}{(1-V_v)}} = \sqrt{\rho_i \rho_{ct}}\sqrt{\frac{d}{l_{TPB}(1-V_v)}} = \sqrt{\rho_i \rho_{ct}^{'}}\sqrt{\frac{d}{l_{TPB}(1-V_v)}}\sqrt{\frac{1}{\theta_{O_2}}} \tag{11}$$

or

$$R_p \approx \sqrt{\rho_i \rho_{ct}^{'}}\sqrt{\frac{d}{l_{TPB}(1-V_v)}}\sqrt{\frac{1+b^{'}p_{O_2}+b^{''}p_{diluent}}{b^{'}p_{O_2}}} \tag{12}$$

or

$$R_p \approx \sqrt{\rho_i \rho_{ct}^{'}}\sqrt{\frac{d}{l_{TPB}(1-V_v)}}\sqrt{\frac{1+b^{''}}{b^{'}p_{O_2}}+\left(b^{'}-b^{''}\right)} \tag{13}$$

in which it is assumed the total pressure to be 1 atm; that is $p_{O_2} + p_{diluent} = 1$.
If the above is squared on both sides, one expects

$$R_p^2 \approx \rho_i \rho_{ct}^{'}\frac{d}{l_{TPB}(1-V_v)}\left(\frac{1+b^{''}}{b^{'}p_{O_2}}+\left(b^{'}-b^{''}\right)\right) \tag{14}$$

which would imply that a plot of $R_p^2 p_{O_2}$ vs. p_{O_2} should be a straight line, with slope proportional to $\left(b' - b''\right)$. Unfortunately, it is not possible to accurately obtain R_p. This is because it is not possible to accurately correct for the ohmic loss. Also, even as $i \to 0$, there is a contribution from cathodic concentration polarization, which depends upon p_{O_2}. All that is done here, therefore, is to plot R_p vs. $\left(p_{O_2}\right)^{-1/2}$, which is what is given in Figure 23. The plots are approximately linear. It is seen that the corresponding slope is much lower for CO_2 as the diluent. This seems to suggest that relative adsorption of CO_2 is less as compared to the other two diluents. Thus, the preliminary conclusion is that inert gas adsorption has an effect. But much more importantly is the issue of O_2 adsorption. For a good cathode, which is capable of functioning efficiently even at high oxidant utilization, the adsorption coefficient should be as high as possible. That is, it would be desirable to have θ_{O_2} vs. p_{O_2} adsorption plot plateau out at low values of p_{O_2}. Figure 24 shows a schematic of desirable and undesirable adsorption behavior. Figure 25 shows the measured $1/\rho_{ct}$ vs. p_{O_2} for LSC, with patterned electrodes at various temperatures.

CONCLUSIONS

Based on the work conducted during the course of this project (October 1, 2002 through December 31, 2003 – which includes a three-month no-cost extension), a number of conclusions have emerged. The most important one is that in a low p_{O_2} environment, the effective cathodic charge transfer resistance or polarization resistance, R_p, is higher, as measured from the actual cell measurements. These correlate well, at least qualitatively, with out-of-cell measurements on the two cathode systems studied, LSM and LSC. In the case of LSM which is a predominantly electronic conductor with a negligible ionic conductivity, the experimentally measured charge transfer resistivity, ρ_{ct}, using patterned electrodes, is found to increase with decreasing p_{O_2}. It was also observed that temperature dependence of ρ_{ct} can be described by an Arrhenius equation, with an activation energy on the order of ~120 kJ/mol. The ionic resistivity of YSZ used in composite cathode, namely ρ_i, is known to be nearly the same over a large range of p_{O_2}, as the vacancy concentration is fixed, by the Y content. Also, the temperature dependence of ρ_i is known to be thermally activated. Our model shows that the polarization resistance of a composite cathode, $R_p \propto \sqrt{\rho_{ct}\rho_i}$. Thus, the dependence of R_p estimated from cell measurements on p_{O_2}, is consistent with the dependence of ρ_{ct} on p_{O_2}.

In the case of LSC, which is a MIEC, in addition to the occurrence of charge transfer at TPB, there also is expected a significant cathodic reaction on the surface. The parameters which determine the polarization resistance in such a case are the surface exchange coefficient, k_{chem}, and the chemical diffusion coefficient of oxygen, $\widetilde{D}_O$. It can be shown that in this

case, $R_p \propto \frac{1}{\sqrt{k_{chem}\widetilde{D}_O}}$. Using the conductivity relaxation technique on dense and porous LSC, both k_{chem} and $\widetilde{D}_O$ were measured as a function of temperature and p_{O_2}. It was observed that k_{chem} increases with increasing p_{O_2}, while $\widetilde{D}_O$ is essentially independent of p_{O_2}. Both parameters are thermally activated. The dependence of R_p on p_{O_2} and temperature thus is qualitatively consistent with that of the $\frac{1}{\sqrt{k_{chem}\widetilde{D}_O}}$.

The dependence of ρ_{ct} and k_{chem} on p_{O_2} is consistent with an adsorption isotherm such as Langmuir. More work, however, will be needed in order to develop a quantitative correlation. A model for the charge transfer resistance, R_{ct}, on p_{O_2} through an adsorption isotherm shows that it should depend upon the adsorption characteristics of the inert gas, e.g. N_2. Preliminary work was carried out with oxidant made of gaseous mixtures of O_2 with N_2, Ar, and CO_2. Based on electrochemical measurements on cells, it was noted that the polarization resistance was lower in $O_2 + CO_2$ atmospheres as compared to that in $O_2 + N_2$ atmospheres. This observation can be rationalized on the premise that the adsorption of CO_2 occurs to a lower degree than that of N_2. These results are preliminary, and more work is needed. It is, however, clear that in order to lower the cathodic polarization resistance, it is necessary to have the adsorption coefficient of oxygen as high as possible, and that of the diluent as low as possible. Search for materials with high adsorption coefficient for oxygen should be fruitful.

The method of patterned electrodes has been found to be extremely valuable. This affords a direct method for the measurement of ρ_{ct} as a function of temperature and atmosphere (e.g. p_{O_2} and the partial pressures of other gaseous species) on a number of materials. Work is planned on the measurement of parameters, which dictate polarization resistance, and then compare results on actual electrochemical measurements on cells. The principal objective of the effort is to identify material combinations, which can exhibit good cathodic activity at low temperatures (as low as 600^{o}C) and in oxygen-depleted oxidant (at high oxidant utilizations).

Two manuscripts have been recently submitted for publication. One more will be submitted for publication over the next few months.

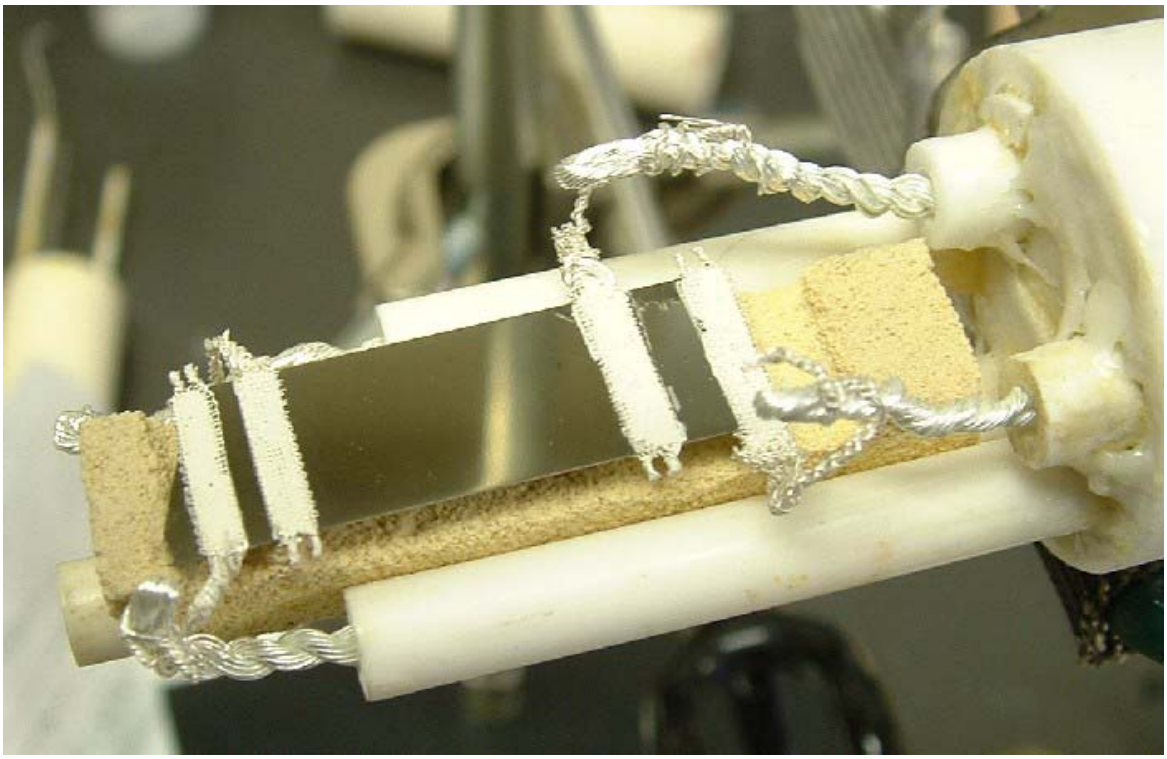


Figure 1: A sample of LSC of 218 μm thickness resting on a ceramic block. The assembly shown is inserted into a closed-end tube with a gas inlet and outlet.

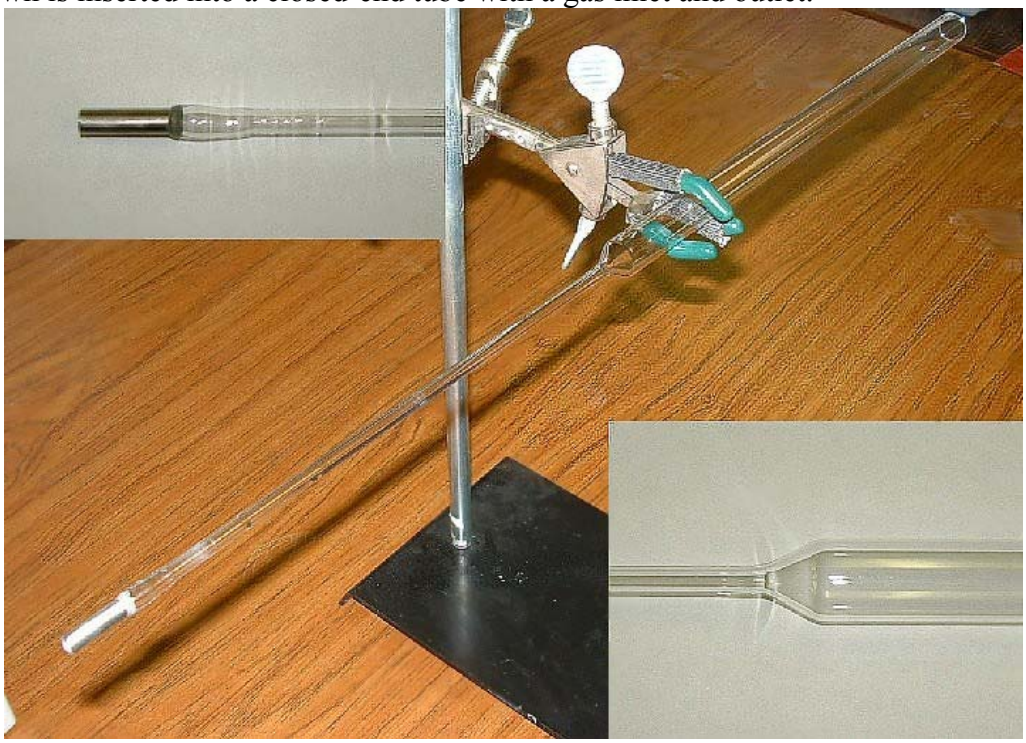


Figure 2: A photograph showing the smaller chamber used in later studies. The set up is equipped with a four-way valve for rapid switching of atmosphere. The switching time is less than about 2 seconds.

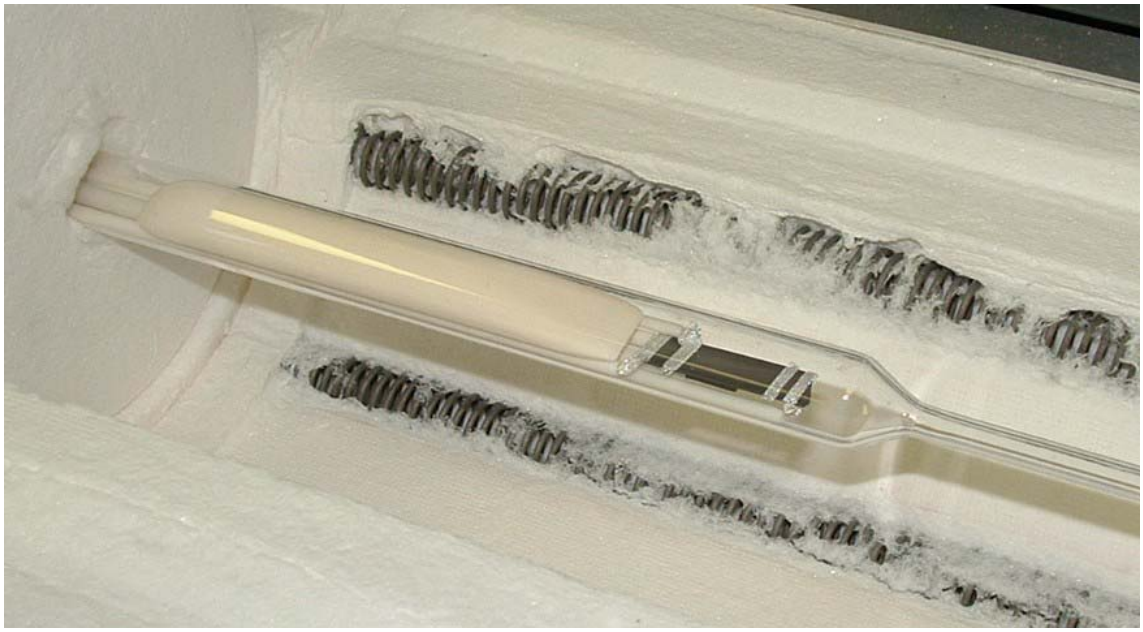


Figure 3: A photograph showing the 218 micron sample inside the new chamber, with a much smaller volume, and switching time < 2 seconds.

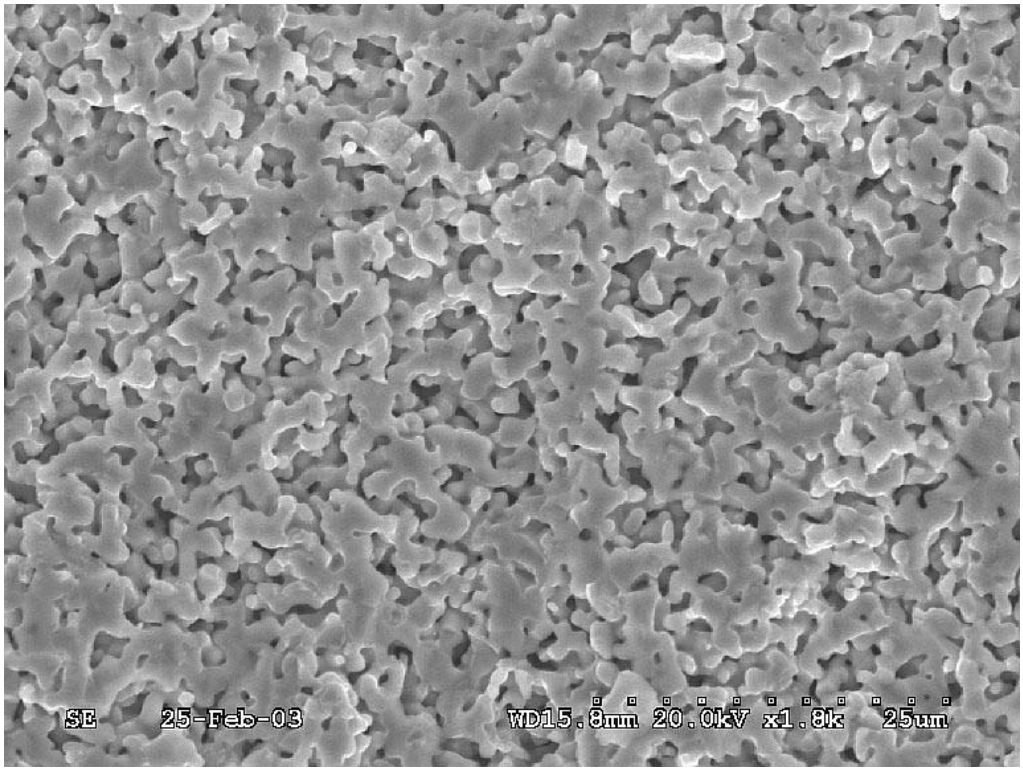


Figure 4: An SEM micrograph of a porous sample of LSC (30% porosity) used for the estimation of k_{chem} by the conductivity relaxation method.

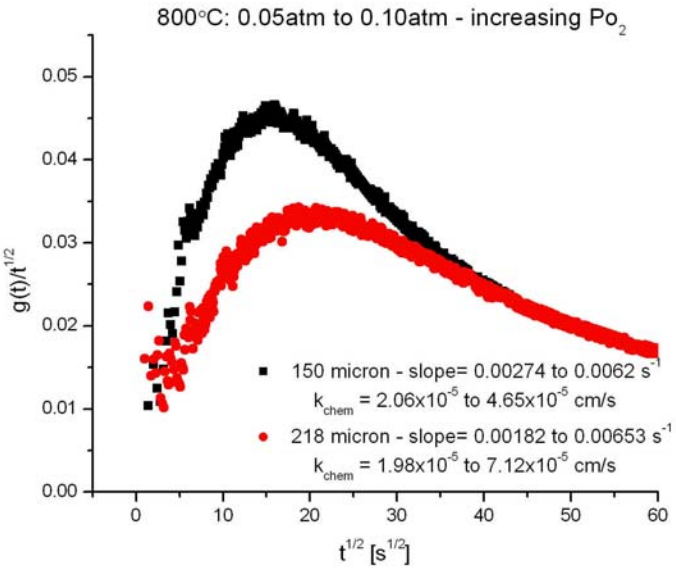


Figure 5: Plots of $g(t)/\sqrt{t}$ vs. $\sqrt{t}$ for samples of two thicknesses, 150 and 218 microns, at 800°C, for p_{O_2} change fro 0.05 to 0.1 atm (old chamber). Note that linear portions of the plots as $t \to 0$. Note also that the slope is higher for the thinner sample. The k_{chem} estimated is about the same.

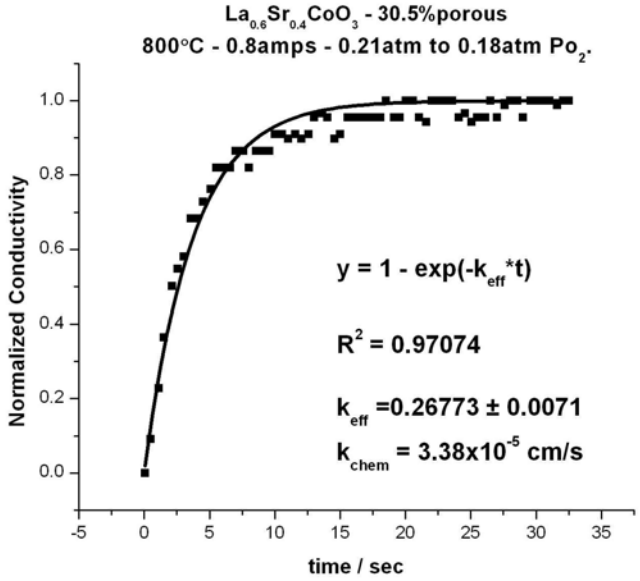


Figure 6: A plot of $g(t)$ vs. t for a porous LSC sample at 800°C for a p_{O_2} change from 0.21 to 0.18 atm. The governing kinetic equation is given in the inset. The k_{eff} is estimated to be ~0.268 sec^{-1}. From the specific pore surface area, S_v of ~7900 cm^{-1}, determined by quantitative stereology, the k_{chem} is determined to ~3.4 x 10^{-5} cm/sec, which is in good agreement with that measured using dense samples.

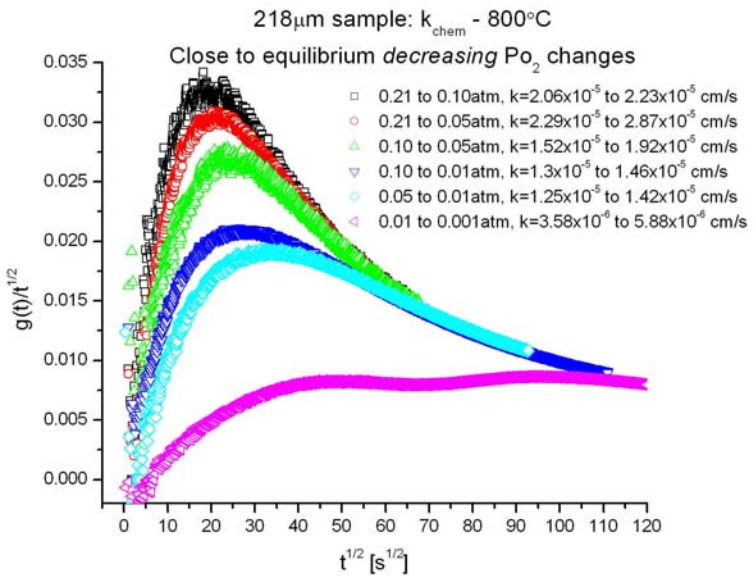


Figure 7: Plots of $g(t)/\sqrt{t}$ vs. $\sqrt{t}$ for a dense sample of LSC of thickness 218 microns tested at 800°C. The p_{O_2} was changed from high to low (old chamber).

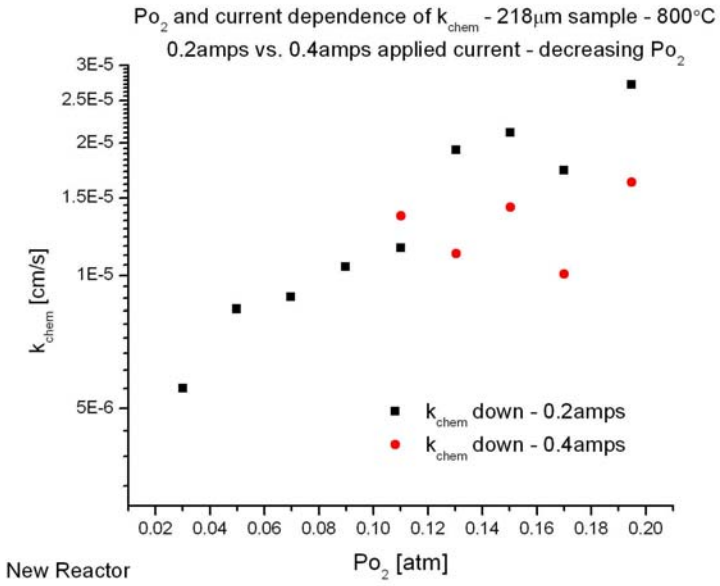


Figure 8: Plot showing k_{chem} as a function of p_{O_2} (measured during decreasing p_{O_2}) at 800°C, measured on the 218 micron sample (new chamber). The Δp_{O_2} was ~0.02 atm. Measurements were conducted at two different values of current; 0.2 and 0.4 A. Note that there is not a significant effect – although the k_{chem} values are somewhat smaller for measurements conducted at higher current. It is not clear if this is a real effect. More experiments are underway to make a definitive determination.

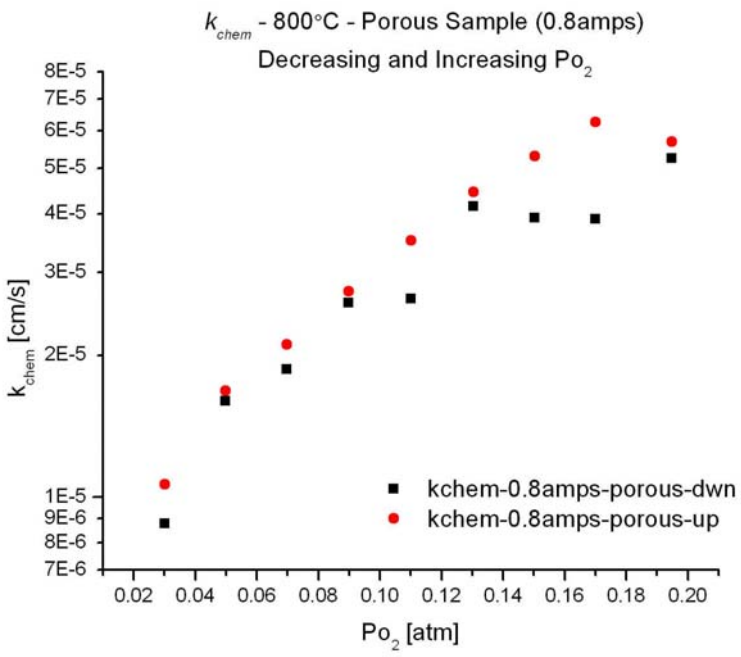


Figure 9: Plots of k_{chem} vs. p_{O_2} at 800°C, during both increasing and decreasing p_{O_2}, measured using porous sample. For the reasons stated in the text, the measurement of k_{chem} using porous samples is expected to be more accurate. Note that at low values of p_{O_2}, the k_{chem} is virtually the same either during increasing p_{O_2} or decreasing p_{O_2}. The variance at high p_{O_2} may be experimental scatter. Note that k_{chem} increases with increasing p_{O_2}. It is anticipated that at high p_{O_2}, it will plateau out, consistent with Langmuir type adsorption.

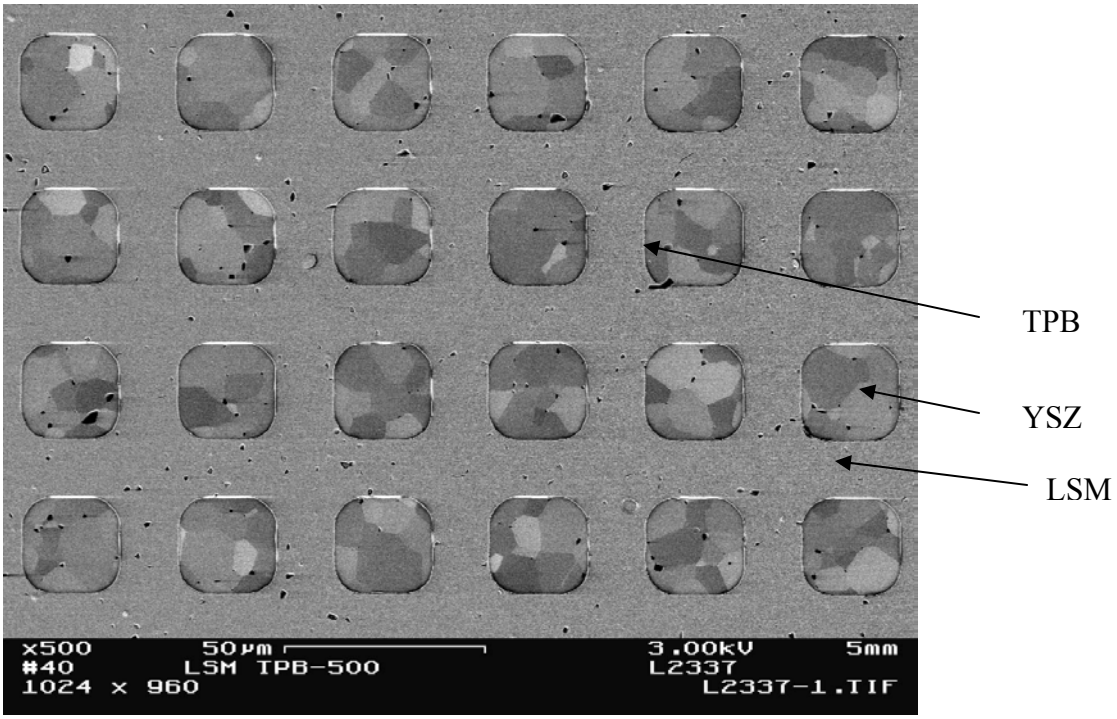


Figure 10: An SEM image of LSM patterned electrode deposited on a YSZ disc. The square regions are of YSZ, in which the grains can be seen. The rest of the region is the LSM coating. The l_{TPB} of this sample is 500 cm^{-1}.

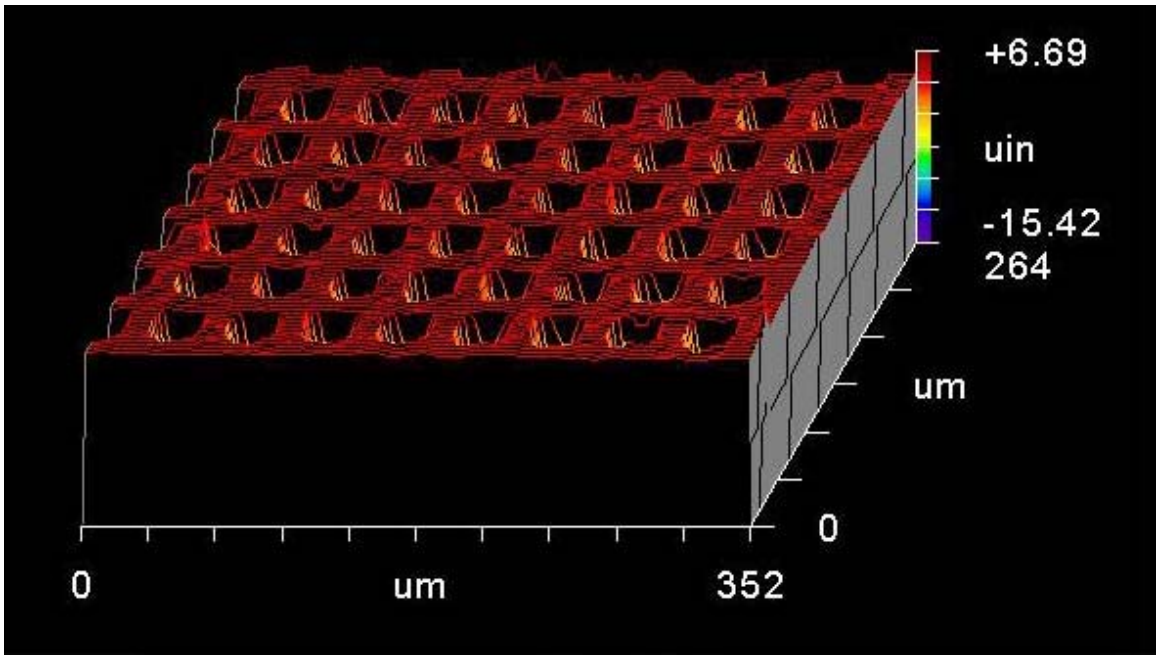


Figure 11: A profilometric trace of the patterned electrode.

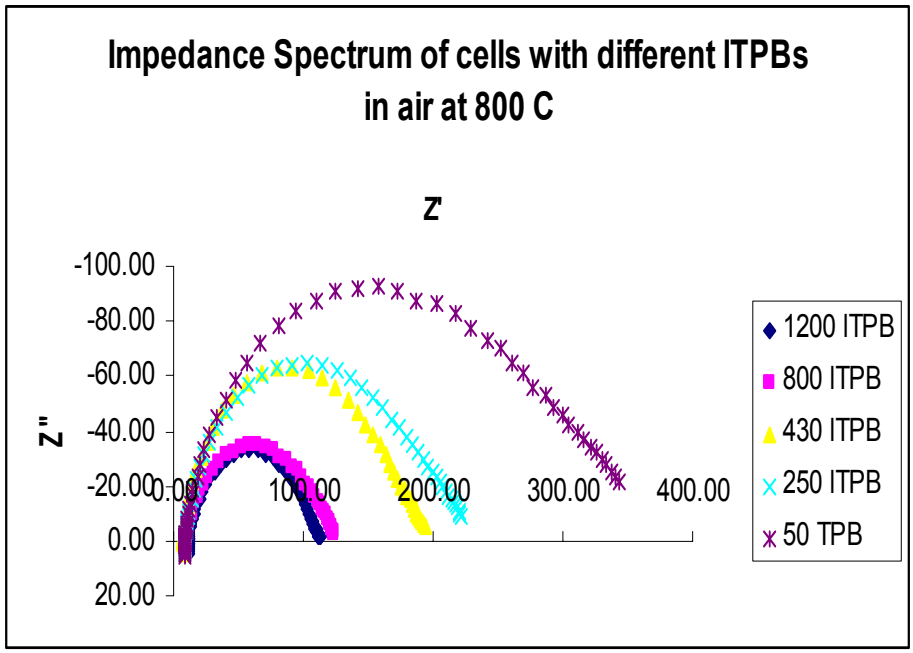


Figure 12: Impedance spectra on LSM patterned electrodes with different l_{TPB}, at 800°C in air.

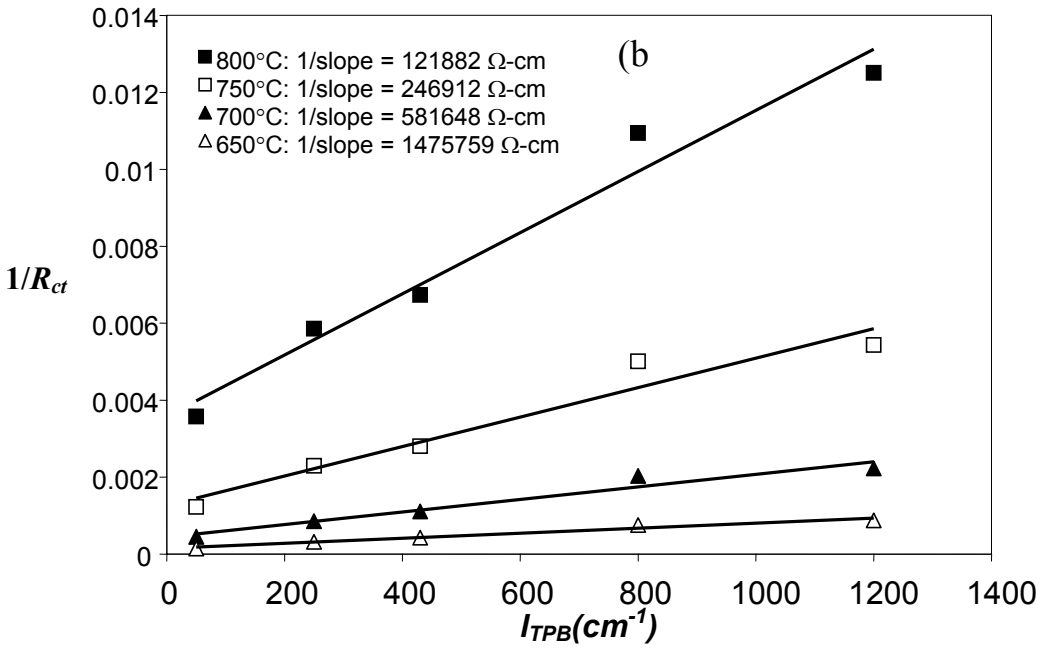


Figure 13: Plots of $1/R_{ct}$ vs. l_{TPB} at various temperatures, measured in air. Note that plots are straight lines. The slope of each line is $1/\rho_{ct}$, where ρ_{ct} is the charge transfer resistivity. As seen in the figure, the ρ_{ct} decreases, as the temperature increases.

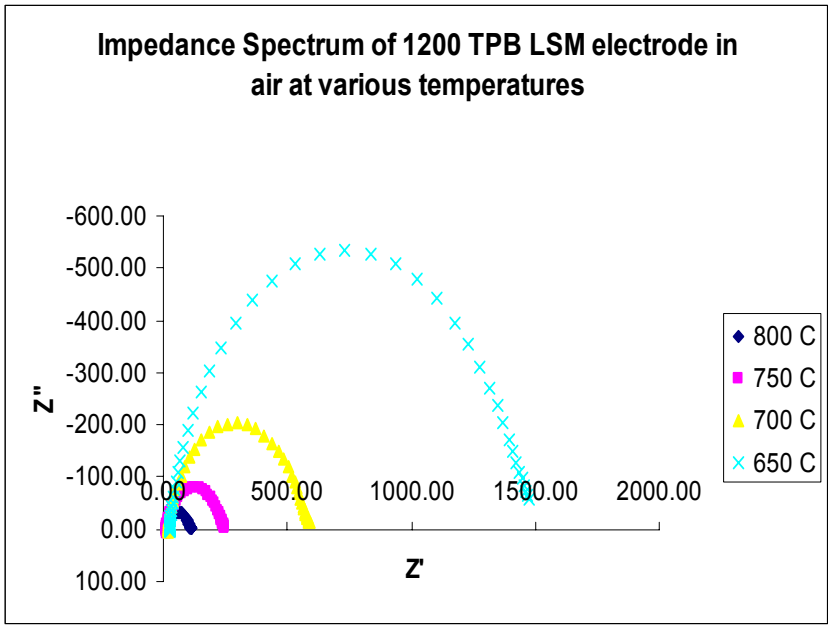


Figure 14: Impedance spectra on LSM patterned electrodes of $l_{TPB} \approx 1200$ cm^{-1}, in air at various temperatures.

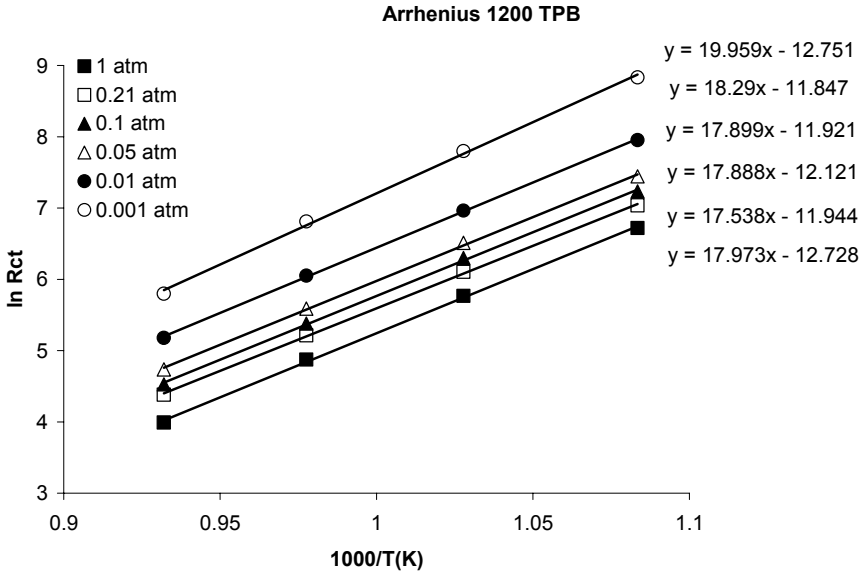


Figure 15: An Arrhenius plot of the measured R_{ct} for LSM patterned electrodes of two different l_{TPB}. The estimated activation energy is ~120 kJ/mol.

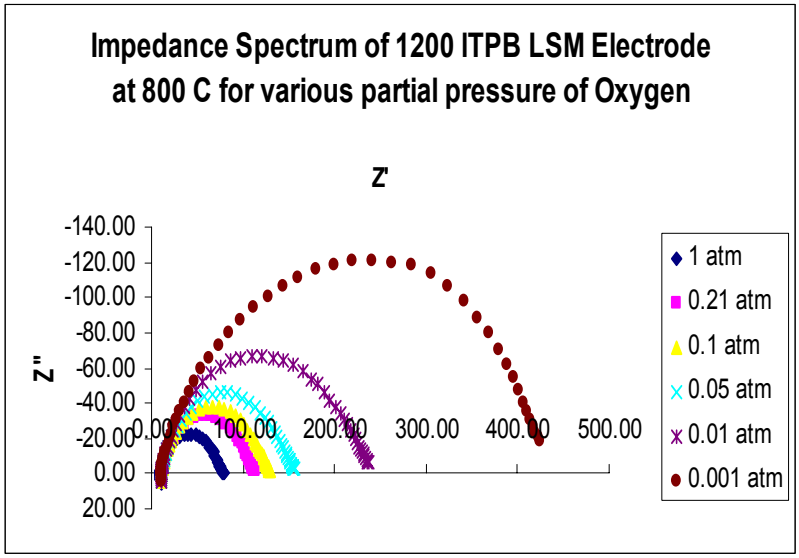


Figure 16: Impedance spectra on LSM patterned electrodes as a function of partial pressure of oxygen, p_{O_2}, in O_2-N_2 gas mixtures as oxidant.

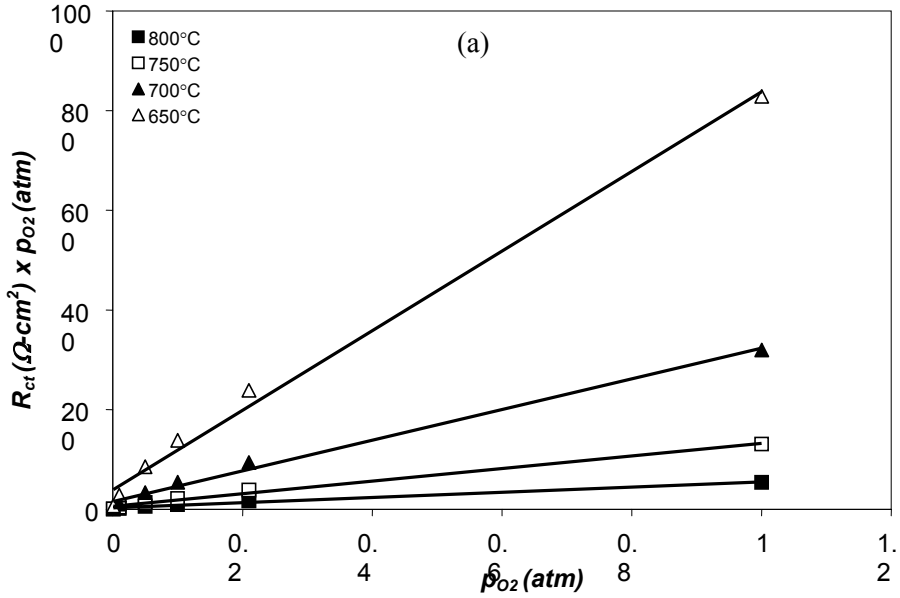


Figure 17: Plots of $R_{ct}\,p_{O_2}$ vs. p_{O_2} for LSM patterned electrodes on YSZ at various temperatures. Note that the plots are linear, in accord with equation (10). Also note that: (a) The slope is greater than zero, indicating that $b' > b''$, and (b) The slope decreases as the temperature increases. This implies at lower temperatures, the relative tendency of adsorption of O_2 in relation to N_2 increases. Alternatively, as the temperature is increased, the relative (not absolute) tendency for adsorption of N_2 increases. Also, it is to be noted that as the temperature increases, the ρ'_{ct} decreases. At the present time, sufficient information is not available to determine the relative contributions of these two effects.

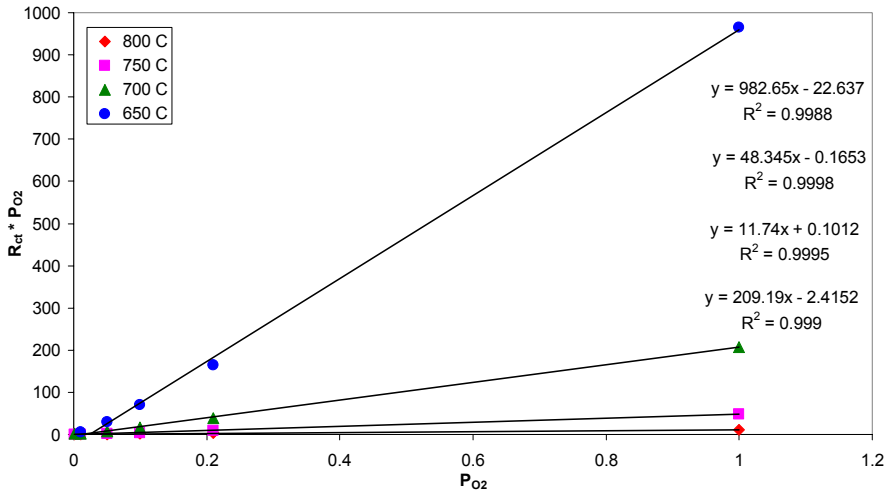


Figure 18: Plots of $R_{ct}p_{O_2}$ vs. p_{O_2} for LSC patterned electrodes on YSZ at various temperatures. Note that in this case also the plots are linear, in accord with the model. Also, it is to be noted that in this case also the slope decreases with increasing temperature. The intercept should be positive. The observation that it is negative can be attributed to experimental scatter. In order to accurately determine the intercept, data will have to obtained at several more p_{O_2} values. Also, the use of a sample with smaller value of l_{TPB} is preferred.

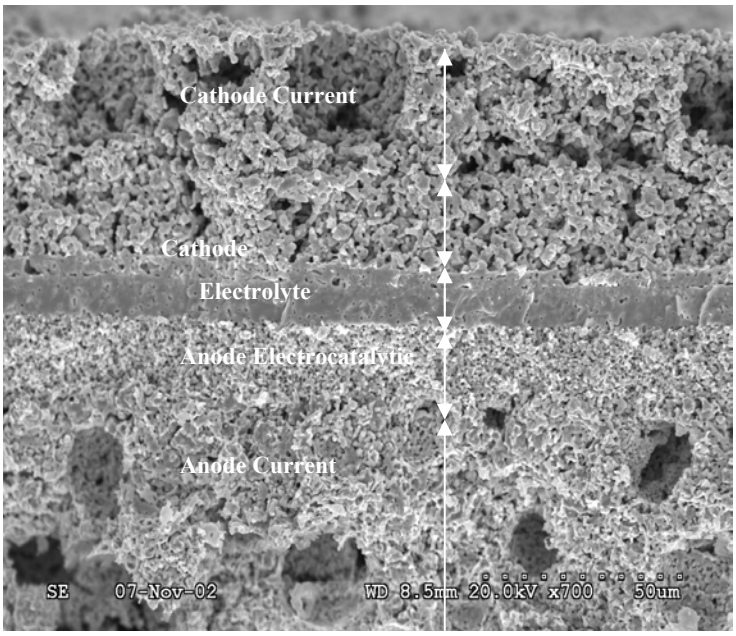


Figure 19: An SEM micrograph of a typical anode-supported cell used in the present work.

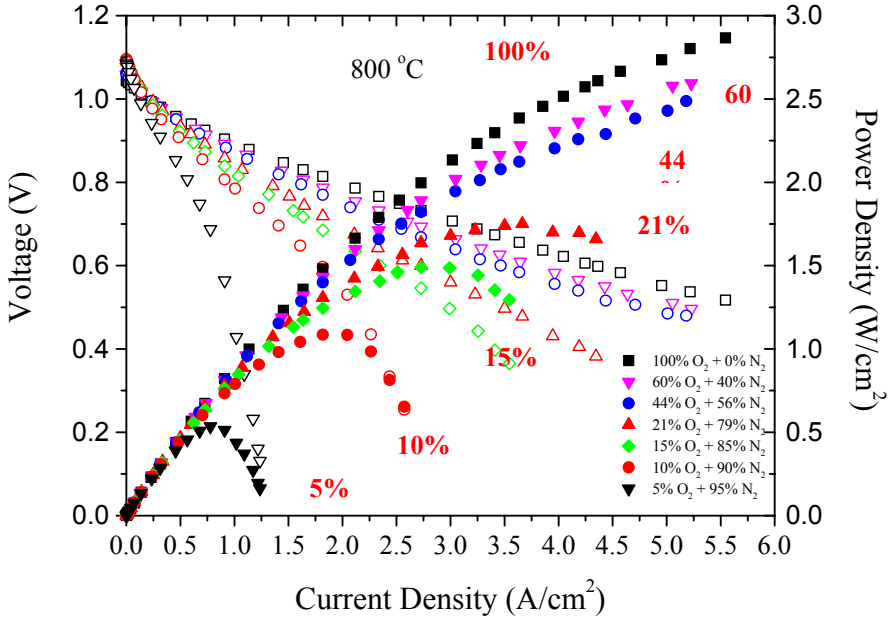


Figure 20: Voltage and power density vs. current density plots for a cell in oxidants of various compositions, ranging between ~5% O_2 + 95% N_2 to ~100% O_2. Fuel: Hydrogen. Temperature: 800°C.

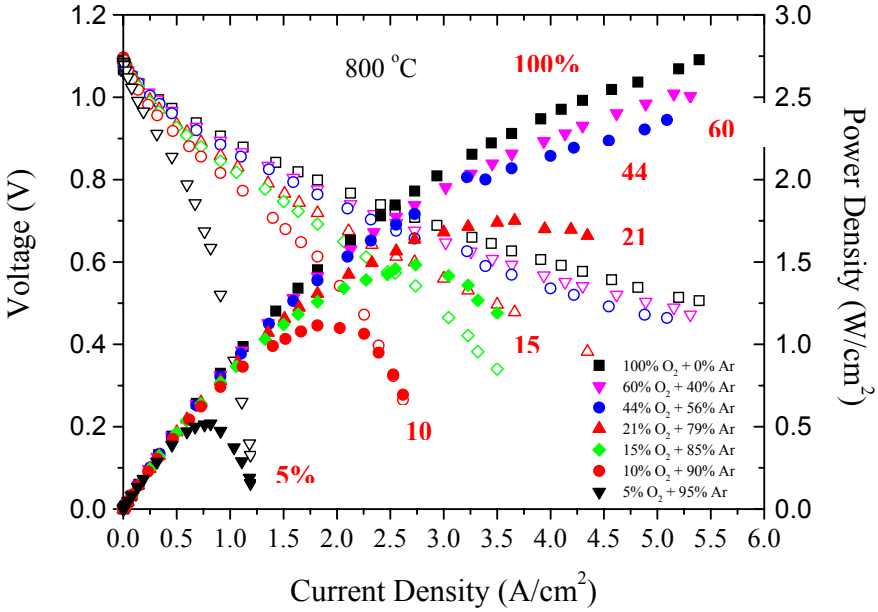


Figure 21: Voltage and power density vs. current density plots for a cell in oxidants of various compositions, ranging between ~5% O_2 + 95% Ar to ~100% O_2. Fuel: Hydrogen. Temperature: 800°C.

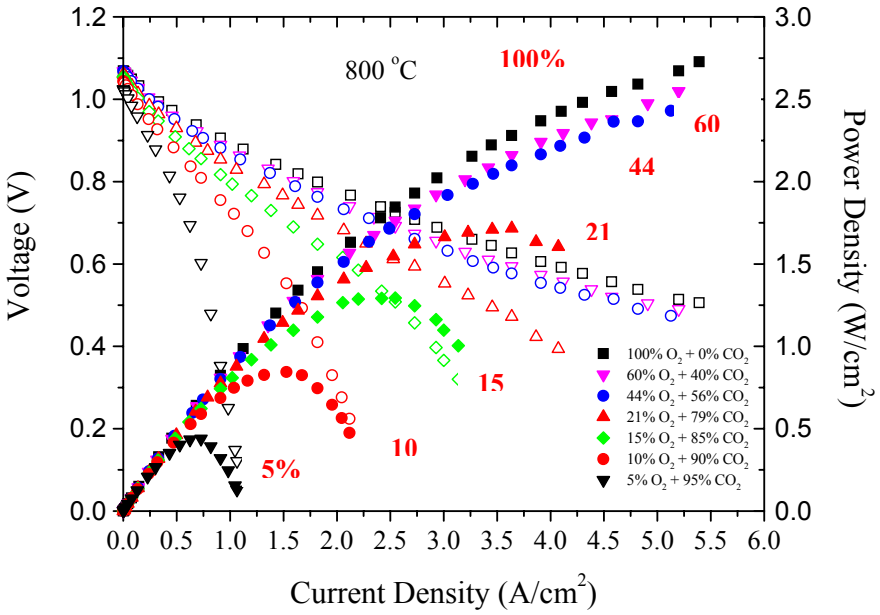


Figure 22: Voltage and power density vs. current density plots for a cell in oxidants of various compositions, ranging between ~5% O_2 + 95% CO_2 to ~100% O_2. Fuel: Hydrogen. Temperature: 800°C.

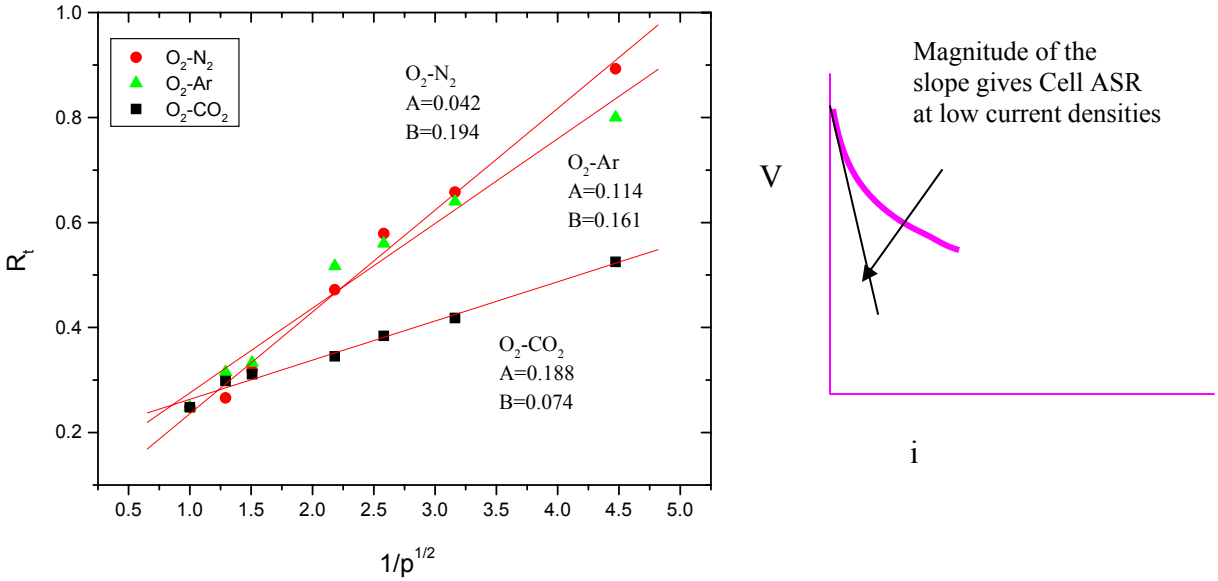


Figure 23: Plots of the total resistance, R_t, as $(i \to 0)$ vs. $\left(p_{O_2}\right)^{-1/2}$. The only term that depends on p_{O_2} as $i \to 0$ is the cathodic polarization resistance, R_p. Thus, the dependence of R_t on p_{O_2} is a measure of the dependence of R_p on p_{O_2}.

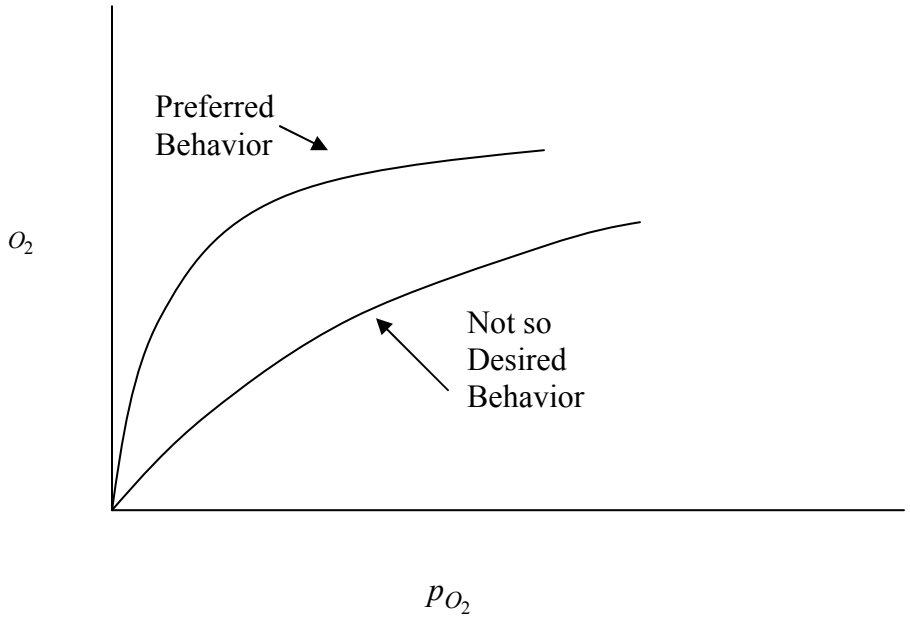


Figure 24: Schematics of the dependence of θ_{O_2} on p_{O_2}.

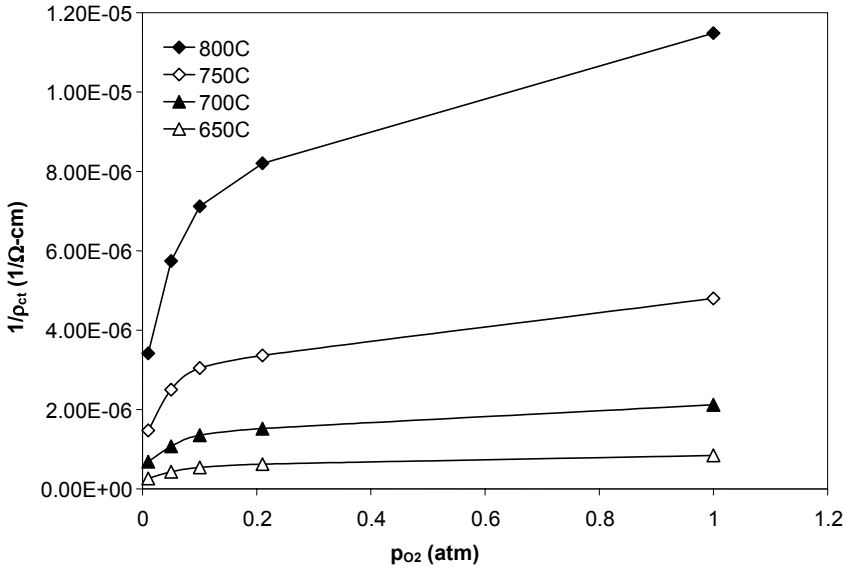


Figure 25: Experimentally measured $1/\rho_{ct}$ vs. p_{O_2} for LSC on YSZ at various temperatures. Note the similarity between Figure 24 (which gives schematics of the dependence of θ_{O_2} on p_{O_2}) and Figure 25.

REFERENCES

1) A. W. Adamson, '*Physical Chemistry of Surfaces*', John Wiley & Sons, New York, (1976).
2) B. K. Hodnett, '*Heterogeneous Catalytic Oxidation*', John Wiley, New York (2000).
3) T. Kenjo, S. Osawa, and K. Fujikawa, *J. Electrochem. Soc*., **138** 349 (1991).
4) I. V. Murygin, *Elektrokhimiya*, **23** [6] 740 (1987).
5) R. M. Thorogood, R. Srinivasan, T. F. Yee, and M. P. Drake, Composite Mixed Conductor Membranes for Producing Oxygen, U. S. Patent 5,240,480. Date of Issue: August 31, 1993.
6) A. V. Virkar, K. Z. Fung, and C. W. Tanner, 'Electrode Design for Solid State Devices, Fuel cells, and Sensors', U. S. Patent 5,543,239. Date of issue: August 6, 1996.
7) C. W. Tanner,K-Z. Fung, and A. V. Virkar, *J. Electrochem. Soc*., **144** 21-30 (1997).
8) P. J. Gellings and H. J. M. Bouwmeester, '*Solid State Electrochemistry*', CRC Press, Boca Raton, FL (1997).
9) J. W. Stevenson, T. R. Armstrong, R. D. Carneim, L. R. Pederson and W. J. Weber, *J. Electrochem. Soc*., **143** [9] 2722-2729 (1996).
10) J. A. Lane, S. J. Benson, D. Waller, and J. A. Kilner, *Solid State Ionics*, **121** 201-208 (1999).
11) S. Wang, A. Verma, Y. L. Yang, A. J. Jacobson, and B. Abeles, *Solid State Ionics*, **140** 125-133 (2001).
12) W. Preis, E. Bucher and W. Sitte, *Journal of Power Sources*, **106** 116-121 (2002).
13) I. Yasuda and T. Hikita, *J. Electrochem. Soc*., **141** 1268 (1994).
14) J. Crank, '*The Mathematics of Diffusion*', Oxford University Press (1970).

LIST OF ACRONYMS AND ABBREVIATIONS

AC:	Alternating current
BET:	Brunauer-Emmett-Teller
DC:	Direct current
EMSL:	Environmental and Molecular Science Laboratory
LSC:	Sr-doped $LaCoO_3$
LSCF:	Sr-doped lanthanum colbatite-ferrite
LSF:	Sr-doped $LaFeO_3$
LSM:	Sr-doped $LaMnO_3$
MIEC:	Mixed ionic-electronic conducting or conductor or conduction
PNNL:	Pacific Northwest National Laboratory
SDC:	Samaria-doped CeO_2
SEM:	Scanning electron microscope
SOFC:	Solid oxide fuel cell
TPB:	Three-phase boundary
UU:	University of Utah
XRD:	X-ray diffraction
YSZ:	Yttria-stabilized zirconia

APPENDIX-I

ESTIMATION OF CHARGE TRANSFER RESISTIVITY OF $La_{0.8}Sr_{0.2}MnO_3$ (LSM) CATHODE ON $Y_{0.16}Zr_{0.84}O_2$ (YSZ) ELECTROLYTEUSING PATTERNED ELECTRODES

Rajesh Radhakrishnan[1], Anil V. Virkar[1*] and S. C. Singhal[2†]

(1) Department of Materials Science and Engineering, University of Utah

Salt Lake City, UT 84112

(2) Pacific Northwest National Laboratory

Richland, WA 99352

*Corresponding author - Address:

122 S Central Campus Dr. Room 304,

Salt Lake City, UT 84112

Ph: 801-581-5396

Fax: 801-581-4816

Email: anil.virkar@m.cc.utah.edu

[†]Fellow, The Electrochemical Society

ABSTRACT

YSZ Electrolyte discs with patterned LSM electrodes having different three phase boundary (TPB) lengths (l_{TPB}), but the same electrode-electrolyte interface area, were prepared using photomicrolithography. Impedance spectra for half-cells were obtained under oxygen partial pressures, (p_{O_2}), ranging from 10^{-3} to 1 atm and temperatures from 650 to 800°C. Area specific charge transfer resistance, R_{ct}, was found to vary inversely with l_{TPB}. While the charge transfer resistance is inversely proportional to l_{TPB}, consistent with the charge transfer reaction occurring mainly at the TPB, at 800°C some transport through LSM also appears to occur. The estimated value of charge transfer resistivity, ρ_{ct}, corresponding to the charge transfer reaction occurring at TPB, in air at 800°C (1.26 x 10^5 Ω-cm) is in good agreement with that estimated from actual fuel cell tests using quantitative stereological analysis of LSM-YSZ composite electrodes. R_{ct} and ρ_{ct} were found to decrease with increasing p_{O_2} and with increasing temperature. The activation energy for the overall charge transfer reaction was estimated to be ~1.5 eV.

Key words: Patterned electrode, Charge transfer resistance, Three phase boundary, Impedance spectroscopy, Oxygen reduction reaction

I. INTRODUCTION

Sr-doped $LaMnO_3$ (LSM), is the most commonly used cathode material for solid oxide fuel cells with Y_2O_3-stabilized ZrO_2 (YSZ) as the electrolyte because of its high thermal and chemical stability and excellent compatibility with YSZ [1, 2]. Many studies have been conducted to investigate the cathode reaction mechanism and to assess the performance of LSM electrodes [3, 4]. It is generally assumed that with LSM as the cathode and YSZ as the electrolyte, the electrochemical reaction of oxygen reduction given by

$$O_2(g) + 4e' = 2O^{2-} \quad (1)$$

occurs at the three phase boundary (TPB) between LSM, YSZ, and the gas phase. The corresponding geometric parameter, which governs the overall reaction kinetics, is the length of the TPB per unit area of the cathode-electrolyte macroscopic interface, given by l_{TPB} in units of cm^{-1}.

Various studies have been reported, wherein attempts were made to elucidate the exact relation between the length of three-phase boundary (TPB) and the charge transfer resistance [5-7]. In real electrodes which may consist of porous composite mixtures of LSM and YSZ, or other materials for example, the length of TPB can not be directly determined, albeit can be estimated using techniques in quantitative stereology. This in fact has been done in a limited number of studies [8]. From an experimental standpoint, however, a direct approach would be to deposit the electrode material, e.g. LSM, in a specific geometric pattern over an electrolyte disc, e.g. YSZ, and measure the polarization resistance using techniques such as impedance spectroscopy. Such an approach has been used recently to study the reaction mechanism of Ni anode [9, 10].

Horita et al. [11, 12], used cells with patterned LSM electrode and conducted SIMS analysis of oxygen isotope diffusion under the influence of externally applied potential to image the charge transfer regions and concluded that the most active site for charge transfer reaction is the TPB region. On the other hand, Brichzin et al. [13] used circular micro electrodes of LSM of varying area to study the dependence of cathodic polarization on the geometry and concluded that the polarization resistance varies with the inverse of the square of the microelectrode diameter, suggesting that the oxygen reduction reaction takes place at the surface of LSM.

In addition, there is no unanimity on the exact details of the cathodic reaction process though it is generally believed that the reaction steps include adsorption of oxygen, dissociation of molecular species into atomic species, migration of molecular or atomic species to TPB region, the occurrence of electron transfer reaction and the transfer of ions across the TPB region into the solid electrolyte. Often for simplicity it is assumed that one of the above is the rate-limiting step. Several rate-limiting steps in the charge transfer mechanism have been reported. For example, the dependence of the polarization resistance on p_{O_2} has been found to be of the form $p_{O_2}^{-n}$, with n varying between 0 and 1 [14-18]. Van Heuveln and Bouwmeester [19] reported that the diffusion of O^- species ng the LSM surface to the TPB area competes with charge transfer at low overpotential. Ostergard et al. [20] proposed three rate limiting steps, corresponding to three depressed semicircles observed in the impedance plots, which include dissociative adsorption of oxygen, diffusion of oxygen ions to the interface and transfer of oxygen ions from interface to the oxygen ion vacancies inside the electrolyte. Seibert et al. [15]

suggested that the rate-determining step may be dissociative adsorption of oxygen. The reported literature thus shows that while the p_{O_2} dependence of the charge transfer resistance is reasonable, the details of the overall reaction mechanisms are not well understood.

The present work was undertaken to investigate charge transfer characteristics at the LSM/YSZ/gas phase TPB using patterned electrodes and compare the results with those obtained using fuel cells with composite cathodes in which the ρ_{ct} was deduced from cell measurements and quantitative stereology [8]. Patterned LSM electrodes of well defined TPBs were sputter-deposited on sintered YSZ discs and impedance spectroscopy was used to obtain the polarization resistance to investigate the LSM-YSZ half cell reactions at temperatures between 650-800^{o}C and p_{O_2} between 10^{-3} to 1 atm. Limitations of impedance measurements on determining the exact reaction mechanism from these data are also discussed.

II. THEORY

Dependence of R_{ct} on the three phase boundary length (l_{TPB}):

In solid-state electrochemical devices, the charge transfer reaction given by equation (1) occurs at the TPB between the electrocatalyst (electrode), electrolyte, and the gas phase, provided the electrocatalyst is a predominantly electronic conductor. This is illustrated in Figure 1. The geometric parameter of importance is the TPB line length, l_{TPB}, given in units of length per unit area of the electrode/electrolyte macroscopic interface. The TPB line where charge-transfer occurs may be thought of as having a thickness, δ, and width,

ε. In terms of the charge transfer resistivity, $\rho_{ct}^{'}$, TPB line length, l_{TPB}, width, ε, and thickness, δ, through which charge transfer occurs, the area specific charge transfer resistance corresponding to the overall charge transfer reaction occurring at a TPB, R_{ct}^{TPB}, in units of Ωcm^2 is given by [21]

$$R_{ct}^{TPB} = \frac{\rho_{ct}^{'}\delta}{\varepsilon l_{TPB}} \tag{2}$$

The parameters δ and ε are expected to be on the order of a few angstroms, typical dimensions over which the actual charge transfer is anticipated to occur. The parameters $\rho_{ct}^{'}$, δ, and ε are not amenable to independent measurements. Thus one can define an intrinsic charge transfer resistivity, ρ_{ct}, by

$$\rho_{ct} = \frac{\rho_{ct}^{'}\delta}{\varepsilon} \tag{3}$$

and hence

$$R_{ct}^{TPB} = \frac{\rho_{ct}}{l_{TPB}} \tag{4}$$

wherein, in principle, R_{ct}^{TPB} and l_{TPB} can be separately measured, thus facilitating the estimation of ρ_{ct}. It is important to note that the R_{ct}^{TPB} as-defined includes the adsorption process, dissociation of molecular species into atomic species, migration of molecular or atomic species to TPB region, the occurrence of electron transfer reaction and the transfer of ions across the TPB region. Hence, ρ_{ct} depends upon a number of parameters such as the oxygen partial pressure, temperature, electronic and ionic conductivities of the electrode and electrolyte etc. However, it is microstructure-independent, and thus can be used as a figure of merit to compare two electrode materials. For a given set of conditions

of temperature and atmosphere, if the electrochemical reaction occurs at a TPB, it is expected that the dependence of R_{ct}^{TPB} on l_{TPB} will be given by equation (4).

For the electrodes investigated in this study, the three-phase boundary length is attributed to three factors: (1) the TPB length of the particular geometric pattern prepared by photolithography (l_{TPBp}), assuming straight line edges, (2) additional TPB length due to the possible waviness (α) of the edge at a microscopic level, and (3) the three phase boundary that occurs in the electrode film due to the inherent porosity of the substrate (electrolyte) and also due to the defects that occur during the preparation of the sputtered film (l_{TPB0}). Hence

$$l_{TPB} = l_{TPBp}(1+\alpha) + l_{TPB0} \tag{5}$$

It is not possible to measure or estimate α precisely. However since even microscopically the edges appear to be linear, the waviness factor α, may be close to zero and hence will be omitted in this analysis. The l_{TPBp}, was varied over a wide range to study the effect of three phase boundary length on area specific charge transfer resistance. The l_{TPB0} is more or less constant in all samples, since the electrode-electrolyte interface area was maintained constant in all samples. The two charge transfer paths, l_{TPBp} and l_{TPB0}, are parallel and hence the equation for the area specific charge transfer resistance corresponding to the overall charge transfer reaction occurring at a TPB can be written as

$$\frac{1}{R_{ct}^{TPB}} = \frac{1}{R_{ct_1}} + \frac{1}{R_{ct_2}} = \frac{l_{TPBp}}{\rho_{ct}} + \frac{l_{TPB0}}{\rho_{ct}} \tag{6}$$

where R_{ct_1} and R_{ct_2} are the area specific charge transfer resistance corresponding to the overall charge transfer reaction occurring at a TPB prepared by photolithography and that due to the defects in the film respectively.

Finally, if there is some transport of oxygen through the dense part of LSM, such as would occur if LSM exhibits some oxygen ion conduction in addition to its predominantly electronic conduction (that is, mixed ionic-electronic conduction, MIEC), there is a third parallel path, the inclusion of which gives

$$\frac{1}{R_{ct}} = \frac{1}{R_{ct}^{TPB}} + \frac{1}{R_{ct}^{MIEC}} = \frac{l_{TPBp}}{\rho_{ct}} + \frac{l_{TPB0}}{\rho_{ct}} + \frac{A_A}{R_{ct}^{MIEC}} \tag{7}$$

where, R_{ct} is the total area specific charge transfer resistance, A_A is the area fraction of the LSM electrode (microscopic electrode-electrolyte contact area), R_{ct}^{MIEC} is the area specific charge transfer resistance associated with the through transport of oxygen, which scales with inverse LSM/YSZ area, such as observed in the work of Brichzin et al. [13]. Since the LSM/YSZ area is same for all the samples in this study, effect of R_{ct}^{MIEC} should be same for all samples. It is important to emphasize that R_{ct}^{MIEC} also depends upon the thickness of the LSM layer. In the present work the thickness of LSM was essentially the same in all samples. Thus this aspect is not explicitly included in the analysis.

Dependence of R_{ct} and ρ_{ct} *on oxygen partial pressure* (p_{O_2})

Partial pressure dependence of the intrinsic charge transfer resistivity at a TPB may be given as

$$\rho_{ct} = \frac{\rho_{ct}^{''}}{\theta} \tag{8}$$

where θ is the surface coverage of oxygen and $\rho_{ct}^{''}$ is the charge transfer resistivity at $\theta = 1$. Substituting equation (8) in (4), R_{ct}^{TPB} may be given by

$$R_{ct}^{TPB} = \frac{\rho_{ct}^{''}}{\theta l_{TPB}} \tag{9}$$

Charge transfer on the entire surface of LSM, due to any possible mixed conduction, is similarly expected to depend upon surface oxygen coverage, and may be given by

$$R_{ct}^{MIEC} = \frac{R_{ct}^{MIEC(0)}}{\theta A_A} \tag{10}$$

where $R_{ct}^{MIEC(0)}$ is the area specific charge transfer resistance for the overall charge transfer process through LSM at surface coverage $\theta = 1$. In the preceding, it is assumed that surface coverage, θ, for a given oxygen partial pressure is the same at a TPB (which is strictly a line coverage) as well as on the surface of LSM, although in general, the two θs could be different. Since oxygen can adsorb as either molecular (associative) or atomic (dissociative) oxygen, it is important to consider both associative and dissociative adsorption. According to the Langmuir adsorption [22] model, surface coverage for associative absorption, θ_{O_2} is given by

$$\theta_{O_2} = \frac{b' p_{O_2}}{1 + b' p_{O_2} + b'' p_{N_2}} \tag{11}$$

Substituting equation (11) in (9) gives

$$R_{ct}^{TPB} = \frac{\rho_{ct}^{''}(1 + b' p_{O_2} + b'' p_{N_2})}{l_{TPB} b' p_{O_2}} \tag{12}$$

The partial pressure of oxygen was varied in this study by using mixtures of oxygen and nitrogen, while keeping the total pressure at 1 atm., i.e.,

$$p_{O_2} + p_{N_2} = 1 \tag{13}$$

Thus equation (12) can be written as

$$R_{ct}^{TPB} = \frac{\rho_{ct}^{''}\{(1+b'')+(b'-b'')p_{O_2}\}}{l_{TPB}b'p_{O_2}} \tag{14}$$

Similarly,

$$R_{ct}^{MIEC} = \frac{R_{ct}^{MIEC(0)}\{(1+b'')+(b'-b'')p_{O_2}\}}{A_A b'p_{O_2}} \tag{15}$$

Considering the two parallel paths contributing to the l_{TPB} and transport through LSM

$$\frac{1}{R_{ct}} = \frac{1}{R_{ct}^{TPB}} + \frac{1}{R_{ct}^{MIEC}} = \frac{1}{R_{ct_1}} + \frac{1}{R_{ct_2}} + \frac{1}{R_{ct}^{MIEC}} = \frac{\theta_{O_2} l_{TPBp}}{\rho_{ct}^{''}} + \frac{\theta_{O_2} l_{TPB0}}{\rho_{ct}^{''}} + \frac{\theta_{O_2} A_A}{R_{ct}^{MIEC(0)}} \tag{16}$$

or

$$\frac{1}{R_{ct}} = \frac{l_{TPBp}}{\rho_{ct}^{''}} \frac{b'p_{O_2}}{\{(1+b'')+(b'-b'')p_{O_2}\}} + \frac{l_{TPB0}}{\rho_{ct}^{''}} \frac{b'p_{O_2}}{\{(1+b'')+(b'-b'')p_{O_2}\}} + \frac{A_A}{R_{ct}^{MIEC(0)}} \frac{b'p_{O_2}}{\{(1+b'')+(b'-b'')p_{O_2}\}} \tag{17}$$

Thus a plot of $1/R_{ct}$ vs. l_{TPBp} should be linear with slope = $\frac{1}{\rho_{ct}^{''}} \frac{b'p_{O_2}}{\{(1+b'')+(b'-b'')p_{O_2}\}}$ and intercept = $\frac{l_{TPB0}}{\rho_{ct}^{''}} \frac{b'p_{O_2}}{\{(1+b'')+(b'-b'')p_{O_2}\}} + \frac{A_A}{R_{ct}^{MIEC(0)}} \frac{b'p_{O_2}}{\{(1+b'')+(b'-b'')p_{O_2}\}}$. The ratio of intercept to slope should give $l_{TPB0} + \frac{\rho_{ct}^{''}A_A}{R_{ct}^{MIEC(0)}}$. Also from equation (4), 1/slope of the plot of $1/R_{ct}$ vs. l_{TPBp} is the charge transfer resistivity, ρ_{ct}, which is given by

$$\rho_{ct} = \frac{\rho_{ct}^{''}(1+b'')}{b'p_{O_2}} + \frac{\rho_{ct}^{''}(b'-b'')}{b'} \tag{18}$$

Note that a plot of ρ_{ct} vs. $\frac{1}{p_{O_2}}$ should be linear with slope = $\frac{\rho_{ct}^{''}(1+b'')}{b'}$ and intercept = $\frac{\rho_{ct}^{''}(b'-b'')}{b'}$. Multiplying both sides of equation (18) by p_{O_2}

$$\rho_{ct} p_{O_2} = \frac{\rho_{ct}^{"}(1+b")}{b'} + \frac{\rho_{ct}^{"}(b'-b")p_{O_2}}{b'} \tag{19}$$

Thus plot of $\rho_{ct} p_{O_2}$ vs. p_{O_2} should be linear with slope = $\frac{\rho_{ct}^{"}(b'-b")}{b'}$ and intercept = $\frac{\rho_{ct}^{"}(1+b")}{b'}$.

If the adsorption of nitrogen is negligible, $b" = 0$, and equation (18) becomes

$$\rho_{ct} = \frac{\rho_{ct}^{"}}{b' p_{O_2}} + \rho_{ct}^{"} \tag{20}$$

and equation (19) becomes

$$\rho_{ct} p_{O_2} = \frac{\rho_{ct}^{"}}{b'} + \rho_{ct}^{"} p_{O_2} \tag{21}$$

Thus a plot of ρ_{ct} vs. $\frac{1}{p_{O_2}}$ should be linear with slope = $\frac{\rho_{ct}^{"}}{b'}$ and intercept = $\rho_{ct}^{"}$ and that of $\rho_{ct} p_{O_2}$ vs. p_{O_2} should be linear with slope = $\rho_{ct}^{"}$ and intercept = $\frac{\rho_{ct}^{"}}{b'}$. That is, $\rho_{ct}^{"}$ and b' can be estimated from both of these plots provided adsorption of nitrogen is negligible and should give same values, if the p_{O_2} dependence of ρ_{ct} obeys the associative adsorption model.

If oxygen adsorbs as atomic oxygen, the surface coverage, θ_O is given by

$$\theta_O = \frac{b^* \sqrt{p_{O_2}}}{1 + b^* \sqrt{p_{O_2}} + b^{**} \sqrt{p_{N_2}}} \tag{22}$$

Using equation (22) in (9)

$$R_{ct}^{TPB} = \frac{\rho_{ct}^{''}(1 + b^{*}\sqrt{p_{O_2}} + b^{**}\sqrt{p_{N_2}})}{l_{TPB} b^{*}\sqrt{p_{O_2}}} \tag{23}$$

In this case to further simplify the equation it is necessary to ignore the adsorption of nitrogen. Thus, setting $b^{**} = 0$ gives

$$R_{ct}^{TPB} = \frac{\rho_{ct}^{''}(1 + b^{*}\sqrt{p_{O_2}})}{l_{TPB} b^{*}\sqrt{p_{O_2}}} \tag{24}$$

Similarly

$$R_{ct}^{MIEC} = \frac{R_{ct}^{MIEC(0)}(1 + b^{*}\sqrt{p_{O_2}})}{A_A b^{*}\sqrt{p_{O_2}}} \tag{25}$$

Considering the two parallel paths that contribute to l_{TPB} and transport through LSM,

$$\frac{1}{R_{ct}} = \frac{1}{R_{ct}^{TPB}} + \frac{1}{R_{ct}^{MIEC}} = \frac{1}{R_{ct_1}} + \frac{1}{R_{ct_2}} + \frac{1}{R_{ct}^{MIEC}} = \frac{\theta_O l_{TPBp}}{\rho_{ct}^{''}} + \frac{\theta_O l_{TPB0}}{\rho_{ct}^{''}} + \frac{\theta_O A_A}{R_{ct}^{MIEC(0)}} \tag{26}$$

or

$$\frac{1}{R_{ct}} = \frac{b^{*}\sqrt{p_{O_2}} l_{TPBp}}{(1 + b^{*}\sqrt{p_{O_2}})\rho_{ct}^{''}} + \frac{b^{*}\sqrt{p_{O_2}} l_{TPB0}}{(1 + b^{*}\sqrt{p_{O_2}})\rho_{ct}^{''}} + \frac{b^{*}\sqrt{p_{O_2}} A_A}{(1 + b^{*}\sqrt{p_{O_2}})R_{ct}^{MIEC(0)}} \tag{27}$$

A plot of $1/R_{ct}$ vs. l_{TPBp} should be linear with slope = $\frac{b^{*}\sqrt{p_{O_2}}}{(1 + b^{*}\sqrt{p_{O_2}})\rho_{ct}^{''}}$ and intercept = $\frac{b^{*}\sqrt{p_{O_2}} l_{TPB0}}{(1 + b^{*}\sqrt{p_{O_2}})\rho_{ct}^{''}} + \frac{b^{*}\sqrt{p_{O_2}} A_A}{(1 + b^{*}\sqrt{p_{O_2}})R_{ct}^{MIEC(0)}}$ and the ratio of intercept to slope = $l_{TPB0} + \frac{\rho_{ct}^{''} A_A}{R_{ct}^{MIEC(0)}}$. Again, 1/slope of the plot of $1/R_{ct}$ vs. l_{TPBp} is the charge transfer resistivity, ρ_{ct}, given by

$$\rho_{ct} = \frac{\rho_{ct}^{''}}{b^{*}\sqrt{p_{O_2}}} + \rho_{ct}^{''} \qquad (28)$$

A plot of ρ_{ct} vs. $\frac{1}{\sqrt{p_{O_2}}}$ should be linear with slope = $\frac{\rho_{ct}^{''}}{b^{*}}$ and intercept = $\rho_{ct}^{''}$.

Multiplying both sides of equation (28) by $\sqrt{p_{O_2}}$ gives

$$\rho_{ct}\sqrt{p_{O_2}} = \frac{\rho_{ct}^{''}}{b^{*}} + \rho_{ct}^{''}\sqrt{p_{O_2}} \qquad (29)$$

A plot of $\rho_{ct}\sqrt{p_{O_2}}$ vs. $\sqrt{p_{O_2}}$ should also be linear with slope = $\rho_{ct}^{''}$ and intercept = $\frac{\rho_{ct}^{''}}{b^{*}}$.

The above two plots should give same values of $\rho_{ct}^{''}$ and b^{*}, if the p_{O_2} dependence of ρ_{ct} obeys the dissociative adsorption model.

III. EXPERIMENTAL

Discs of YSZ (Tosoh Corporation, Japan) were fabricated using conventional ceramic processing methods involving die-pressing of powder compacts followed by sintering in air. The powder was pressed in a circular die using a uni-axial press at a pressure of 4,500 Kg. The discs obtained were then sintered at 1500^{o}C for 5 hours in air. The discs r sintering had dimensions of approximately 24 mm in diameter and 3.5 mm in thickness. One surface of each disc was polished to a 1 micron finish. After polishing, a groove was machined along the cylindrical surface of the disc at a distance of nearly 1.5 mm from the polished surface. The discs were then cleaned in soap solution followed by rinsing in acetone, in de-ionized water and dried at 500^{o}C for 2 hours.

Patterned (mesh patterns with electrode-electrolyte contact area fraction A_A = 0.75) LSM electrodes corresponding to a wide range of l_{TPBp} were fabricated on the polished surfaces, in a circular area of 1 cm diameter (area = 0.785 cm^2) at the center of the each disc, using microphotolithography and sputtering techniques. In order to obtain the mesh pattern of the electrode, the disc was initially coated with positive photoresist Shipley 1818 and was baked at 100^oC for 5 minutes. The sample was then exposed to UV light for 20 seconds using previously prepared dark field mask with appropriate mesh pattern. The exposed sample was developed using MF 321 developer for nearly 30 seconds, rinsed in DI water and dried. Several samples were patterned using different masks, each having the same A_A but different l_{TPBp}. The patterned samples were then loaded into a sputtering chamber. The LSM electrodes of nearly 0.5 μm thickness were sputter deposited from a $La_{0.8}Sr_{0.2}MnO_3$ target by RF sputtering using argon plasma. The YSZ discs were held at a distance of 15 cm from the target and were at room temperature during sputtering. The chamber pressure was kept at a minimum (1 mTorr) to obtain a dense thin film of LSM. The deposition was conducted for 90 minutes at a rate of 5 nm per minute. After sputtering the discs were washed in acetone to lift off the photoresist and LSM film on top of the resist, giving rise to the LSM film in the desired mesh pattern. The discs with patterned electrodes were later annealed at 1000^oC for 2 hours. X-ray diffraction (XRD) patterns of the as-sputtered and annealed LSM films were obtained. The electrode morphology was analyzed before and after annealing and after electrochemical testing by optical profilometer and scanning electron microscope (SEM).

A counter electrode of platinum was applied using platinum resinate, again in a circular area of 1 cm diameter at the center of the opposite face of the disc so that it is symmetric with respect to the patterned LSM working electrode. The discs were again annealed at 900^{o}C for 2 hours to remove the organic components of the platinum resinate and to obtain a well bonded porous platinum counter electrode. A platinum reference electrode in the form of a ring was positioned along the groove on the cylindrical surface of the disc.

Platinum mesh was used as current collector on both working and counter electrode. The cell was assembled between two alumina rings with the help of two honeycomb discs of alumina, two threaded rods, springs and wing nuts. Care was taken to ensure that both the electrodes were completely exposed to the external atmosphere, while firmly holding the current collector mesh on to the electrodes. Electrical connections were made by connecting platinum wires to the platinum mesh. The assembled cell was then placed inside an alumina tube such that the cell was near the closed end of the tube, the working electrode always facing the closed end of the tube. The tube was tightly sealed using a rubber cork. Holes were drilled in the cork through which the platinum leads for electrical connection and the rods to hold the cell were inserted. A gas inlet tube and a gas outlet tube were also inserted into the rubber cork. The inlet tube was long enough to ensure release of the gas very close to the working electrode of the cell. The alumina tube containing the cell assembly was then placed in a horizontal tube furnace such that the cell was positioned near the center of the furnace. The tip of a thermocouple was placed very near the cell to measure the temperature. The inlet tube was connected to

compressed gas cylinders with premixed gas compositions. A flow rate of nearly 200 ml/minute was used to continuously circulate the respective premixed gas of a given oxygen partial pressure. When changing the temperature or pressure, the system was allowed to equilibrate at the new conditions for two hours before taking any measurements. Impedance spectra were obtained using Solartron Impedance/gain-phase analyzer (SI-1260) in combination with Solartron Electrochemical Interface (SI-1287), over a range of temperatures between 650 and 800^{o}C in gas mixtures with oxygen partial pressure ranging from 10^{-3} to 1 atm.

IV. RESULTS AND DISCUSSION

Phase and Morphology of the LSM electrode:

XRD pattern of the as-sputtered electrode was that of an amorphous phase and did not exhibit evidence of a crystalline phase. The XRD pattern (Figure 2) of the same film after annealing at 1000^{o}C clearly showed LSM-type orthorhombic perovskite phase. Peaks from the YSZ substrate can also be seen in the XRD pattern. An SEM image of the sample with $l_{TPBp} = 430$ cm^{-1} after annealing is given in Figure 3 which clearly shows the well defined mesh pattern of the electrode. The image shows that the electrode edges are smooth and continuous. Optical profiles indicated that edges are essentially vertical and sharp. This allows precise determination of the l_{TPBp}. The l_{TPBp} was varied from sample to sample by varying the width of the mesh and the openings, while keeping A_A constant. The calculated l_{TPBp} for various patterns were 1200, 800, 430, 250, and 50 cm^{-1}. The pores in the film due to those in the substrate can also be seen in the SEM micrograph shown in Figure 3. Since A_A in all samples was kept constant, the contribution to l_{TPB}

due to these pores in the prepared film, namely l_{TPB0}, should be more or less the same in all samples. The l_{TPB0} was estimated using quantitative stereology [23]. For this all the tested samples were examined under SEM and nearly 5 micrographs were obtained randomly on the patterned electrode area of each sample. Horizontal and vertical test lines were drawn on the images along the LSM area and the point intercepts per unit length (p_L) where the pores in the film intercept the test line were determined. The length of the perimeter of the pores in the film per unit area (L_A) was estimated using the equation $L_A = \frac{\pi}{2} p_L$ [23]. The average value of L_A was found to be 334 ± 23 cm^{-1}. The area fraction of LSM in the patterned electrode, A_A, is 0.75. Therefore, we have $l_{TPB0} = A_A \times L_A = 0.75 \times 334 = 250$ cm^{-1}. The SEM patterns of the electrodes appeared more or less unchanged after electrochemical testing.

Impedance Analysis:

The impedance spectra of patterned LSM electrodes on YSZ at various temperatures and in oxygen partial pressures for samples of different TPB length are given in Figures 4 through 6. The impedance spectra typically consisted of suppressed single arcs. The high frequency intercept of the arc with the real axis (R_1) corresponds to the ohmic resistance and the low frequency intercept (R_2) corresponds to the total resistance of the half cell. In Figures 4 and 5, which correspond to measurements at 800^{o}C the ohmic part (R_1) does not change. R_1 for all samples with different l_{TPBp} (Figure 4) is expected to be the same, since it is mainly due to the resistance of the YSZ disc between the working and the reference electrodes. R_1 does not change with change in p_{O_2} (Figure 5), since over this

partial pressure range the resistance of YSZ is essentially constant. In Figure 6, in which measurements are given for temperatures ranging from 650°C and 800°C, it can be seen that R_1 (inset) decreases with increasing temperature due to the temperature dependence of the YSZ resistance. Polarization resistance of the electrode was obtained by subtracting R_1 from R_2. From the impedance spectra (Figures 4 through 6) it is seen that the polarization resistance depends on l_{TPB}, oxygen partial pressure, and temperature. The R_{ct} was calculated by multiplying the polarization resistance with the total electrode area (0.785 cm^2).

Dependence of R_{ct} on the three phase boundary length (l_{TPB})

Figure 7 shows plots of $1/R_{ct}$ vs. l_{TPBp} at 800°C in atmospheres with different p_{O_2} and Figure 8 shows similar plots in air at different temperatures. It is seen that the R_{ct} varies inversely with l_{TPBp}, consistent with equation (7). The inverse of the slope gives the charge transfer resistivity, ρ_{ct}. The estimated values of ρ_{ct}, at different temperatures and p_{O_2}, are summarized in Table 1. It can be seen that a value of zero for l_{TPBp} gives a finite R_{ct} value, i.e., a finite y-intercept. Similar non-zero intercept for $1/R_{ct}$ has been reported for microfabricated Ni anode [9, 10]. According to equation (7) this intercept is given by $\frac{l_{TPB0}}{\rho_{ct}} + \frac{A_A}{R_{ct}^{MIEC}}$. The ratio of the y-intercept to slope of these plots (or the magnitude of the intercept on negative x-axis) gives $l_{TPB0} + \frac{\rho_{ct} A_A}{R_{ct}^{MIEC}}$. As discussed above in the theory, this ratio is also equal to $l_{TPB0} + \frac{\rho_{ct}^{"} A_A}{R_{ct}^{MIEC(0)}}$, since same surface coverage and

adsorption model is assumed. This value was found to be close to 400 cm^{-1} from Figure 7. The l_{TPB0} determined by quantitative stereology is 250 cm^{-1}. This confirms that charge transfer through l_{TPB0}, due to the pores in the electrode area (which in turn is created due to the pores in the substrate and also due to the unintentional defects that occur in the sputter deposited LSM film), is significant. Thus, while varying the l_{TPBp} from 50 to 1200 (24 fold), the l_{TPB}, actually varied from 300 to 1450 (4.83 fold). Hence if the charge transfer reaction were to take place only at the TPB, it is expected that R_{ct} should also vary by a factor of 4.83 for the range of l_{TPBp} studied. It was found that R_{ct} varied 6 fold at 650°C while it varied 3.5 fold at 800°C. It is also interesting to note that while, $l_{TPB0} + \frac{\rho_{ct}^{"} A_A}{R_{ct}^{MIEC(0)}}$ determined from the ratio of the intercept to slope of the $1/R_{ct}$ vs. l_{TPBp} plot exhibits no systematic variation with p_{O_2} (Figure 9a), it decreases systematically with decrease in temperature (Figure 9b). This is reasonable since both $\rho_{ct}^{"}$ and $R_{ct}^{MIEC(0)}$ are independent of oxygen partial pressure (correspond to surface coverage $\theta = 1$), but are functions of temperature. Since $\rho_{ct}^{"}$ and $R_{ct}^{MIEC(0)}$ correspond to thermally activated processes with Arrhenius type temperature dependence, both should increase with decreasing temperature. It can be seen from Figure 9b that $l_{TPB0} + \frac{\rho_{ct}^{"} A_A}{R_{ct}^{MIEC(0)}}$ decreases with decreasing temperature, indicating that $\frac{\rho_{ct}^{"} A_A}{R_{ct}^{MIEC(0)}}$ decreases with decreasing temperature. Since the temperature dependence of $l_{TPB0} + \frac{\rho_{ct}^{"} A_A}{R_{ct}^{MIEC(0)}}$ is only due to that of $\frac{\rho_{ct}^{"} A_A}{R_{ct}^{MIEC(0)}}$, this is possible if the activation energy for $R_{ct}^{MIEC(0)}$ is higher than that of $\rho_{ct}^{"}$. The oxygen

reduction reaction at the surface of LSM and subsequent transport of oxygen ions through LSM is governed by the oxygen chemical surface exchange coefficient (k_{chem}) and oxygen chemical diffusion coefficient (D_{chem}) of LSM [24, 25]. Owing to the very low D_{chem} of LSM, for an electrode of nearly 0.5 μm thickness, $R_{ct}^{MIEC(0)}$ should essentially be determined by D_{chem}, with the activation energy ranging between 2 to 3 eV [26, 27]. This is higher than the activation energy for $\rho_{ct}^{"}$ (1.5 eV) determined in this work. Since same partial pressure dependence is assumed for both ρ_{ct} and R_{ct}^{MIEC}, $\frac{\rho_{ct}A_A}{R_{ct}^{MIEC}} = \frac{\rho_{ct}^{"}A_A}{R_{ct}^{MIEC(0)}}$ and $l_{TPB0} + \frac{\rho_{ct}A_A}{R_{ct}^{MIEC}} = l_{TPB0} + \frac{\rho_{ct}^{"}A_A}{R_{ct}^{MIEC(0)}}$. This allows for the estimation of the value of R_{ct}^{MIEC} at a given temperature and pressure, knowing l_{TPB0} determined from quantitative stereology and $l_{TPB0} + \frac{\rho_{ct}A_A}{R_{ct}^{MIEC}}$, and ρ_{ct} determined from the $1/R_{ct}$ vs. l_{TPBp} plot. Because of the possible errors involved in the determination l_{TPB0} and $l_{TPB0} + \frac{\rho_{ct}A_A}{R_{ct}^{MIEC}}$, it is not possible to determine R_{ct}^{MIEC} at lower temperatures, but its value at 800°C in air is estimated to be 460 Ω-cm^2. Measured value of R_{ct} for a sample with l_{TPBp} = 1200 cm^{-1} is 80 Ω-cm^2. Knowing R_{ct} and R_{ct}^{MIEC}, R_{ct}^{TPB}, the charge transfer resistance associated with oxygen reduction reaction occurring at the TPB (TPB due to the mesh pattern and the pores and defects in the film) can be estimated using equation (7). The R_{ct}^{TPB} estimated for a sample with l_{TPBp} = 1200 cm^{-1} is 97 Ω-cm^2. Thus the value of R_{ct}^{MIEC} at 800°C in air is nearly 4.7 times that of R_{ct}^{TPB} for a sample with l_{TPBp} = 1200 cm^{-1}. This indicates that while the

charge transfer resistance is inversely proportional to l_{TPB}, consistent with the charge transfer reaction occurring mainly at the TPB, at higher temperatures some transport through LSM also appears to occur. But, while the oxygen reduction reaction at the surface of LSM and subsequent transport of oxygen ions through LSM is possible at 800^{o}C, its contribution to the overall charge transport reaction is much lower compared to that occurring at a TPB. This contribution reduces further at temperatures below 800^{o}C. In actual fuel cells consisting of composite electrodes of LSM and YSZ, the l_{TPB} is of the order 10^4 cm^{-1} [28] and hence, the contribution of the oxygen reduction reaction occurring at the surface of LSM to the overall charge transfer process is even lower.

The value of ρ_{ct} at 800^{o}C in air is 1.26 x 10^5 Ω-cm, which is in good agreement with that reported by Zhao [7] et al. from measurements on fuel cells with LSM + YSZ composite electrodes. In that report they used quantitative stereology to estimate the TPB length. Advantage of using patterned electrodes is that the l_{TPB} can be varied more systematically and can be determined more accurately than using composite electrodes. Also, using composite electrodes a direct measurement of activation polarization is difficult, since the measured resistance includes contribution from concentration polarization as well. The contribution from concentration polarization can be essentially neglected when using patterned thin film electrode, such as in the present studies

Dependence of R_{ct} and ρ_{ct} *on oxygen partial pressure* (p_{O_2})

Plots of ρ_{ct} vs. $\frac{1}{p_{O_2}}$ and $\rho_{ct} p_{O_2}$ vs. p_{O_2} (associative adsorption) and ρ_{ct} vs. $\frac{1}{\sqrt{p_{O_2}}}$ and $\rho_{ct}\sqrt{p_{O_2}}$ vs. $\sqrt{p_{O_2}}$ (dissociative adsorption) are given in Figures 10 and 11. It can be seen that in the two plots for associative adsorption (10a and 10b) and those for dissociative adsorption (11a, and 11b) the slope in one plot (a) is the intercept in the other (b) and vice-a-versa. The value of b' and b^* (Table 2) and ρ''_{ct} (Table 3) were estimated from the slope and intercept in the respective plots. These values estimated from Figures 10a and 10b corresponding to associative adsorption model do not agree very well with each other, but those estimated from Figures 11a and 11b corresponding to dissociative adsorption are in good agreement. This may indicate that the adsorption mechanism is dissociative, rather than associative. But it should also be noted that while using the associative adsorption model it is not necessary to assume that adsorption of nitrogen is negligible, though in that case it wouldn't be possible to estimate b' or ρ''_{ct}. Also, estimated values of both $b'$and b^*were found to be independent of temperature. It is known that the adsorption coefficient is a function of temperature, given by $b(T) = b_0 \exp(\frac{E_{ads}}{kT})$, ($b$ represents b' or b^*) where E_{ads} is negative. The invariance of the estimated value of b' or b^* with temperature suggests that the magnitude of E_{ads} must be rather small. It should also be noted that the impedance spectrum is not a direct measurement of the adsorption process, but is a measurement of the cumulative effects of the various steps involved in the overall charge transfer reaction. Hence, it is difficult to conclude the reaction mechanism from impedance spectra alone. In addition, the often used assumption that only one process among the many processes occurring in the multi-

step charge transfer process is away from equilibrium, may not be valid, making the determination of the exact mechanism even more difficult.

Effect of Temperature:

It was found that R_{ct} and ρ_{ct} increase exponentially with decrease in temperature. All samples with different TPB exhibited the same temperature dependence of R_{ct} on temperature. In Figure 12, $\ln(\rho_{ct})$ is plotted vs. inverse of absolute temperature for various p_{O_2}. From the slope of the plots, the activation energy (E_a) for the overall charge transfer process was estimated to be ~1.5 eV. It was also observed that the activation energy is nearly the same over the entire p_{O_2} range investigated. It was further found that the ρ''_{ct} estimated from associative or dissociative adsorption model also exhibits the same activation energy, although, the ρ''_{ct} determined assuming dissociative adsorption is deemed more reliable.

V. CONCLUSIONS

The present work shows a linear relation between $1/R_{ct}$ and l_{TPB} for LSM electrodes on YSZ, consistent with the occurrence of charge transfer predominantly at TPB. While the charge transfer resistance is inversely proportional to l_{TPB}, consistent with the charge transfer reaction occurring mainly at the TPB, at 800°C, some transport through LSM also appears to occur. However, even though oxygen reduction reaction at the surface of LSM and subsequent transport of oxygen ions through LSM is possible at 800°C, its

contribution to the overall charge transport reaction is much lower compared to that occurring at a TPB. In addition this contribution is even lower at temperatures below 800°C. The slope of the plots of $1/R_{ct}$ vs. l_{TPB}, gives the charge transfer resistivity, ρ_{ct}. The estimated value of ρ_{ct} is in good agreement with that measured for LSM in composite electrodes in actual fuel cells using quantitative stereology [8]. R_{ct} and hence ρ_{ct} decreases with increase in p_{O_2} and increase in temperature. When the adsorption of nitrogen is neglected, the variation of measured R_{ct} with p_{O_2} agrees better with the dissociative adsorption model rather than associative adsorption model. The adsorption coefficients were found to be independent of temperature. It is difficult to accurately predict a reaction mechanism from impedance spectra alone due to the fact that an impedance spectrum is a measurement of the cumulative effect of the various steps in the oxygen reduction reaction. The estimated activation energy for the charge transfer reaction is ~1.5 eV.

ACKNOWLEDGEMENTS

This work was supported by the United States Department of Energy (DOE) through its High Temperature Electrochemistry Center (HiTEC) at the Pacific Northwest National Laboratory (PNNL) and by the DOE contract (contract no.: DE-FC26-02NT41565) at the University of Utah. A portion of the research described in this paper was performed in the Environmental Molecular Sciences Laboratory, a national scientific user facility sponsored by the Department of Energy's Office of Biological and Environmental Research and located at the Pacific Northwest National Laboratory.

REFERENCES

1. Proceedings of the third international symposium on solid oxide fuel cells, S. C Singhal and H. Iwahara, Editors PV 93-4, The Electrochemical Society Proceeding Series, Pennington, NJ (1993).
2. N. Minh, J. Am. Cer. Soc., **76**, 563 (1993).
3. Y. Jiang, S. Wang, Y Zhang, J. Yan and W. Li, J. Electrochem. Soc., **145**, 373 (1998).
4. J. Van Herle, A. J. McEvoy and R. Thampi, Electrochim. Acta, **41** 1447 (1996)
5. H. Fukunaga, M. Ihara, K. Sakaki, and K. Yamada, Solid State Ionics, **86-88**, 1179 (1996)
6. J. Fleig, Journal of Power Sources, **105**, 228 (2002)
7. F. H van Heuveln, H. J. M. Bouwmeester and F.P.F.van Berkel, J. Electrochem. Soc., **144**, 126 (1997)
8. F. Zhao, Y. Jiang, G. Y. Lin and A.V. Virkar, Electrochemical Society Proceedings Volume 2001-16, 501 (2001)
9. J. Mizusaki, H. Tagawa, T. Saito, T. Yamamura, K. Kamitani, K. Hirano, S. Ehara, T. Takagi, T. Hikita, M. Ippommatsu, S. Nakagawa and K. Hashimoto, Solid State Ionics, **70/71**, 52 (1994).
10. A. Bieberle, L. P. Meier and L. J Gauckler, J. Electrochem. Soc., **148** A646 (2001)
11. T. Horita, K. Yamaji, N. Sakai, H. Yokokawa, T. Kawada, and T. Kato, Solid State Ionics, **127**, 55 (2000)

12. T. Horita, K. Yamaji, N. Sakai and H. Yokokawa, J. Electrochem. Soc., **148**, J25 (2001)
13. V. Brichzin, J Fleig, H.-U.Habermeier, and J. Maier, Electrochem. Solid State Lett., **3**, 403 (2000)
14. Y. Takeda, R. Kanno, M. Noda, Y. Tomido and O. Yamamoto, J. Electrochem. Soc., **134**, 2656 (1987)
15. E. Seibert, A. Hammouche and M Kleitz, Electrochim. Acta **40**, 1741 (1995)
16. J-D. Kim, G-D. Kim, J-W. Moon, Y. Park, W-H. Lee, K. Kobayashi, M. Nagai and C-E Kim, Solid State Ionics **143**, 379 (2001)
17. E. P. Murray, T. Tsai, and S. A. Barnett, Solid State Ionics, **110**, 235 (1998)
18. A. Endo, H. Fukunaga, C. Wen, and K. Yamada, Solid State Ionics, **135**, 353 (2000)
19. F. H van Heuveln and H. J. M. Bouwmeester, J. Electrochem. Soc.,**144**, 134 (1997)
20. M. J. L Ostergard and M. Mogensen, Electrochim. Acta, **38**, 2015 (1993)
21. C. W. Tanner, K-Z. Fung and A. V. Virkar, J. Electrochem. Soc., **144**, 21 (1997)
22. A. W. Adamson and A. P. Gast. Physical Chemistry of Surfaces, 6th Ed., Wiley, New York (1997)
23. E. Underwood, Quantitative Stereology, Addison Wesley Publishing Company, Inc. (1970).
24. J. Mizusaki, H. Tagawa, K. Tsuneyoshi and A. Sawata, J. Electrochem. Soc., **138**, 1867 (1991)
25. J. Fleig and J. Maier, J. Eu. Cer. Soc., **24**, 1343 (2004)

26. I. Yasuda, K. Ogasawara, M. Hishinuma, T. Kawada and M. Dokiya, Solid State Ionics, **86-88**, 1197 (1996)

27. L. Mikkelsen and E. Skou, J. Therm. Anal. Cal., **64**, 873 (2001)

28. E. Ivers' Tiffee and A. V. Virkar, in High Temperature Solid Oxide Fuel Cells: Fundamentals Design and Application, S. C. Singhal and K. Kendall, Editors, Elsevier Ltd. (2003)

TABLES

Table 1: Values of ρ_{ct} (Ω-cm) estimated from $1/R_{ct}$ vs. l_{TPBp} plots at different temperature and oxygen partial pressure

Temp \ p_{O2}	1 atm	0.21 atm	0.1 atm	0.05 atm	0.01 atm
800°C	88000	126000	143000	176000	293000
750°C	206000	261000	310000	386000	676000
700°C	474000	613000	746000	935000	1540000
650°C	1190000	1520000	1850000	2330000	4170000

Table 2: Estimated values of adsorption coefficient from Figures 10 and 11.

	Estimated from	800°C	750°C	700°C	650°C
Associative b'	Figure 10a	60.77	58.74	65.70	61.60
	Figure 10b	20.42	20.42	22.61	16.6
Dissociative b^*	Figure 11a	3.10	3.40	2.94	3.07
	Figure 11b	2.59	3.18	3.00	2.97

Table 3: Estimated values ρ''_{ct} (Ω-cm) from Figures 10 and 11.

	Estimated from	800°C	750°C	700°C	650°C
Associative	Figure 10a	113000	245000	592000	1470000
	Figure 10b	83000	197000	452000	1140000
Dissociative	Figure 11a	69000	149000	377000	913000
	Figure 11b	64000	154000	353000	886000

FIGURE CAPTIONS

Figure 1: Model for charge transfer at a three phase boundary (TPB).

Figure 2: An XRD pattern of sputtered LSM film after annealing at 1000°C for 2 hours.

Figure 3: An SEM image of LSM patterned electrode on YSZ with $l_{TPBp} = 430$ cm^{-1}.

Figure 4: Impedance Spectra of cells with different l_{TPBp} in air at 800°C.

Figure 5: Impedance Spectra of a cell with $l_{TPBp} = 1200$ cm^{-1} at 800°C for different p_{O_2}.

Figure 6: Impedance Spectra of a cell with $l_{TPBp} = 1200$ cm^{-1} in air at different temperatures. The inset shows enlarged region of the high frequency intercepts at various temperatures.

Figure 7: Plots of $1/R_{ct}$ vs. l_{TPBp} at 800°C at different p_{O_2}.

Figure 8: Plots of $1/R_{ct}$ vs. l_{TPBp} in air at different temperatures.

Figure 9(a): Plots of $l_{TPB0} + \frac{\rho_{ct}^{"} A_A}{R_{ct}^{MIEC(0)}}$ vs. oxygen partial pressure at several temperatures.

Figure 9(b): Plots of $l_{TPB0} + \frac{\rho_{ct}^{"} A_A}{R_{ct}^{MIEC(0)}}$ vs. temperature at several oxygen partial pressures.

Figure 10(a): Plots of ρ_{ct} vs. $1/p_{O_2}$ at different temperatures (associative adsorption model).

Figure 10(b): Plots of $\rho_{ct} p_{O_2}$ vs. p_{O_2} at different temperatures (associative adsorption model).

Figure 11(a): Plots of ρ_{ct} vs. $1/\sqrt{p_{O_2}}$ at different temperatures (dissociative adsorption model).

Figure 11(b): Plots of $\rho_{ct}\sqrt{p_{O_2}}$ vs. $\sqrt{p_{O_2}}$ at different temperatures (dissociative adsorption model).

Figure 12: Arrhenius plots of ρ_{ct} at different oxygen partial pressures.

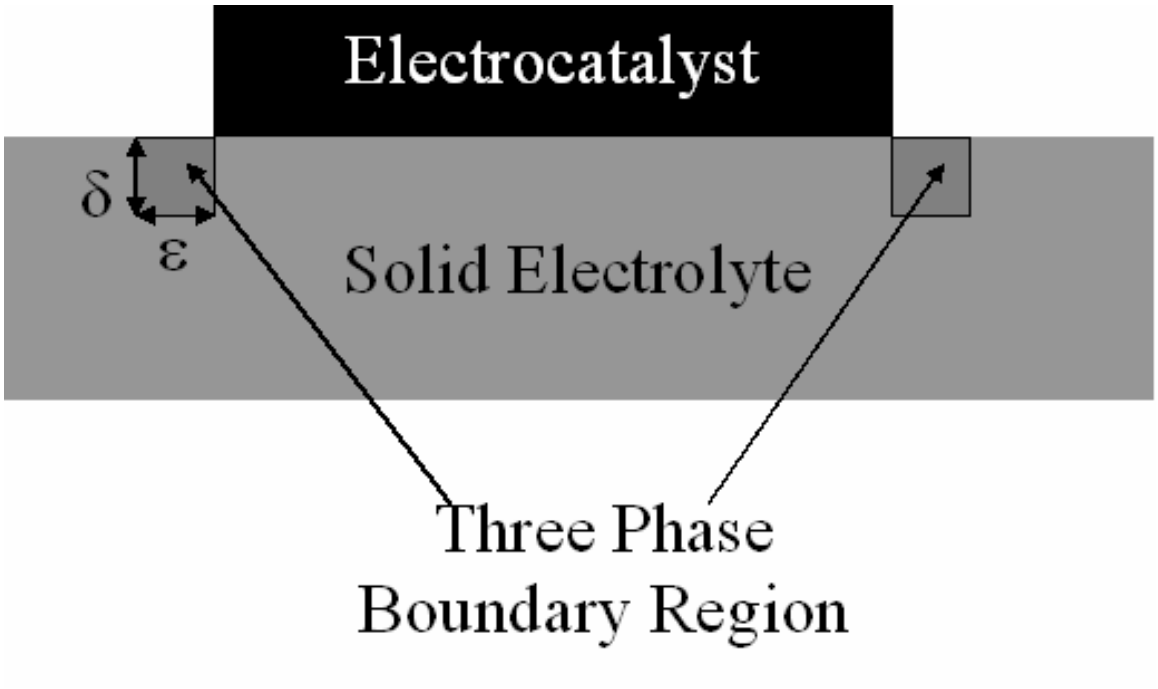


Figure 1: Model for charge transfer at a three phase boundary (TPB).

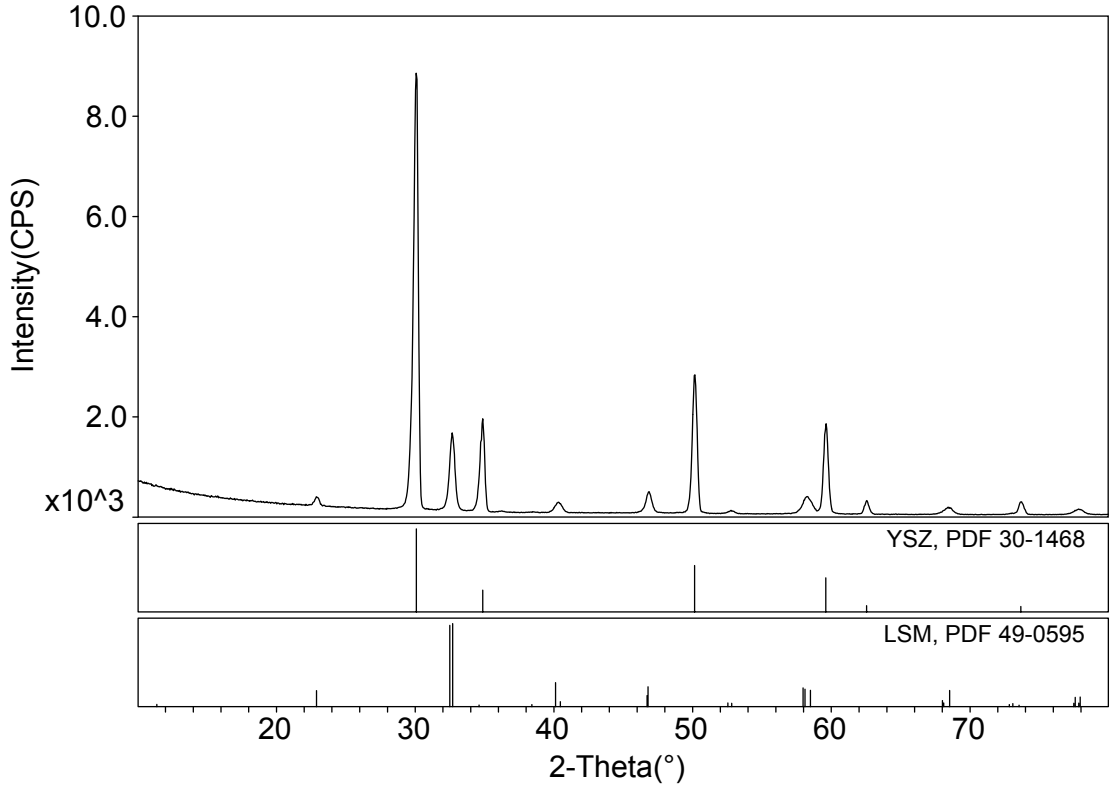


Figure 2: An XRD pattern of sputtered LSM film after annealing at 1000^{o}C for 2 hours.

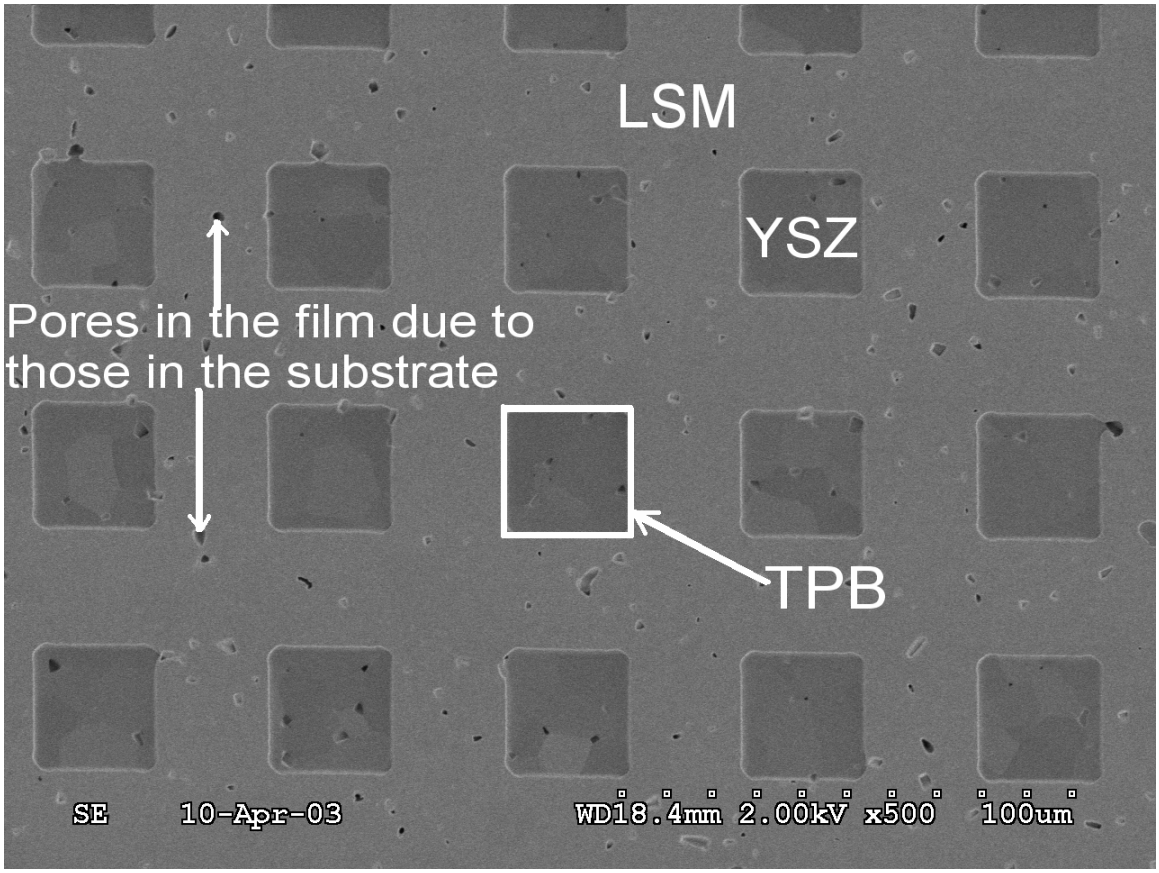


Figure 3: An SEM image of LSM patterned electrode on YSZ with $l_{TPBp} = 430\ \text{cm}^{-1}$.

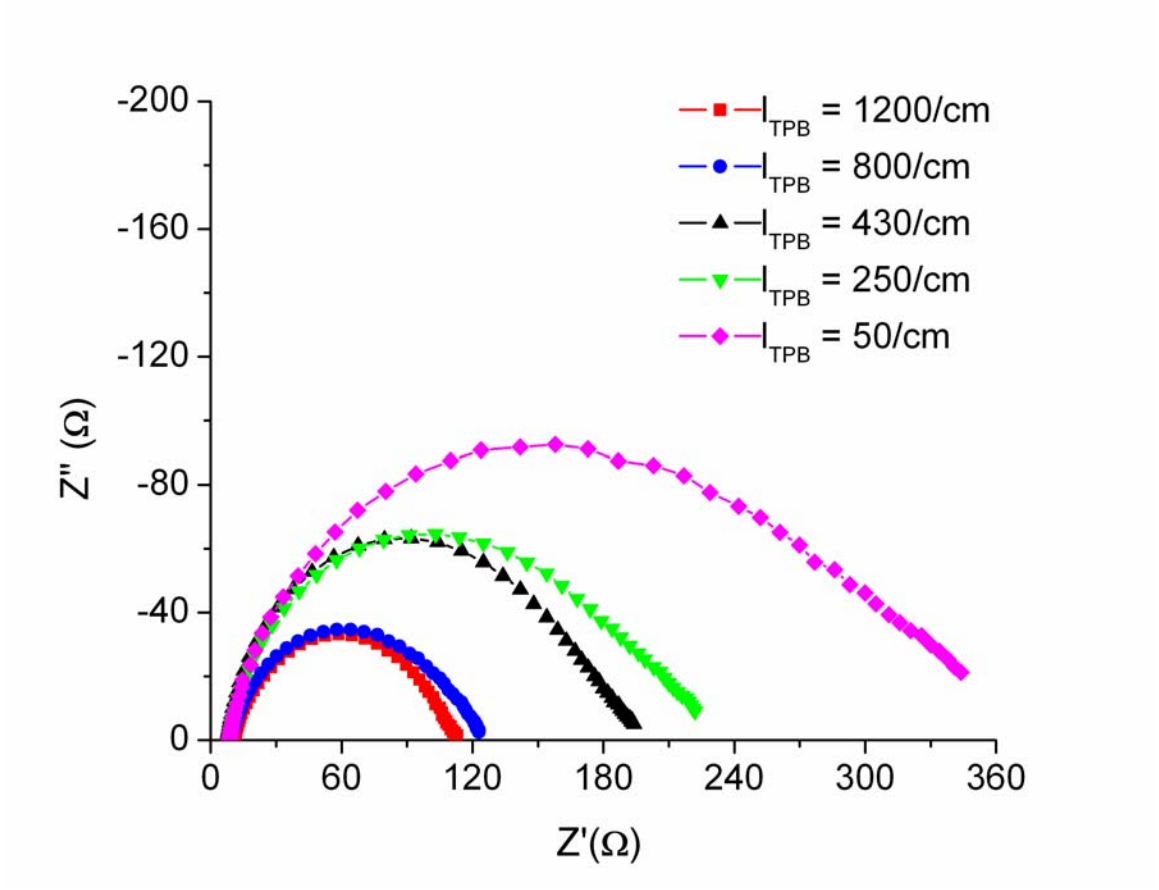


Figure 4: Impedance Spectra of cells with different l_{TPBp} in air at 800°C.

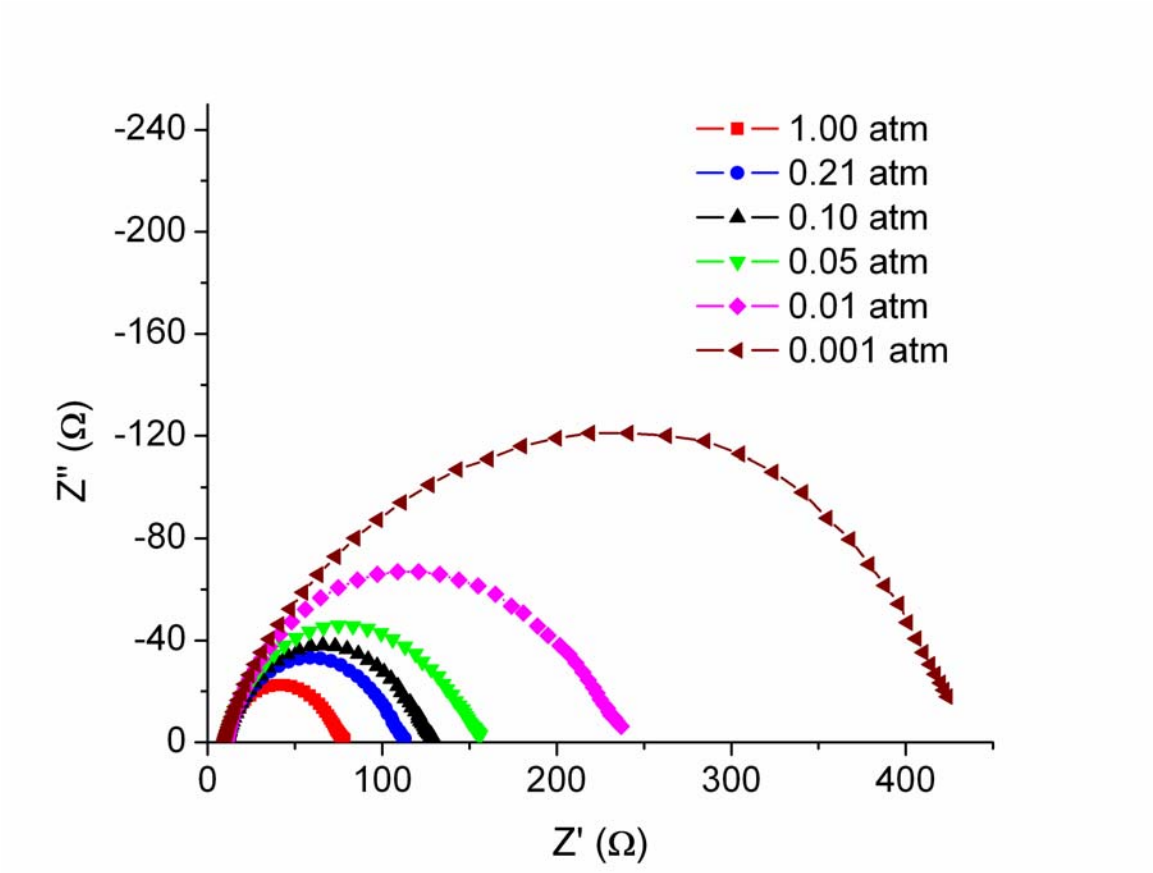


Figure 5: Impedance Spectra of a cell with $l_{TPBp} = 1200$ cm^{-1} at 800°C for different p_{O_2}.

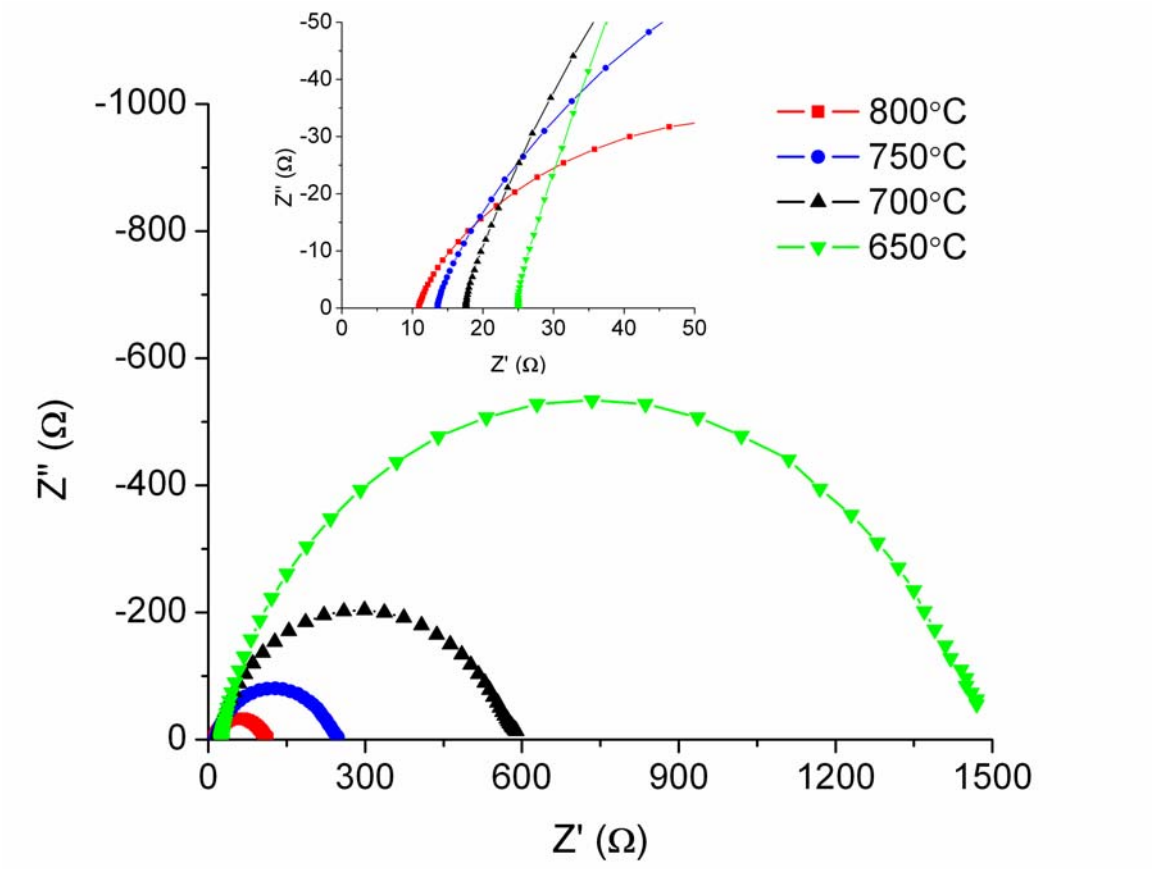


Figure 6: Impedance Spectra of a cell with $l_{TPBp} = 1200$ cm^{-1} in air at different temperatures. The inset shows enlarged region of the high frequency intercepts at various temperatures.

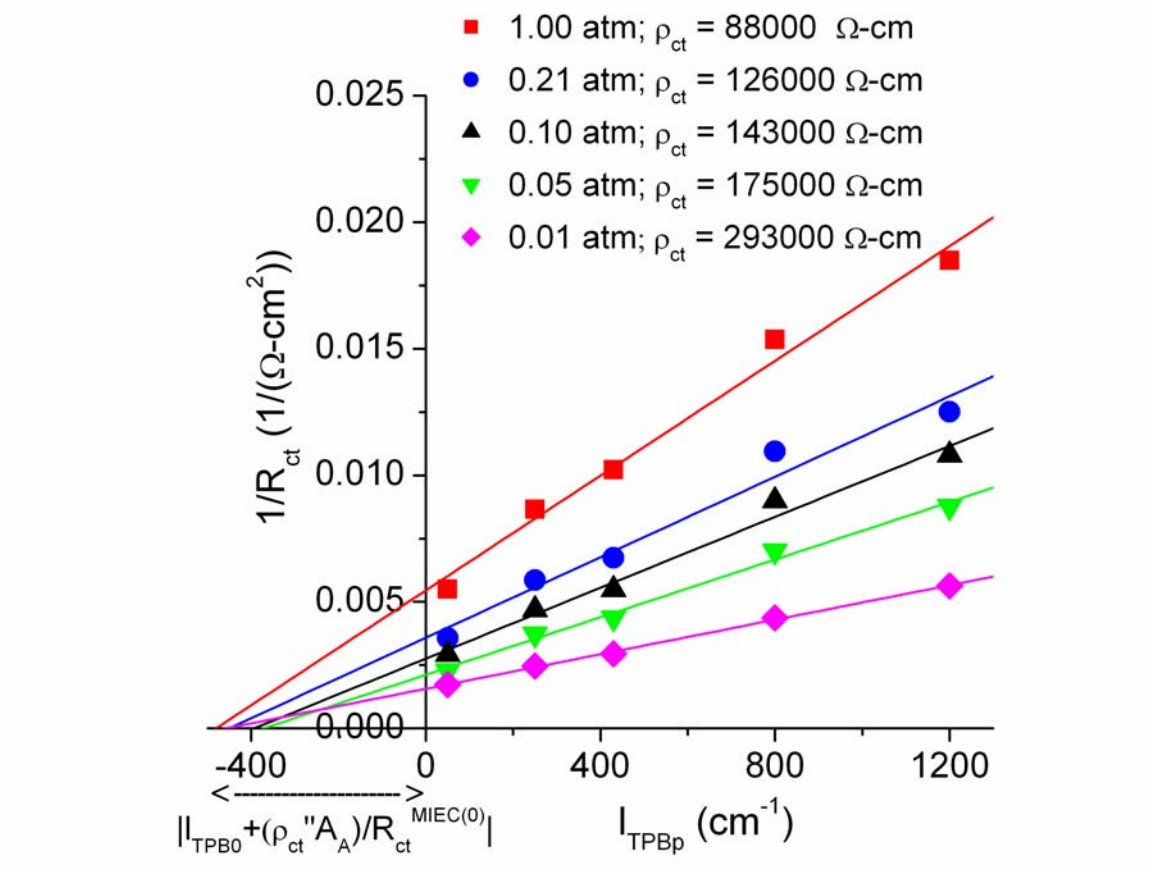


Figure 7: Plots of $1/R_{ct}$ vs. l_{TPBp} at 800°C at different p_{O_2}.

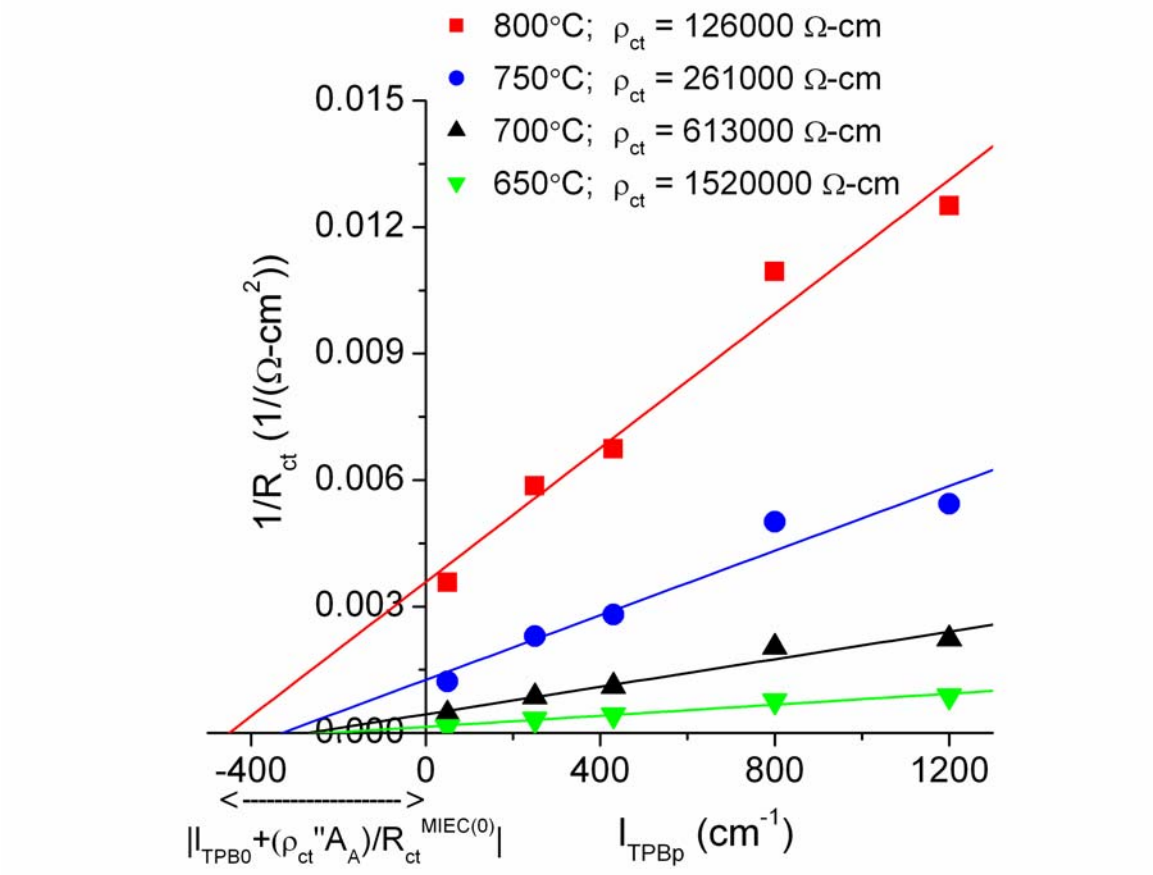


Figure 8: Plots of $1/R_{ct}$ vs. l_{TPBp} in air at different temperatures.

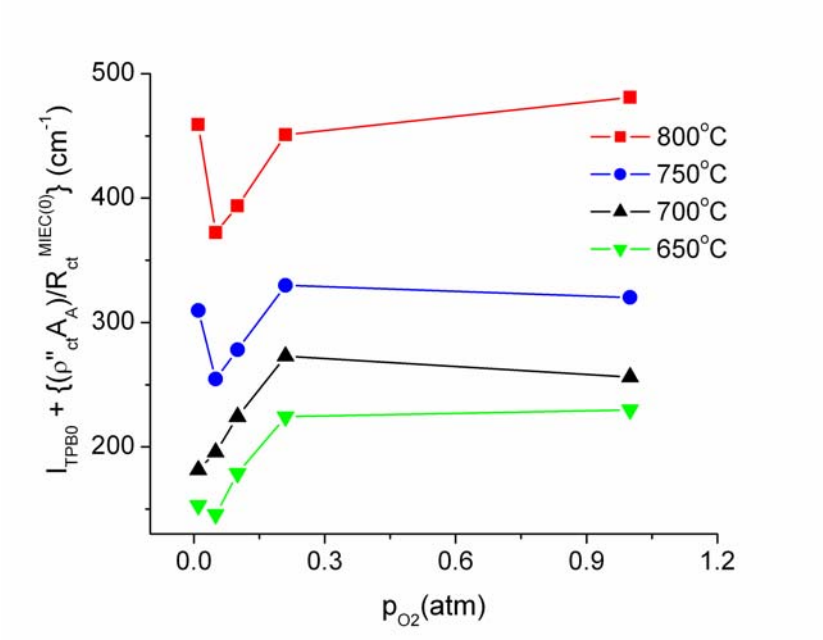


Figure 9(a): Plots of $l_{TPB0} + \frac{\rho''_{ct} A_A}{R_{ct}^{MIEC(0)}}$ vs. oxygen partial pressure at several temperatures.

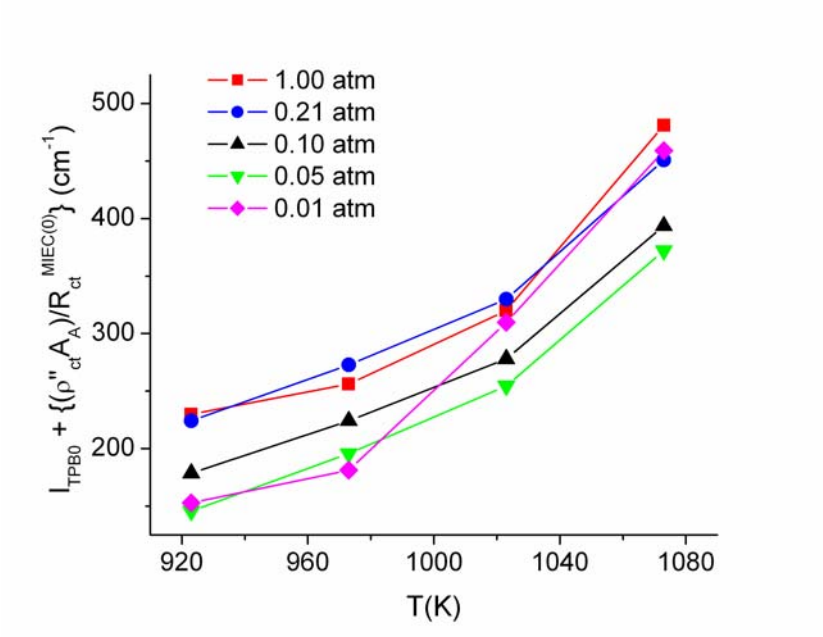


Figure 9(b): Plots of $l_{TPB0} + \frac{\rho''_{ct} A_A}{R_{ct}^{MIEC(0)}}$ vs. temperature at several oxygen partial pressures.

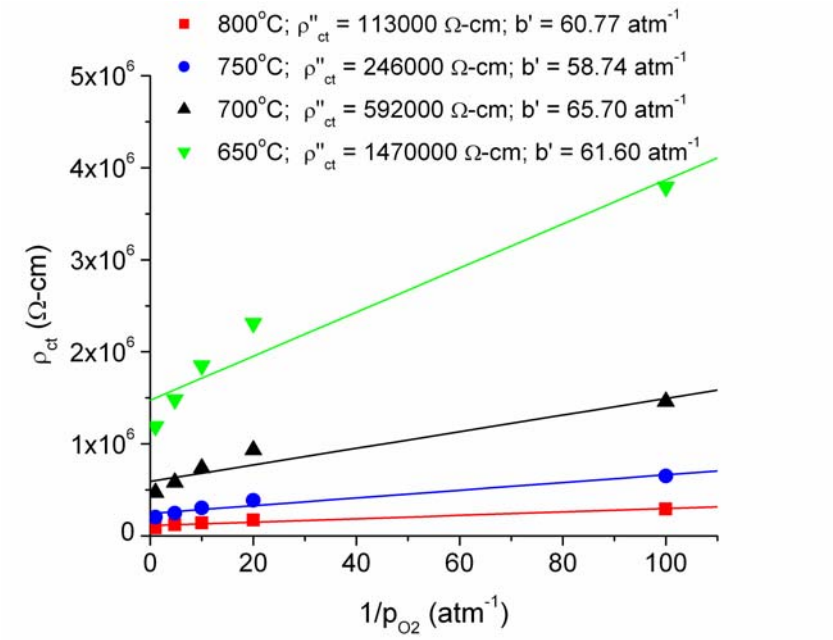


Figure 10(a): Plots of ρ_{ct} vs. $1/p_{O_2}$ at different temperatures (associative adsorption model).

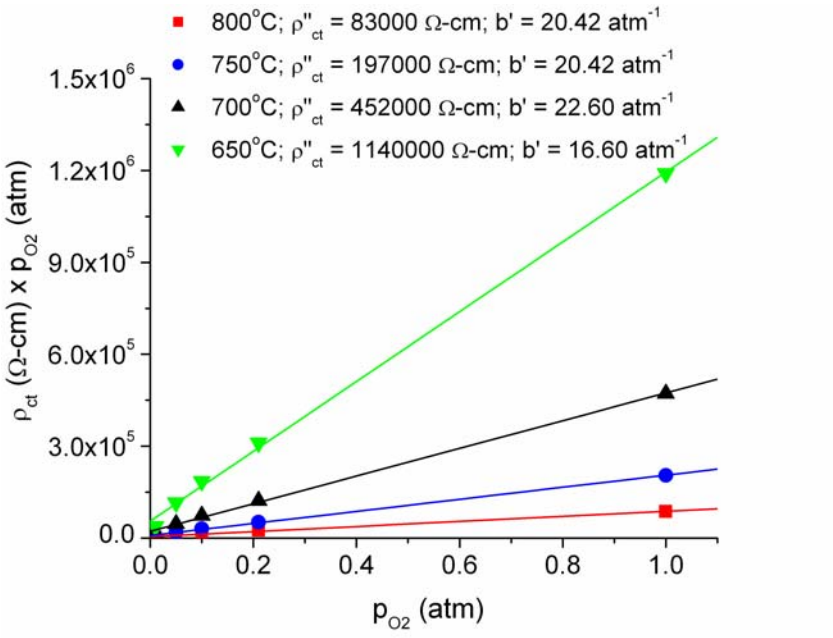


Figure 10(b): Plots of $\rho_{ct} p_{O_2}$ vs. p_{O_2} at different temperatures (associative adsorption model).

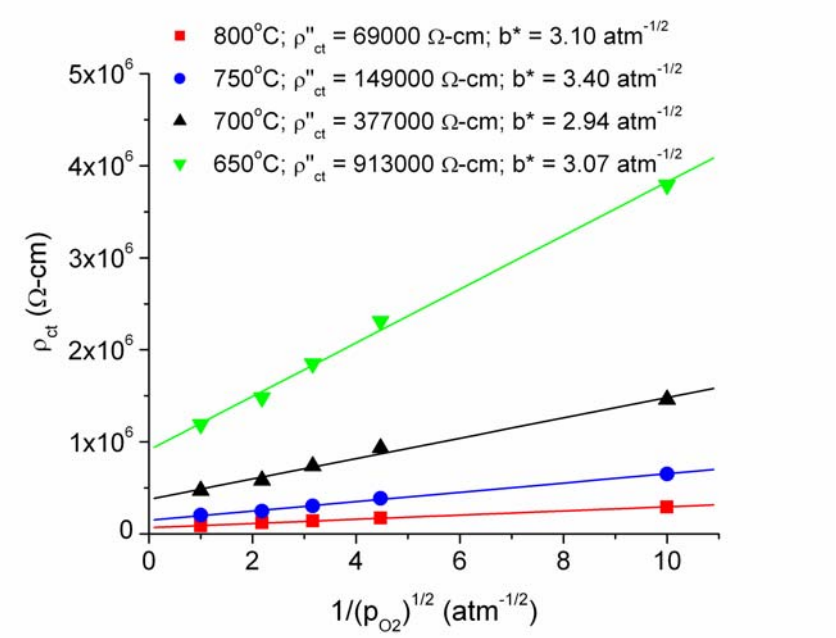


Figure 11(a): Plots of ρ_{ct} vs. $1/\sqrt{p_{O_2}}$ at different temperatures (dissociative adsorption model).

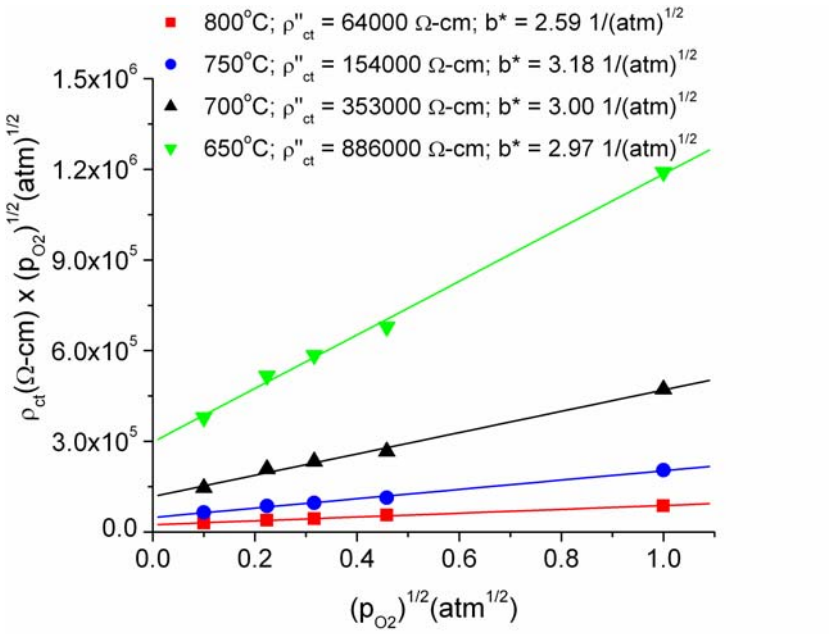


Figure 11(b): Plots of $\rho_{ct}\sqrt{p_{O_2}}$ vs. $\sqrt{p_{O_2}}$ at different temperatures (dissociative adsorption model).

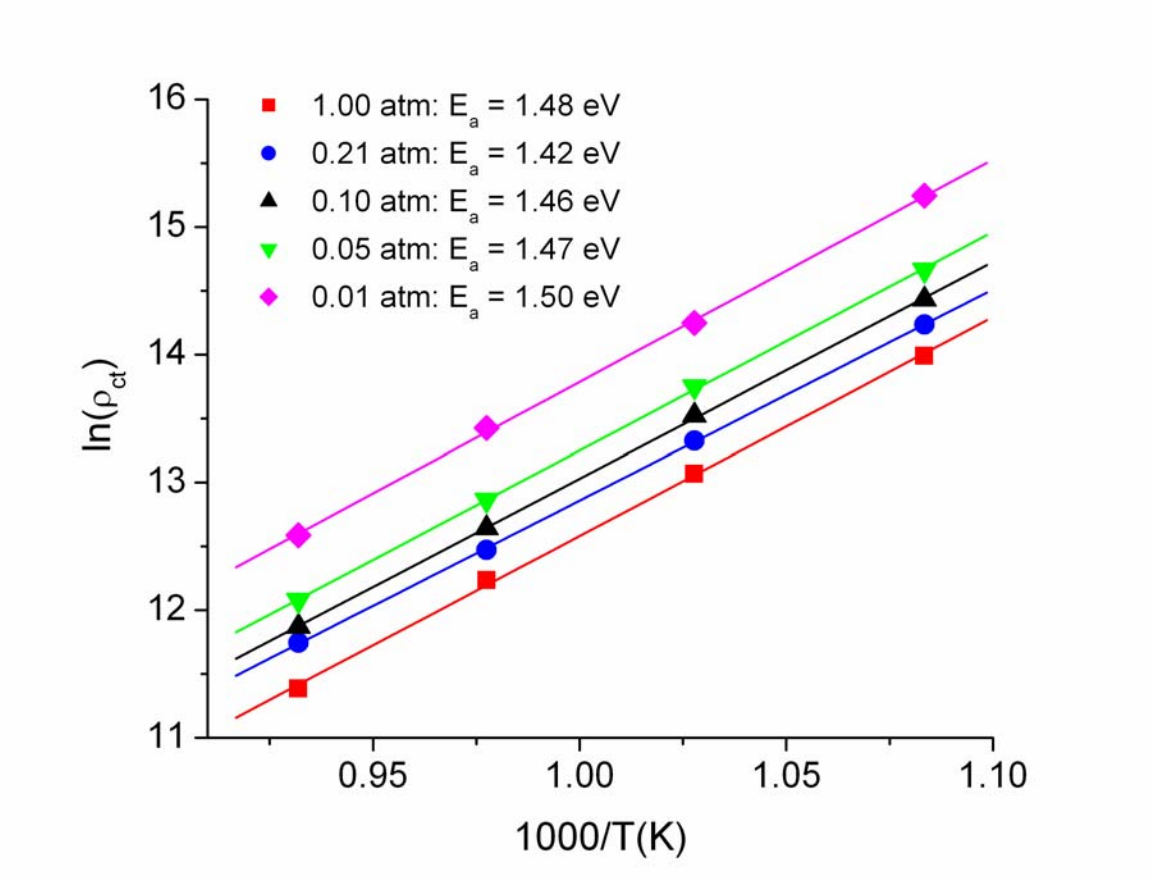


Figure 12: Arrhenius plots of ρ_{ct} at different oxygen partial pressures.

APPENDIX-II

MEASUREMENT OF SURFACE EXCHANGE COEFFICIENT ON POROUS $La_{0.6}Sr_{0.4}CoO_{3-\delta}$ SAMPLES BY CONDUCTIVITY RELAXATION

Ramanan Ganeshananthan and Anil V. Virkar
Department of Materials Science and Engineering
122 S. Central Campus Drive
University of Utah
Salt Lake City, UT 84112

ABSTRACT

A novel technique using conductivity relaxation on porous bodies was used to determine the oxygen surface exchange coefficient, k_{chem}, of mixed conducting $La_{0.6}Sr_{0.4}CoO_{3-\delta}$ (LSC40). The results from the porous bodies were compared with values of k_{chem} obtained from dense samples of LSC40 using the same technique. Conductivity relaxation experiments were carried out from 600 to 800ºC for small p_{O2} step changes, both decreasing and increasing, from 0.02 to 0.21 atm. The k_{chem} obtained from a porous body at a given temperature was found to increase in the range from 10^{-6} to 10^{-5} cm/s over the p_{O2} range from 0.02 to 0.21 atm, with some leveling off at the higher p_{O2}'s close to 0.21 atm. Over the temperature range investigated, the k_{chem} was found to increase with decreasing temperature, with the dependence described by an enthalpy of -23 kJ/mol. This contrasted sharply with the results obtained from the dense samples, in which the k_{chem} was found to increase with increasing temperature, with the corresponding activation energy of 220 kJ/mol. This discrepancy was rationalized on the premise that in dense samples, transport was predominantly controlled by chemical diffusion, which made accurate determination of k_{chem} difficult. The increasing k_{chem} with decreasing temperature in porous samples is believed to be due to chemisorption of oxygen, which is expected to lead to increased surface coverage at lower temperatures.

I. INTRODUCTION

Mixed ionic and electronic conducting (MIEC) materials transport both ionic and electronic species, and thus can effectively transport (permeate) atomic or molecular species. MIEC materials are potential candidates as electrodes and permeation membranes in industrial electrochemistry. MIEC materials with O^{-2} as the mobile ionic species are being explored for applications such as membranes for oxygen separation, synthesis of syngas, and as electrodes for solid oxide fuel cells (SOFCs) and sensors. Considerable work has been reported on the fabrication and characterization of a number of such MIEC materials. The description of transport kinetics in MIECs requires the knowledge of two parameters, namely the chemical diffusion coefficient, $\widetilde{D}$, and the chemical surface exchange coefficient, k_{chem}. The former describes transport through the membrane, while the latter describes transport across the gas phase/solid phase interface. These coefficients, together with conductivity and stability, determine the suitability of such materials for use in solid-state electrochemical devices.

Many oxide perovskites containing a rare earth on the A-site, and a transition element on the B-site, when acceptor-doped, are known to be good MIEC materials. Strontium doped lanthanum cobaltite, $La_{1-x}Sr_xCoO_{3-\delta}$ (LSC), is an important MIEC ceramic since it exhibits excellent MIEC properties. This material, therefore, has been extensively investigated as a membrane for oxygen separation, and as a cathode in SOFCs.

The parameters $\widetilde{D}$ and k_{chem} are expected to be functions of composition, microstructure, temperature and atmosphere. Conventional methods for determining $\widetilde{D}$ and k_{chem} include radio isotope, O^{18}, oxygen exchange (analyzed using secondary ion mass spectroscopy - SIMS) and oxygen permeation experiments. In recent years, the conductivity relaxation technique has been widely used for the measurement of $\widetilde{D}$ and k_{chem}. This technique involves the measurement of conductivity of an MIEC material as a function of time upon an abrupt change in the ambient p_{O2}. When exposed to such a p_{O2} change, the sample under test re-equilibrates to the new p_{O2} with a concomitant change in conductivity. This change could be an increase or decrease, depending on whether the new atmosphere is more oxidizing or more reducing and upon the pertinent defect chemistry. An analysis of the change of conductivity with time on a dense sample can be used to estimate the values of $\widetilde{D}$ and k_{chem}, using the mathematical solution of the diffusion equation as outlined by Crank [1].

Transport of oxygen across the atmosphere/membrane interface is governed by k_{chem}, and transport through the membrane is governed by $\widetilde{D}$. The ratio of $\widetilde{D}$ to k_{chem}, for a given temperature and atmosphere, has units of length and is defined as the critical thickness, l_{cr} [2]. For samples thicker than l_{cr}, the overall kinetics of oxygen transport (or incorporation) is governed by $\widetilde{D}$, and for thinner samples it is governed by k_{chem}. For LSC this critical length lies in the range from tens to hundreds of microns, depending on doping, stoichiometry and temperature [3,4].

When the sample thickness is much less than l_{cr}, the four-probe conductivity response (when a po_2 change is made in the ambient atmosphere and over short time scales) is indicative of a regime where oxygen surface exchange kinetics is rate limiting. Typically, studying this regime in LSC requires a sample tens of microns or less in thickness. Experimentally, it is difficult to work with samples much thinner than ~150 microns. Chen et al. [5] therefore used a dense thin film (< 1 μm) grown on a substrate by pulsed laser deposition (PLD) to estimate values of k_{chem} in this manner. However, they observed an appreciable difference in k_{chem} determined from bulk samples and thin films. The observed differences were attributed to differences in the microstructure/morphology between films deposited by PLD and samples made by conventional ceramic processing techniques.

An alternate possible experimental configuration in which transport kinetics may be governed by k_{chem} involves the use of a porous sample in conductivity relaxation. The experimental approach is essentially identical to that used on dense bodies. When a porous sample is subjected to an abrupt p_{O2} change, four processes occur, each having a different time constant or a characteristic time. The four processes are: (1) Change of atmosphere in the chamber. (2) Transport of the gaseous atmosphere into the porous interstices of the porous sample. (3) Surface exchange on the interior surfaces of the porous body. (4) Chemical diffusion of oxygen into the particles of the sample. In order to facilitate the determination of k_{chem} by this technique, it is necessary that step (3) be the slowest; that is, having a time constant or a characteristic time greater than those for the other three processes. By a proper design of the chamber, and by adjusting the gas

flushing rate, the time constant/characteristic time for the first process can be made quite small. By ensuring that the sample is sufficiently porous and relatively thin, the time constant/characteristic time for the second step can similarly be made very small. Finally, by ensuring the smallest possible particle size, the diffusion distance for chemical diffusion of oxygen into the particles can also be minimized. The time required for oxygen transport by diffusion into the particles in such a microstructure (governed by $\widetilde{D}$) is estimated to be less than 1 second for LSC at 800ºC. In this manner, in principle, a porous body can be used to make measurements of k_{chem} by conductivity relaxation. The use of a porous sample instead of using a deposited film is also expected to closely resemble the actual cathodes in a SOFC, which are porous and of a fine microstructure.

The objective of this work was to study the surface exchange characteristics of $La_{0.6}Sr_{0.4}CoO_{3-\delta}$ (LSC40) using a porous sample where the average particle size and pore size are on the order of a few microns. If the kinetics is governed by surface exchange, a simple first order differential equation with a single time constant describes the kinetics. Since k_{chem} is expected to be a function of oxygen partial pressure, in the present work step changes were limited to ~ 0.02 to 0.03 atm, so that over any given and yet narrow p_{O2} range, the k_{chem} can be regarded as a constant. Values of k_{chem} so obtained were compared to values obtained from dense LSC samples from our own lab and from the known literature.

II. THEORETICAL BACKGROUND

Using conventional ceramic processing it is possible to make dense LSC40 samples down to a few hundred microns in thickness. This size range is reportedly suitable for the determination of both $\widetilde{D}$ and k_{chem} at 800ºC by the conductivity relaxation technique, for which l_{cr} is also on the order of a few hundred microns. However, the use of the same samples for relaxation experiments below 750-700ºC is expected to yield measurements that are increasingly sensitive to the diffusion coefficient only, as l_{cr} decreases with decreasing temperature. Apart from sputtering and specialized vapor deposition techniques, it is difficult to fabricate dense samples of LSC in the range of l_{cr} required for measurements at lower temperatures. Also, as stated before, the properties of thin films made by vapor phase techniques can vary notably from bulk ceramics.

Transport kinetics of dense samples with thickness comparable to l_{cr} depend on both $\widetilde{D}$ and k_{chem}. For the geometry of the dense samples used in this study, the data are analyzed for transport in an infinite plate of finite thickness (2*l*), using the diffusion equation:

$$\frac{\partial C}{\partial t} = \widetilde{D}\frac{\partial^2 C}{\partial x^2} \qquad -l \leq x \leq l \qquad (1)$$

with the initial condition

$$C(x, 0) = C(0) \qquad -l \leq x \leq l$$

and boundary conditions

$$C(-l, t) = C(l, t) = C_o \qquad t > 0$$

and

$$-\widetilde{D}\left.\frac{\partial C(x,t)}{\partial x}\right|_{x=\pm l} = k_{chem}(C_o - C_s(t)) \qquad t > 0 \qquad (2)$$

where C_o is the concentration of oxygen in the sample after equilibration to a new p_{O2}, $C(0)$ is the initial concentration of oxygen in the sample corresponding to the initial p_{O2}, and $C_s(t)$ is the concentration of oxygen just inside the sample surface at time t. Using the solution of the diffusion equation given by Crank [1], the normalized conductivity $g(t)$, for a dense sample of thickness $2l$, can be described by:

$$g(t) = \frac{\sigma(t) - \sigma(0)}{\sigma_\infty - \sigma(0)} = \frac{C(t) - C(0)}{C_o - C(0)} = \frac{M(t)}{M_\infty} = 1 - \sum_{n=1}^{\infty} \frac{2L^2 \exp(-\beta_n^2 \widetilde{D} t / l^2)}{\beta_n^2(\beta_n^2 + L^2 + L)} \qquad (3)$$

where $\sigma(0)$ is the initial conductivity, σ_∞ is the conductivity after the sample is equilibrated to the new p_{O2} (that corresponding to C_o), and $\sigma(t)$ is the conductivity after time t, which corresponds to $C(t)$, the average concentration at time t, which is defined as:

$$C(t) = \frac{1}{2l}\int_{-l}^{+l} C(x,t)dx \qquad (4)$$

$M(t)$ is the net amount of oxygen that entered (left) in time 't' after the change in p_{O2} and M_∞ is the net amount of oxygen that entered (left) after an infinite time following the change in p_{O2}. The preceding assumes a linear relation between conductivity and concentration. The 'β_n's are the positive roots of the transcendental equation

$$\beta_n \tan \beta_n = L \qquad (5)$$

and

$$L = \frac{l k_{chem}}{\widetilde{D}} \qquad (6)$$

Frequently a least-squares fitting program is used to fit experimental data to this model. Values of β_n can be easily obtained using a numerical procedure given by den Otter et al. [7].

By using porous LSC samples, in which the average particle size is on the order of a few tens of microns, it is possible to achieve faster equilibration in conductivity relaxation experiments even at low temperatures. In fact, for porous samples with an average particle size on the order of a few microns, the kinetics of conductivity relaxation is expected to be dictated exclusively by k_{chem} (average particle size << l_{cr}). The objective of this work was to investigate this regime of kinetic behavior. In this case, diffusion in very small particles is assumed fast, so that the concentration is essentially uniform within the solid at any time during equilibration. If the specific surface area of the porous body of volume fraction porosity V_v is given by S_V (in cm^2/cm^3 or cm^{-1}), where the average concentration at time *t* is $C(t)$ and the final equilibrated concentration is C_o, the rate of oxygen incorporation (or expulsion) is given by

$$S_V k_{chem}\left(C_o - C(t)\right)dt = \left(1 - V_v\right)dC(t) \tag{7}$$

the integration of which gives

$$\frac{C_o - C(t)}{C_o - C(0)} = \exp\left[-\frac{t}{\left(\frac{1-V_v}{S_V k_{chem}}\right)}\right] = \exp\left[-\frac{t}{\tau_r}\right] \tag{8}$$

which represents first order kinetics with time constant given by

$$\tau_r = \frac{\left(1 - V_v\right)}{S_V k_{chem}} \tag{9}$$

In terms of the measured parameter, namely the normalized conductivity function $g(t)$, the above may also be written as

$$g(t) = \frac{\sigma(t) - \sigma(0)}{\sigma_\infty - \sigma(0)} = 1 - \exp\left[-\frac{t}{\tau_r}\right] = 1 - \exp\left[-\frac{t}{\left(\frac{1-V_v}{S_V k_{chem}}\right)}\right] \quad (10)$$

The experimental procedure consists of measuring the time dependence of conductivity after an abrupt change in atmosphere, and fitting a first order kinetic equation to the normalized conductivity, $g(t)$ vs. t plot, and determining the time constant, τ_r, which is related to k_{chem}, V_v, and S_V by equation (9). Volume fraction porosity, V_v, can be measured by the conventional Archimedes fluid immersion method as well as by a systematic point count by quantitative stereology [6]. The specific pore surface area, S_V, can be determined using quantitative stereology [6]. From these measurements, k_{chem}, thus can be determined using porous samples, given in terms of measured parameters by

$$k_{chem} = \frac{1-V_v}{S_V \tau_r} \quad (11)$$

III. EXPERIMENTAL PROCEDURE

$La_{0.6}Sr_{0.4}CoO_{3-\delta}$ (LSC40) powder was prepared in-house by a solid-state reaction between La_2O_3 (Alfa, 99.99%), $SrCO_3$ (Aldrich, 99.9%) and Co_3O_4 (Alfa, 99.7%) in the required stoichiometry. Starting powders were mixed and ball milled in ethanol using ¼" zirconia grinding media (U.S. Stoneware) for 24 hours, dried and calcined at 1100ºC for 12 hrs to form LSC40. The calcined powder was ball milled in ethanol for an additional 24 hrs.

LSC40 powder, prepared from combustion synthesis, was also procured from a commercial vendor (Praxair Specialty Ceramics).

LSC40 powder was mixed with 13 wt.% carbon (HTW – Germany, 10-20 μm spherical particles) and ball milled in ethanol for 24 hrs. The dried powder was mixed with 3 wt.% ethylene glycol (as binder) and bars were uniaxially pressed at 7,000 lbs for 1 minute. The pressed bars were heated at 1ºC/min in air to 500ºC to burn off the carbon and create porosity, and then sintered in air at 1150ºC for 1 hr. At this temperature the carbon is completely burned out. A few bar samples made from both sources of powder were impregnated with epoxy and polished to a level finish for stereological analysis on a scanning electron microscope (SEM).

For the fabrication of dense samples, bars of LSC40 (without adding carbon) were pressed uniaxially followed by isostatic pressing at 32,000 psi. The bars were then sintered at 1250ºC for 6 hrs. The sintered bars were ground and hand polished to a thickness of ~ 200 μm. X-ray powder diffraction (XRD) was used to determine the phase purity of both the porous and dense samples. Silver mesh and paste were used to attach silver test leads in a four-probe configuration. The sample was then placed in a quartz reaction chamber and inserted into a tube furnace for the conductivity relaxation measurements.

In reality the assumed 'step change' in p_{O2} in relaxation experiments is not instantaneous and there is a finite gas exchange time. It has been shown that gas exchange times of

more than a few seconds can adversely affect the accuracy of the data, especially at short time periods [8]. This is particularly the case with poorly designed sample chambers in which the chamber volume is large and turbulent gas mixing tends to occur. The time constant, τ_{ch}, to flush the chamber with a new atmosphere as defined by den Otter et al. [9] is given by

$$\tau_{ch} = \frac{V_{\mathrm{r}}}{\Phi_{\mathrm{v.tot}}} . \frac{T_{\mathrm{STP}}}{T_{\mathrm{r}}} \tag{12}$$

where V_r and T_r are the reactor volume and temperature, respectively, $\Phi_{\mathrm{v.tot}}$ is the flow rate of the gas and T_{STP} refers to room temperature. The experiments carried out in this study were conducted in a specially designed and built quartz tube. The effective volume of the sample chamber, i.e. chamber volume minus volume of sample and insulated current leads, was ~6.3±0.5 cm^3. At a gas flow rate of 600 ml/min, the time constant for switching the atmosphere in the chamber at 800˚C was approximately 0.17 sec.

A thermocouple was placed inside the sample chamber to measure any possible temperature fluctuations during the relaxation measurements. Conductivity relaxation experiments were carried out in the temperature range from 600 to 800˚C in 50 degree intervals, in the oxygen partial pressure range 0.02 to 0.21 atm for the following p_{O2} step changes (both decreasing and increasing): 0.21 to 0.18 atm, 0.18 to 0.16 atm, 0.16 to 0.14atm, 0.14 to 0.12 atm, 0.12 to 0.10 atm, 0.10 to 0.08 atm, 0.08 to 0.06 atm, 0.06 to 0.04 atm and 0.04 to 0.02 atm. Conductivity relaxation measurements at larger p_{O2} step changes of 0.21 to 0.10 atm, 0.10 to 0.05 atm and 0.05 to 0.01 atm were also carried out.

The voltage and current were measured using a Solartron 1287 Electrochemical Interface and recorded using 'CorrWare' software from Scribner Associates.

IV. RESULTS AND DISCUSSION

Figure 1 shows an SEM micrograph of a porous LSC40 bar (made from the in-house powder) that was used for the relaxation experiments. The average particle size is around 2-3 μm. A line intersection analysis was carried out to determine the intersection count, P_L [6]. The pore surface area per unit volume, S_V, of the randomly oriented surfaces of a porous body can be obtained from the equation [6]:

$$S_V = 2P_L \text{ cm}^{-1} \tag{13}$$

From the measurements S_V was estimated to be ~ 7930 cm^{-1}. The porosity of this sample using the Archimedes method was measured to be 30%. The porosity measured using the statistical point count method [6] was 29.5%. The agreement between these two methods, within experimental scatter, indicates that most of the porosity is open. For this reason, the measured S_V was assumed to be the same as would be accessible to the gas phase. Similar measurements on a LSC40 bar made using powder from Praxair gave S_V ~ 10,840 cm^{-1}, with a porosity of approximately 25% from both the Archimedes and stereological porosity measurements.

The application of the conductivity relaxation technique to porous bodies assumes that transport of gases in the porous interstices is much faster than the kinetics of surface exchange. An estimate of the time required for gas diffusion to occur into the pores of the

sample was made to study the kinetics of oxygen transport through the pores, into the interior of the sample. The objective was to determine if the kinetics of this transport was fast enough to assume it to be essentially instantaneous. This calculation was based on the assumption of binary diffusion into the porous body. The effective diffusion coefficient, D_{eff}, of oxygen-nitrogen through porous bodies is given by [10]:

$$D_{eff} = \frac{D_{O2-N2} V_v}{\varepsilon} \tag{14}$$

where $D_{O2\text{-}N2}$ is the binary diffusion coefficient of oxygen-nitrogen, which can be calculated using the Chapman-Enskog model [11], V_v is the porosity, and ε is the tortuosity factor. A one dimensional diffusion equation was solved numerically using D_{eff} and the time required for the p_{O2} in the center of the sample to reach 99% of the p_{O2} after the switch was calculated. The results for the two porous LSC40 samples, for an assumed tortuosity factor of 5, are given in Table 1, which show that gas diffusion into the pores occurs within 0.07 to 0.11 sec over the temperature range investigated.

Figure 2 shows the plots of normalized conductivity, *g(t)*, versus time for the porous LSC40 sample made from the in-house powder for a p_{O2} change of 0.21 to 0.18 atm at two temperatures, 600 and 800°C, under an applied current of 1.5 amps. An important point to note is that the kinetics of equilibration is faster at lower temperature, the possible explanation of which is given later. Also shown in the figure are the best fits to equation (10), which gave τ_r = 2.48 seconds with the corresponding R^2 = 0.99 at 800°C, and τ_r = 1.04 seconds at 600°C with the corresponding R^2 = 0.96. At 800°C, the sample re-equilibration time constant is over 14 times larger than the chamber time constant, and at 600°C it is about 6 times. Comparison with Table 1 also shows that the kinetics of

gaseous diffusion into the porous interstices is much faster as compared to the sample re-equilibration time. Finally, much of the published work shows that the $\widetilde{D}$ for LSC40 at 600°C is on the order of 10^{-7} to 10^{-6} cm^2/s, and increases with increasing temperature. The approximate particle size of the LSC40 sample in the present work was ~3 microns, or a diffusion distance of ~1.5 microns. Assuming $x \sim \sqrt{\widetilde{D}t}$, the time required for chemical diffusion to occur into the individual particles is therefore estimated to be <~0.22 seconds. This shows that for the present porous samples, the slowest step corresponds to the surface exchange kinetics. This is consistent with the observation that the data can be fitted to equation (10), where the single rate controlling parameter must be from surface and interfacial phenomena related to k_{chem}. It is also noted that any nano-scale effects are expected to be negligible for a porous body with average particle size of 2 to 3 microns since the number of atoms in the bulk of a particle is approximately 4 orders of magnitude larger than the surface atoms.

If the applied current is small (below about 0.4A), the measured signal is small. If the current is too high, there is the possibility that temperature changes could occur due to resistive heating. For most of the testing under small p_{O2} step changes, the current applied therefore was 0.8A. Larger p_{O2} step changes were still conducted at a current of 0.4A.

The chemical surface exchange coefficient, k_{chem}, is related to the time constant τ_r, the pore surface area per unit volume, S_V, and volume fraction porosity, V_v, by equation (11), given earlier. The k_{chem} values so obtained at 800ºC for the LSC40 in-house sample are plotted in Figure 3 as a function of p_{O2} during decreasing and increasing p_{O2} step

changes. The p_{O2} indicated is an average between the initial and final p_{O2} for each measurement. The figure shows that k_{chem} is a function of p_{O2}, with k_{chem} increasing with the average partial pressure. The k_{chem} appears to be more sensitive to partial pressure changes at low p_{O2} with some leveling off occurring at higher p_{O2}'s. There also appears to be no significant difference between the measurements during decreasing or increasing p_{O2} steps at 800ºC.

The values of k_{chem} obtained for the same sample over the temperature range 600 to 800ºC are shown in Figures 4 and 5 for decreasing and increasing p_{O2} step changes, respectively. It is clear that the same trend is maintained even at lower temperatures with an overall increase in k_{chem} with increasing p_{O2} but with a decreasing dependence at higher p_{O2}'s. However, the most important feature of the plots is the dependence of k_{chem} on temperature. The plots clearly show that the surface exchange coefficient increases with decreasing temperature. Arguably, there is little difference in k_{chem} at 800 and 750ºC, but there is a definite increase in k_{chem} as the temperature is lowered below 750ºC.

Figure 6 shows the temperature dependence of k_{chem} with decreasing p_{O2} step changes for the LSC40 sample prepared from the Praxair powder. The values of k_{chem} obtained are on the same order of magnitude (10^{-6} to 10^{-5} cm/s) but are lower by a factor of ~2 than the sample made from the in-house powder. The variation of k_{chem} with p_{O2} is similar and the temperature dependence also clearly shows an increase in k_{chem} when the

temperature decreases from 800 to 600ºC. A similar dependence of temperature and p_{O2} was obtained for the case of increasing p_{O2} step changes for this sample.

The general trend of k_{chem} with p_{O2} for the porous samples at a given temperature is consistent with the results for dense samples of LSC from other groups found in the literature. For example, Van der Haar et al. [12] carried out conductivity relaxation experiments from 600 to 800ºC on dense LSC with strontium doping of 0.7, 0.5 and 0.2. Their results for LSC50 show that for a given temperature, k_{chem} increases from 10^{-5} to 10^{-4} cm/s in the p_{O2} range of 10^{-4} to 10^{-1} bar and tends to level off from 10^{-1} to 1 bar. Similarly, Wang et al. [13] observed that k_{chem} increases with increasing p_{O2} in the range 0.01 to 0.3 atm for dense LSC50 for the temperature range investigated, namely 619 to 696ºC. However, the temperature dependence of k_{chem} is quite different, where both groups show k_{chem} for a given p_{O2} change increases with temperature. Van der Haar's paper includes plots of k_{chem} versus p_{O2} for different temperatures similar in format to Figures 4-6, where k_{chem} is observed to increase with increasing temperature. This is in contrast to the results from the porous samples in this study where k_{chem} increases with decreasing temperature.

The results from the porous samples are also in conflict with the results of k_{chem} versus temperature obtained from dense samples of LSC40 in our own lab. A dense sample of thickness ~218 μm made using in-house powder was used for these measurements. Figure 7 shows plots of normalized conductivity, $g(t)$ vs. time obtained during

conductivity relaxation experiments for a p_{O2} change of 0.21 to 0.10 atm conducted at 700 and 800°C. As seen in the figure, the kinetics of equilibration is much faster at 800°C than at 700°C, in contrast to the results obtained on porous samples. At 800°C, the chemical diffusion coefficient for LSC40, $\widetilde{D}$, is on the order of 10^{-6} cm^2/s. The estimated k_{chem} is on the order of 10^{-5} cm/s at 0.2 atm of p_{O2}. The corresponding l_{cr} is estimated to be a few hundred microns, which is about the sample thickness. Thus, based on the analysis given by den Otter et al. [9], the analysis of the $g(t)$ vs. t can be used to estimate both $\widetilde{D}$ and k_{chem}. At 700°C, however, the k_{chem} (as-determined using the porous samples) is on the order of high 10^{-5} to 10^{-4} cm/s. However, the corresponding $\widetilde{D}$ is on the order of 10^{-7} cm^2/s (or slightly lower), with the corresponding l_{cr} being tens of microns, or smaller. That is, the dense sample is too thick, and estimation of both $\widetilde{D}$ and k_{chem} is expected to be difficult. That is, the $g(t)$ vs. t plots for the dense sample of ~218 microns at 700°C (and lower) are expected to be largely influenced by diffusion. Thus, the accuracy of k_{chem} at 700°C (and lower) determined from such a thick sample is questionable.

Conductivity relaxation data for the dense sample were fitted to equation (3) and $\widetilde{D}$ and k_{chem} were evaluated from the best fit. Figure 8 is an Arrhenius plot of k_{chem} over the temperature range measured for the porous and dense LSC40 samples made using the in-house powder for a p_{O2} switch of 0.21 to 0.10 atm. Note that at 800°C, the k_{chem} determined from both dense and porous samples are about the same. As stated above, at 800°C, the l_{cr} is comparable to sample thickness, which makes it possible to determine

both parameters with reasonable accuracy. At lower temperatures, the k_{chem} obtained from dense samples does not agree with the results from porous samples, both in terms of absolute magnitudes as well as the temperature dependence. The k_{chem} measured on the dense sample shows a thermally activated dependence with an activation enthalpy of 220 kJ/mol. By contrast, the Arrhenius plot of k_{chem} vs. $(1/T)$ for the porous sample from Figure 8 leads to a negative enthalpy of -23 kJ/mol, indicating that k_{chem} does not obey an Arrhenius type of relationship. It should be noted that the model used for the analysis of the dense samples is the same as those used by other groups measuring conductivity relaxation using dense bodies and our dense results were found to be in good agreement with this literature [12-14]. Based on the present results, it is concluded that k_{chem} obtained from dense samples are not reliable at lower temperatures.

An increase in k_{chem} with increasing temperatures is also evident in experiments on dense samples, which have been conducted using O^{18}/O^{16} exchange followed by SIMS analysis [3, 4]. In the SIMS analysis the diffusion of O^{18} into a sample is described by the solution to Fick's second law for a semi-infinite medium, where the boundary condition of flux into the surface in equilibrium with the flux away from the interface to the bulk is the same as Equation (2). Not surprisingly, k_{chem} again shows positive activation energy with temperature for the results from SIMS. It appears that SIMS measurements on annealed samples also suffer from the same difficulty as in the case of conductivity relaxation, insofar as the determination of k_{chem} is concerned.

The temperature dependence of k_{chem} obtained on dense samples used in electrical conductivity relaxation and oxygen permeation experiments is generally explained by the governing reaction thought to occur at the gas/solid interface, where

$$\frac{1}{2}O_2 + V_O^{\bullet\bullet} + 2e' \Leftrightarrow O_O^X \qquad (15)$$

where $V_O^{\bullet\bullet}$ is the oxygen vacancy, and O_O^X denotes an oxygen ion on its sublattice (Kröger-Vink notation is assumed). In this reaction the rate of absorption (or release) of oxygen is dependent on oxygen nonstoichiometry and the ability of the oxygen vacancy to migrate to the surface. Vacancy formation and migration enthalpies are both thermally activated processes, which are believed to account for the positive activation enthalpy found for k_{chem} from measurements on dense samples.

Clearly, the temperature dependence of k_{chem} obtained from porous samples cannot be described by a thermally activated process as governed by Equation (15). In fact, this type of activity is indicative of an exothermic process, which is consistent with gas adsorption on a surface. The surface exchange coefficient over the temperature range measured could then be given, at least qualitatively, in terms of the oxygen surface coverage as described by an adsorption isotherm, such as Langmuir isotherm, where the coverage increases with decreasing temperature. The possible explanation of increasing k_{chem} with decreasing temperature may hinge on a reaction of the following type, namely

$$\frac{1}{2}O_2 \Leftrightarrow O_{ads} \qquad (16a)$$

and

$$O_{ads} + 2e' \Leftrightarrow O_O^{-2} \qquad (16b)$$

in which O_O^{-2} is now an oxygen ion on the surface of LSC. Since O^{-2} is a component in LSC, once electron transfer occurs and a divalent oxygen ion forms, it can be argued that the adsorbed oxygen becomes a part of the crystal; that is, the oxygen ion has now become a part of the crystal. That is, its incorporation into the crystal does not depend upon the presence and the movement of oxygen vacancies. The role of oxygen vacancies is obviously of paramount importance in subsequent transport. However, the present results seem to suggest that vacancies may not play a part in the surface exchange process. If the electron transfer reaction is assumed not to be rate limiting, the overall surface exchange reaction is expected to be dependent upon the degree of surface coverage, the latter expected to increase with decreasing temperature – at least over some temperature. This may be the possible explanation of the observed increase in k_{chem} with decreasing temperature. The chemical diffusion coefficient, $\widetilde{D}$, on the other hand, is naturally expected to decrease with decreasing temperature due to the decided role of oxygen vacancies.

V. CONCLUSIONS

The chemical surface exchange coefficient of oxygen on porous LSC was measured. It was determined that for a porous sample, the rate limiting parameter for oxygen incorporation into LSC over the temperature range investigated is the surface exchange step, which allows unequivocal estimation of k_{chem}, not influenced by chemical diffusion, unlike dense samples. The estimated k_{chem} for the temperature range from 600 to 800^{o}C and over the range of p_{O2} measured are on the order of 10^{-6} to 10^{-5} cm/s and

agree well with data available in the literature. However, unique to this study, the k_{chem} (from porous samples) was found to increase with decreasing temperature. The rate-limiting step, for a given switch in p_{O2}, was clearly not thermally activated and plots of k_{chem} with temperature were found to have a negative activation enthalpy of -23 kJ/mol. This is in contrast to results for conductivity relaxation on dense LSC samples conducted in our lab as well as from data available in the literature, where k_{chem} is found to increase with increasing temperatures. It appears that k_{chem} estimated from the analysis of dense samples, especially at lower temperatures, is influenced by the chemical diffusion coefficient, $\widetilde{D}$, and thus is not reliable. Further experimentation and modeling of possible rate determining steps is under way in an attempt to explain this behavior.

ACKNOWLEDGEMENTS

This work was supported by the United States Department of Energy (DOE) under contract DE-FC26-02NT41565.

REFERENCES

1. J. Crank, *Mathematics of Diffusion*, 2nd Edition, p. 60, Oxford University Press, Oxford, UK (1995).
2. B. C. H. Steele, *Solid State Ionics*, **75**, 157-165 (1995).
3. S. Carter, A. Selcuk, R. J. Chater, J. Kajda, J. A. Kilner and B. C. H. Steele, *Solid State Ionics*, **53-56**, 597-605 (1992).
4. R. H. E. van Doorn, I. C. Fullarton, R. A. de Souza, J. A. Kilner, H. J. M. Bouwmeester and A. J. Burggraaf, *Solid State Ionics*, **96**, 1-7 (1997).
5. X. Chen, S. Wang, Y. L. Yang, L. Smith, N. J. Wu, B.-I. Kim, S. S. Perry, A. J. Jacobson and A. Ignatiev, *Solid State Ionics*, **146**, 405-413 (2002).
6. Erwin E. Underwood, *Quantitative Stereology*, p. 23, Addison-Wesley Publishing Co., Reading, MA (1970).
7. M.W. den Otter, L.M. van der Haar and H.J.M. Bouwmeester, *Solid State Ionics*, **134**, 259-264 (2000).
8. W. Preis, E. Bucher and W. Sitte, *J. Power Sources*, **106**, n. 1-2, 116-121 (2002).
9. M.W. den Otter, H.J.M. Bouwmeester, B. A. Boukamp and H. Verweij, *J. Electrochem. Soc.*, **148 (2)**, J1-J6 (2001).
10. E.L. Cussler, *Diffusion – Mass Transfer in Fluid Systems*, Cambridge University Press, Cambridge, UK (1995).
11. S. Chapman and T. Cowling, *Mathematical Theory of Non-uniform Gases*, 3rd Edition, Cambridge University Press, Cambridge, UK (1970).

12. L. M. van der Haar, M. W. den Otter, M. Morskate, H. J. M. Bouwmeester and H. Verweij, *J. Electrochem. Soc.*, **149 (3)**, J41-J46 (2002).

13. S. Wang, A. Verma, Y. L. Yang, A. J. Jacobson and Ben Abeles, *Solid State Ionics*, **140**, 124-133 (2001).

14. E. Bucher, W. Jantscher, A. Benisek, W. Sitte, W. Preis, I. Rom and F. Hofer, *Solid State Ionics*, **141-142**, 375-380 (2001).

Tables

(a) LSC40 porous from in-house powder: porosity = 30.5%

Temp (ºC)	$D_{O2\text{-}N2}$ (cm/s^2)	D_{eff} (cm/s^2)	Time (s)
800	1.77	0.108	0.066
750	1.637	0.0999	0.071
700	1.51	0.0921	0.077
650	1.39	0.0846	0.084
600	1.27	0.0773	0.092

(b) LSC40 porous from Praxair powder: porosity = 24.5%

Temp (ºC)	$D_{O2\text{-}N2}$ (cm/s^2)	D_{eff} (cm/s^2)	Time (s)
800	1.77	0.0867	0.082
750	1.637	0.0802	0.089
700	1.51	0.0740	0.096
650	1.39	0.0679	0.105
600	1.27	0.0621	0.114

Table 1: Effective gas diffusion coefficients, D_{eff}, and time for the p_{O2} in the pores to reach 99% of the p_{O2} in the atmosphere of the chamber, from 800 to 600ºC: (a) LSC40 porous sample from in-house powder; and (b) LSC40 porous sample from Praxair powder.

Figure Captions

Figure 1: An SEM micrograph of $La_{0.6}Sr_{0.4}CoO_{3-\delta}$ (porosity = 30.5%) sample made using the in-house powder. Magnification: 4.0k.

Figure 2: Normalized conductivity vs. time at 600 and 800ºC for the porous sample made using in-house powder: p_{O2} change from 0.21 to 0.18 atm p_{O2} and current of 1.5A. Note that the kinetics is faster at 600^{o}C than at 800^{o}C; the sample equilibrates in about 10 seconds at 800^{o}C and about 4 seconds at 600^{o}C.

Figure 3: k_{chem} vs. p_{O2} at 800ºC for the porous sample made using in-house powder: Measurements made during both decreasing and increasing step changes in p_{O2}. Current: 0.8 amps.

Figure 4: k_{chem} vs. p_{O2} for the porous sample made using in-house powder over the temperature range from 600 to 800ºC. Measurements were made during decreasing p_{O2} step changes. Current: 0.8 amps.

Figure 5: k_{chem} vs. p_{O2} for the porous sample made using in-house powder over the temperature range from 600 to 800ºC. Measurements were made during increasing p_{O2} step changes. Current: 0.8 amps.

Figure 6: k_{chem} vs. p_{O2} for the porous sample made using Praxair powder over the temperature range from 600 to 800°C. Measurements made during decreasing step changes in p_{O2}. Current: 1.5 amps.

Figure 7: Plots of normalized conductivity, $g(t)$ vs. t for a dense sample of LSC40 of ~218 micron thickness at 700 and 800°C. Note that the kinetics is faster at 800°C than at 700°C; the sample equilibration time is ~4,000 seconds at 800°C and ~16,000 seconds at 700°C.

Figure 8: Arrhenius plot of k_{chem} vs. 1000/T for the porous and dense samples of LSC40 made from the in-house powder.

Figures

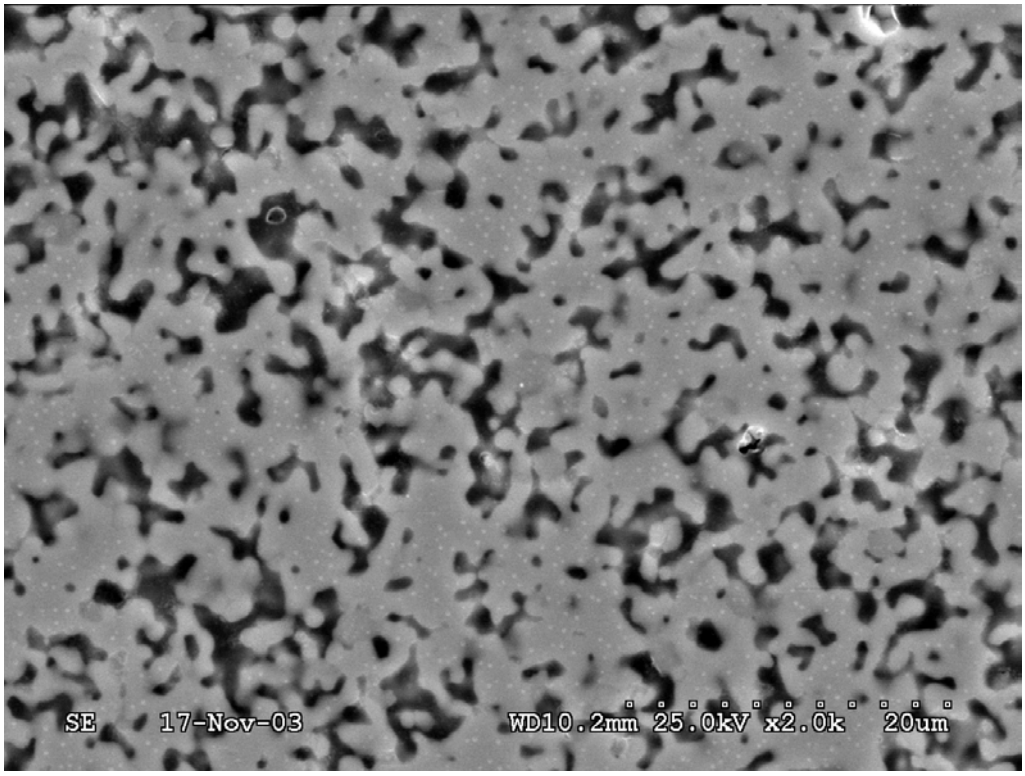


Figure 1

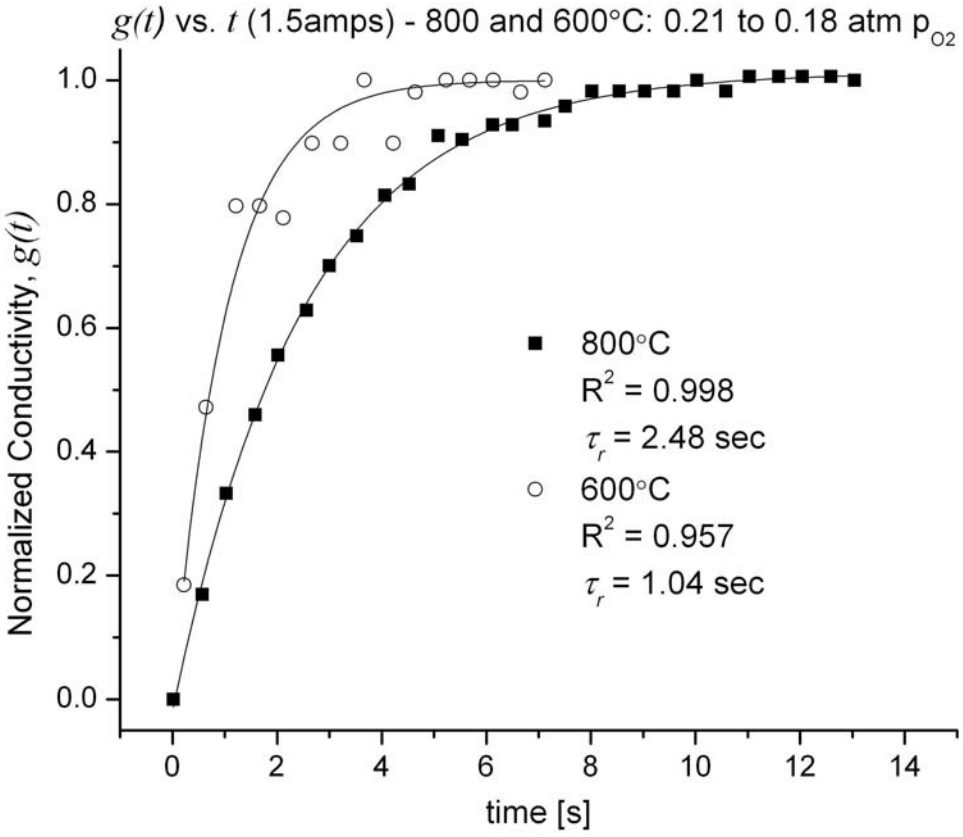

g(t) vs. t (1.5amps) - 800 and 600°C: 0.21 to 0.18 atm p$_{O2}$
Normalized Conductivity, g(t)
time [s]
800°C
R^2 = 0.998
τ_r = 2.48 sec
600°C
R^2 = 0.957
τ_r = 1.04 sec

Figure 2

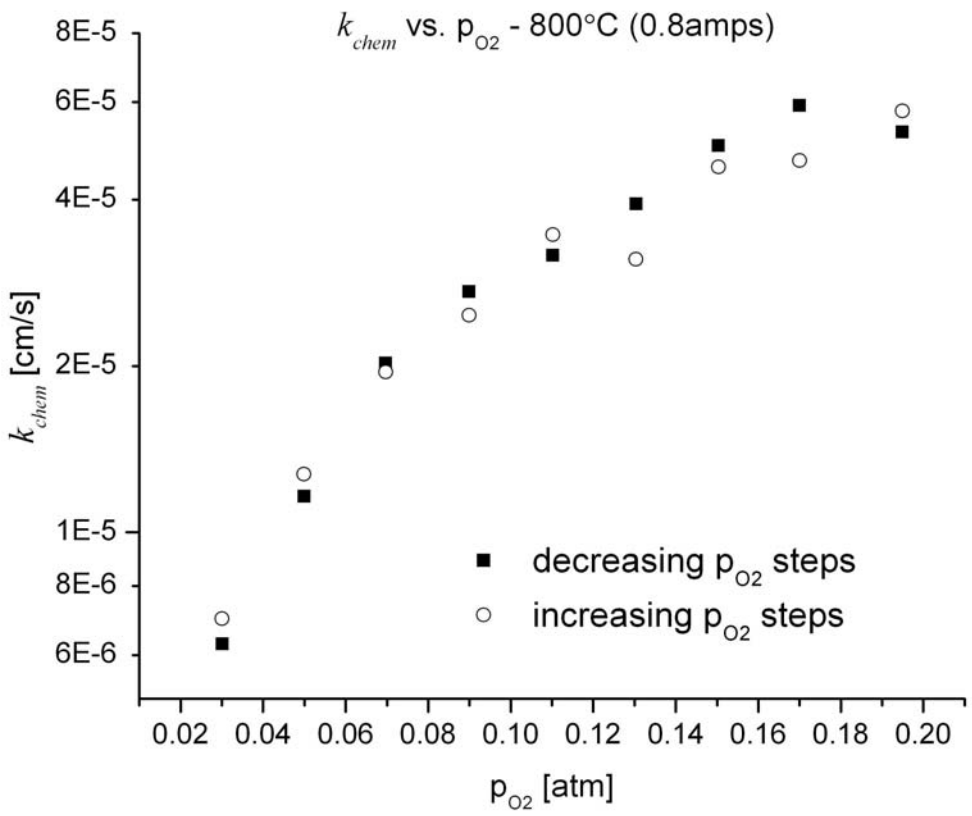

k_{chem} vs. p_{O2} - 800°C (0.8amps)
8E-5
6E-5
4E-5
2E-5
1E-5
8E-6
6E-6
k_{chem} [cm/s]
decreasing p_{O2} steps
increasing p_{O2} steps
0.02
0.04
0.06
0.08
0.10
0.12
0.14
0.16
0.18
0.20
p_{O2} [atm]

Figure 3

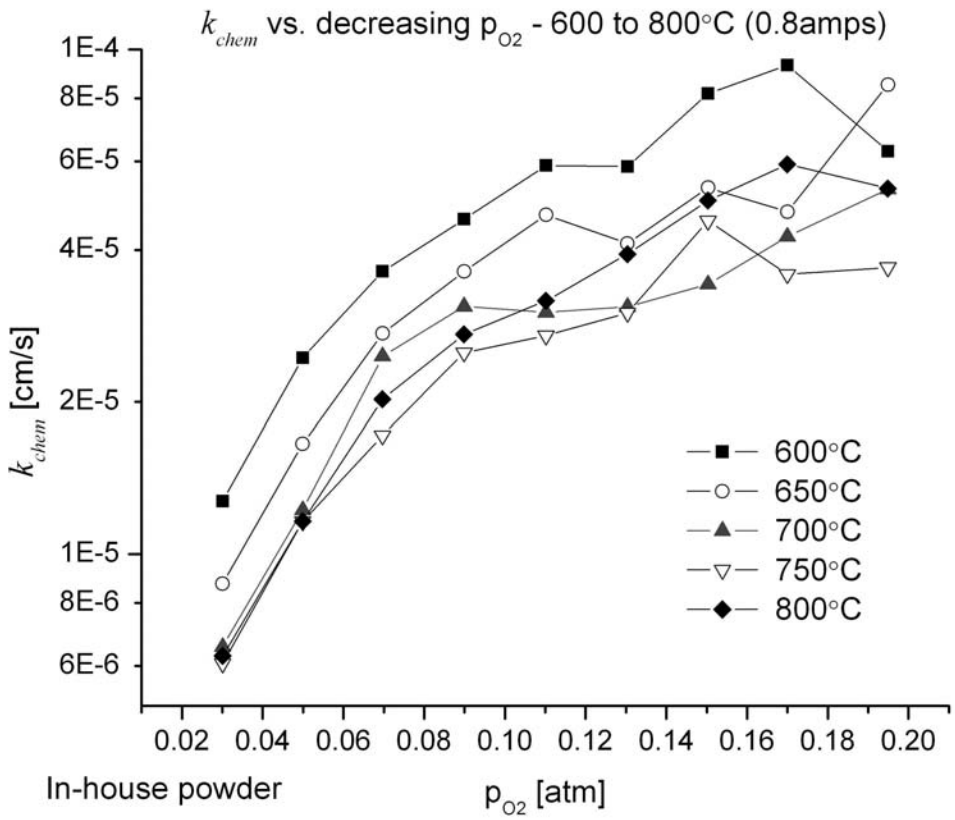

k_{chem} vs. decreasing p_{O2} - 600 to 800°C (0.8amps)
1E-4
8E-5
6E-5
4E-5
2E-5
1E-5
8E-6
6E-6
k_{chem} [cm/s]
600°C
650°C
700°C
750°C
800°C
0.02
0.04
0.06
0.08
0.10
0.12
0.14
0.16
0.18
0.20
In-house powder
p_{O2} [atm]

Figure 4

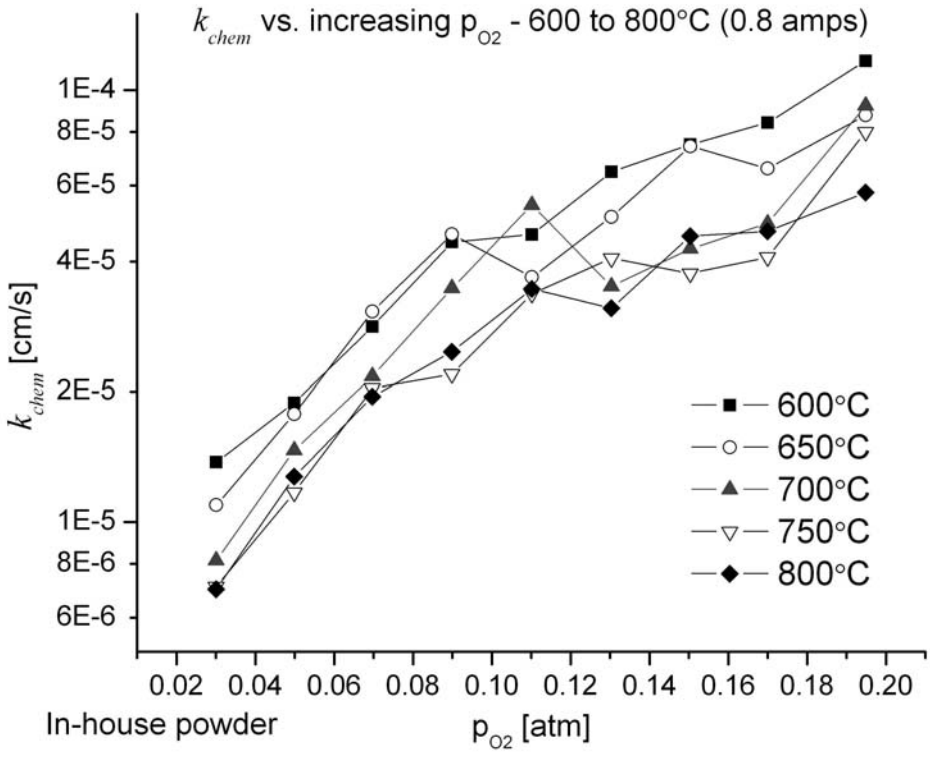

k_{chem} vs. increasing p_{O2} - 600 to 800°C (0.8 amps)
1E-4
8E-5
6E-5
4E-5
2E-5
1E-5
8E-6
6E-6
k_{chem} [cm/s]
600°C
650°C
700°C
750°C
800°C
0.02
0.04
0.06
0.08
0.10
0.12
0.14
0.16
0.18
0.20
In-house powder
p_{O2} [atm]

Figure 5

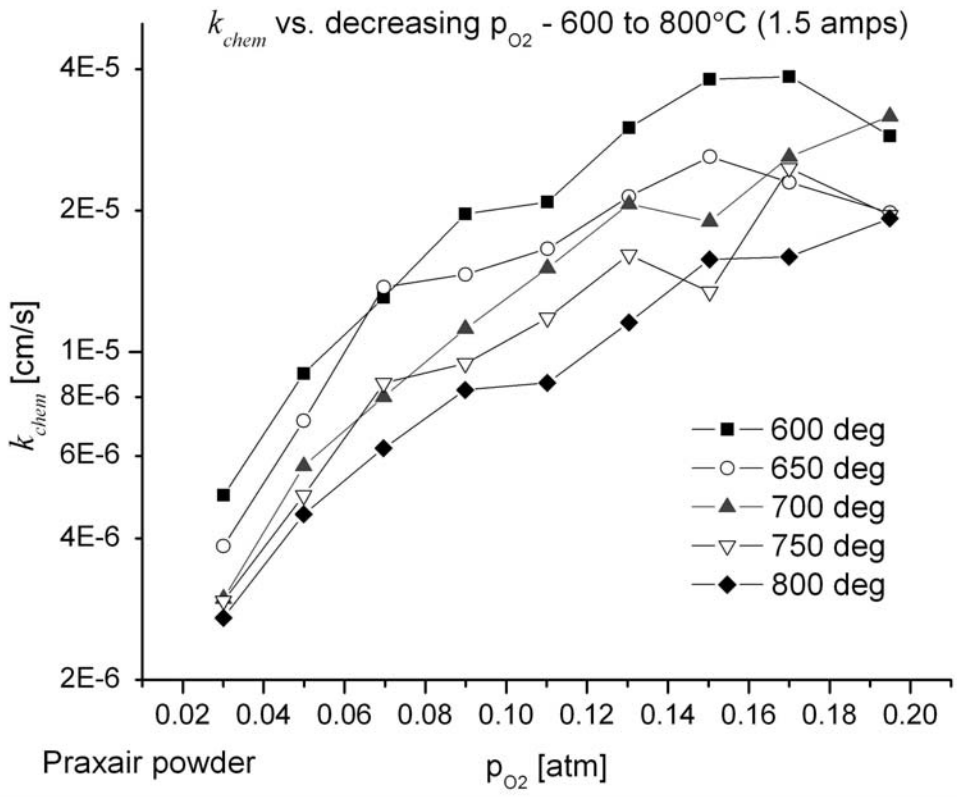

k_{chem} vs. decreasing p_{O2} - 600 to 800°C (1.5 amps)
4E-5
2E-5
1E-5
8E-6
6E-6
4E-6
2E-6
k_{chem} [cm/s]
0.02
0.04
0.06
0.08
0.10
0.12
0.14
0.16
0.18
0.20
p_{O2} [atm]
600 deg
650 deg
700 deg
750 deg
800 deg
Praxair powder

Figure 6

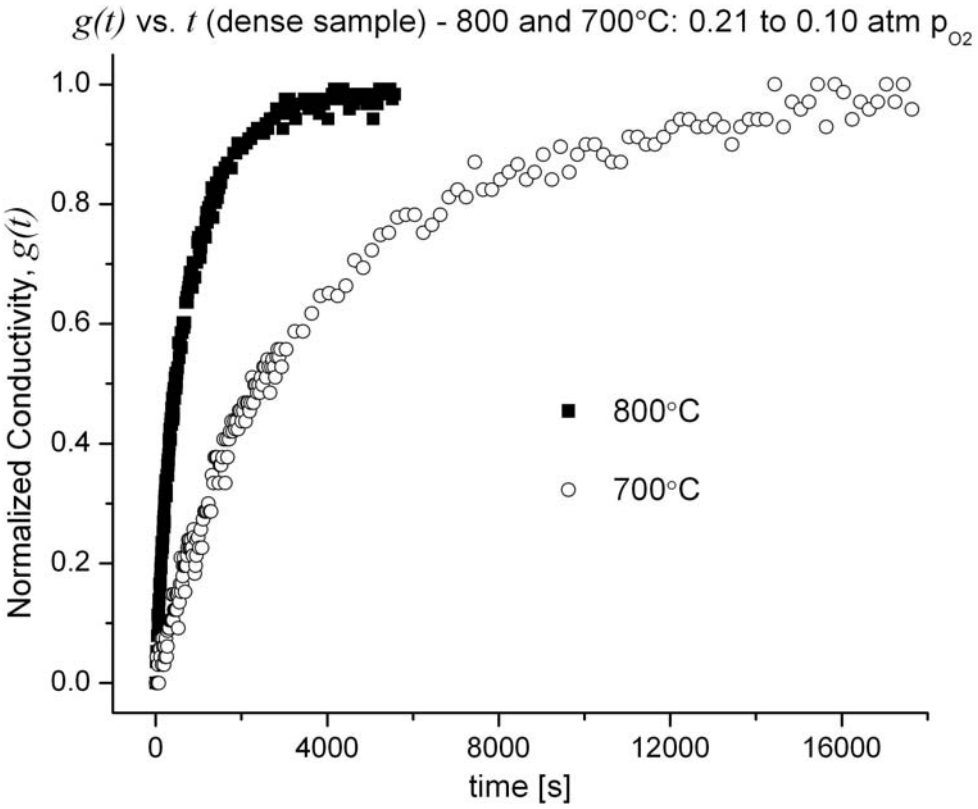

g(t) vs. t (dense sample) - 800 and 700°C: 0.21 to 0.10 atm p_O2
Normalized Conductivity, g(t)
1.0
0.8
0.6
0.4
0.2
0.0
0
4000
8000
12000
16000
time [s]
800°C
700°C

Figure 7

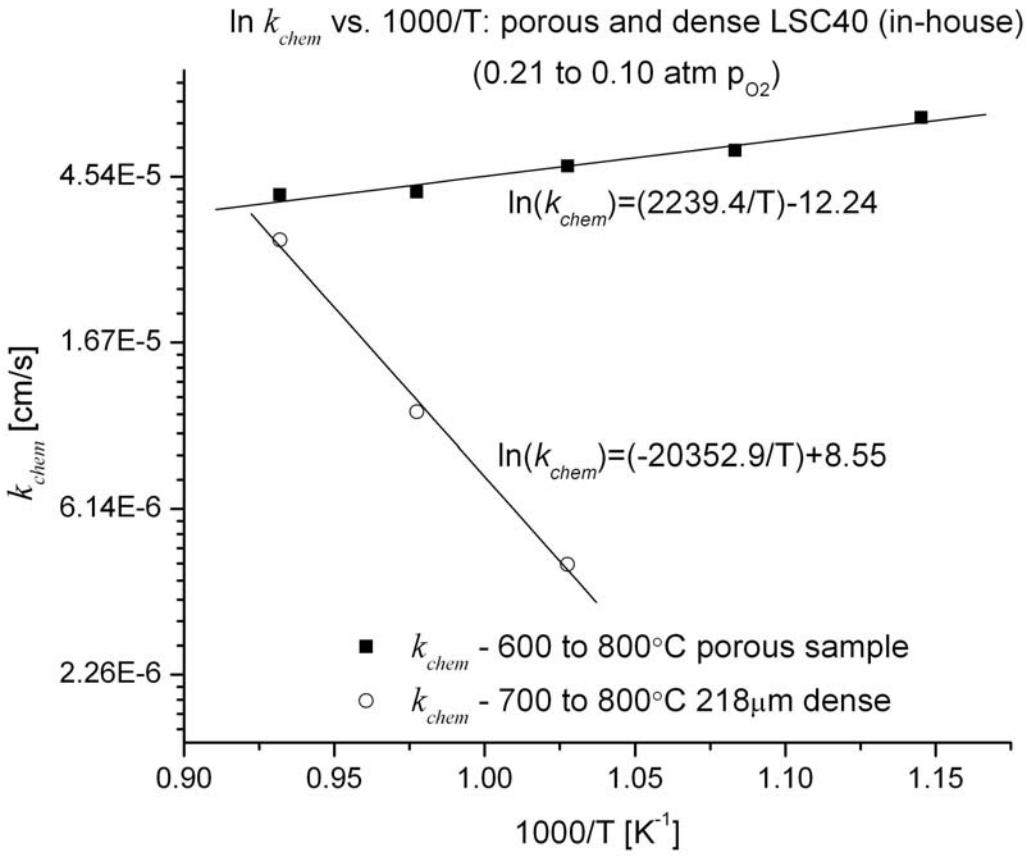

ln k_{chem} vs. 1000/T: porous and dense LSC40 (in-house)
(0.21 to 0.10 atm p_{O2})
4.54E-5
1.67E-5
6.14E-6
2.26E-6
k_{chem} [cm/s]
ln(k_{chem})=(2239.4/T)-12.24
ln(k_{chem})=(-20352.9/T)+8.55
k_{chem} - 600 to 800°C porous sample
k_{chem} - 700 to 800°C 218μm dense
0.90
0.95
1.00
1.05
1.10
1.15
1000/T [K^{-1}]

Figure 8